Master Thesis

Simulation of a Human Finger Joint with Sliding Surfaces

Alexander Synek

DLR

Institut für Robotik und Mechatronik	BJ.: 2011 IB.Nr.: 572-11-23

MASTERARBEIT

SIMULATION OF A HUMAN FINGER JOINT WITH SLIDING SURFACES

Freigabe:	Der Bearbeiter:	Unterschriften
	Alexander Synek	i. A. Georg Stillfried
	Betreuer:	
	Georg Stillfried	Georg Stillfried
	Der Institutsdirektor	
	Prof. Dr. G. Hirzinger	

Dieser Bericht enthält 111 Seiten, 70 Abbildungen und 18 Tabellen

Ort: Oberpfaffenhofen	Datum: 25.01.2012	Bearbeiter:	Zeichen:

FH Technikum Wien

MASTER THESIS

Thesis submitted in partial fulfilment of the requirements for the degree of Master of Science in Engineering

at the University of Applied Sciences Technikum Wien
Mechatronics and Robotics

Simulation of a Human Finger Joint with Sliding Surfaces

by
Alexander Synek, BSc
A-1120, Vienna, Schönbrunnerschloßstraße 31A/21

Supervisors:
FH-Prof. Dipl.-Ing. Dr. Fritz Schmöllebeck
Dipl.-Ing. Georg Stillfried

Vienna, September 16, 2011

FACHHOCHSCHULE
TECHNIKUM WIEN

Declaration

I confirm that this paper is entirely my own work. All sources and quotations have been fully acknowledged in the appropriate places with adequate footnotes and citations. Quotations have been properly acknowledged and marked with appropriate punctuation. The works consulted are listed in the bibliography. This thesis has not been submitted to another examination panel in the same or a similar form, and has not been published.

Place, Date

Signature

Kurzfassung

Eine Hauptaufgabe im Bereich der Automation ist das Manipulieren von Objekten. Das Hand-Arm System des Menschen übersteigt hierbei die Flexibilität aktueller Maschinen. Aus diesem Grund wird am DLR ein anthropomorphisches Hand-Arm System entwickelt, das die Funktionalität der menschlichen Gelenke auf ein robotisches System überträgt. Zur kinematischen Modellierung der Gelenke werden derzeit überwiegend feste Rotationsachsen verwendet. Da dieser Ansatz eine Annäherung der tatsächlichen Bewegung darstellt, verbleibt zwischen gemessenen und simulierten Gelenkstellungen ein Fehler. Verglichen mit anderen Gelenken der Hand werden im Daumen, und im Speziellen im CMC Gelenk des Daumens, große Abweichungen festgestellt. In dieser Arbeit wird ein neuartiger Ansatz zur Modellierung von menschlichen Fingergelenken vorgestellt, der auf aneinander abgleitendenden Kontaktoberflächen basiert. Das CMC Gelenk wird zu diesem Zweck als Mehrkörpersystem in der Simulationssoftware SIMPACK modelliert. Es besteht aus einem festen und einem frei beweglichen Knochen, der durch das Einwirken von Kräften bewegt wird. Kräfte werden durch den Kontakt, acht Muskeln und sieben Bändern ausgeübt. Die Kontaktgeometrie ist durch undeformierbare Polygonoberflächen repräsentiert, die aus MRI Bildern extrahiert werden. Eine modifizierte Version von PCM wird verwendet um die Kontaktkräfte anhand der Durchdringung der Oberflächen zu berechnen. Muskeln und Bänder werden als nichtlineare Punkt-zu-Punkt-Federelemente modelliert, die Zugkräfte entlang der Verbindungslinie eines proximalen und distalen Ansatzpunktes ausüben. Die Koordinaten dieser Punkte werden aus der Literatur übernommen. Das resultierende Modell, bestehend aus zwei Körpern und 21 Kraftelementen, wird in SIMPACK zusammengesetzt und im Zeitbereich simuliert. Als Eingangsgrößen dienen acht Funktionen, die die Aktivierungslevels der einzelnen Muskeln repräsentieren. Obwohl das vorgestellte biomechanische Modell nicht optimiert wurde, können durch die Aktivierung einzelner Muskeln plausible Bewegungsabläufe simuliert werden. Die Ergebnisse dieser Arbeit zeigen, dass eine Mehrkörpersimulation in Kombination mit PCM eine simple und zeitgünstige Methode darstellt, um kinematische Simulationen menschlicher Fingergelenke auf Basis ihrer Morphologie durchzuführen. Durch die anatomische Übereinstimmung mit dem tatsächlichen Gelenk bietet sich der Modellierungsansatz darüber hinaus auch für Anwendungen in medizinischen Bereichen an, wie beispielsweise präoperativen Untersuchungen oder Endoprothetik.

Schlagwörter: Biomechanisch, Kontakt, Daumen, CMC, Gelenk

Abstract

In any automation process, object manipulation is a main task. The human hand and arm represent a system exceeding the versatility of current manipulation systems. Hence, at DLR a highly anthropomorphic hand arm system is being developed which aims at transferring the functionality of the respective human joints to a robotic system. The kinematics of human joints is often modelled with fixed rotational axes. This approximation leads to an error, which was found to be large especially for the CMC joint of the thumb. In this thesis, a new approach of simulating the kinematics of a human finger joint based on contacting surfaces is proposed. The CMC joint of the thumb is modelled as a multi body system in SIMPACK, consisting of one fixed and one unconstrained bone. The movement of the joint is determined by the forces exerted by the contacting articular surfaces, eight muscles and seven ligaments. The contact geometry is represented by undeformable polygonal surfaces extracted from MRI images. A modified version of PCM is used to compute the contact forces depending on the surface penetration depth. Muscles and ligaments are modelled as point-to-point nonlinear spring elements, exerting tensile forces along the connection line between a proximal and a distal attachment point. The attachment locations are determined based on anatomical and biomechanical literature. All components are assembled in SIMPACK to conduct simulations in time domain. The movement is controlled by eight input functions representing the activation levels of the muscles. Even though the present model is not optimized, comparison to literature shows that single and multi muscle activation leads to physiological movements. It is concluded that multi body simulations in combination with PCM represent a simple and fast means of simulating finger joint kinematics based its actual morphology. Due to its anatomical correspondence, the proposed model is capable of investigating the influence of single tissues to joint movements, which makes it more versatile than conventional models based on fixed axes.

Keywords: Biomechanical, Contact, Thumb, CMC, Joint

Acknowledgements

I would like to express my gratitude to my supervisor at DLR, Georg Stillfried, without whose guidance and knowledge this research project would not have been possible. I would also like to thank all members of the bionics group at DLR for their trust and the possibility of working in a pleasant, yet exciting environment. Special thanks also to Marcus Settles for enabling the MRI scans at Klinikum Rechts der Isar, which were indispensable for this thesis.

Contents

1. Introduction

In any automation process, manipulation is a main task. Robotic systems represent a versatile method of manipulating objects, based on end effectors and robotic arms. Since the the human hand and arm still exceed the capabilities of robotic systems, the German aerospace center (*german* "Deutsches Zentrum für Luft und Raumfahrt", DLR) works on biologically inspired robotics. The DLR Hand II is the most recent end effector intended for the use in mobile robotics. In order to meet the high requirements of flexibility in this field of applications, it was designed as a four finger gripper with 14 degrees of freedom (Butterfass et al. 2004). In combination with the light weight robot arm developed at the DLR, human like actions are performed, such as ball throwing. However, it was experienced that this system is not capable of reproducing the results achieved by humans to the full extent. In a new approach, a highly anthropomorphic hand arm system is being developed (Grebenstein et al. 2011). Besides a new actuation principle based on energy storage, it is intended to incorporate the actual kinematics of the human hand and arm. Rather than just copying the respective anatomy, the functional principles are investigated and transferred to the robotic system. For this purpose, the kinematics of the human hand is studied intensively and in great detail at DLR.

1.1. State of the Art

In order to conduct investigations on the human hand kinematics, different models have been established. They describe the kinematics of the whole hand, single fingers or single joints. Anatomically, the movement of a human joint results from two contacting surfaces and restrictive forces due to surrounding tissues. In most biomechanical models, this movement is approximated by fixed rotational axes serving as a link between two bones.

Stillfried (2009) presents a very accurate 24 degree of freedom (DoF) model of the whole hand, based on in-vivo measurements of the locations of the bones of the hand in different postures. The positions and orientations of the axes of the joints are optimized to fit all the postures with minimal error. Another approach is to take dynamics into account to determine the movement of the joints depending on the force exerted by the muscles. These simulations mostly focus on a single finger: Both Sancho-Bru et al. (2001) and Brook et al. (1995) propose a biomechanical five DoF model of a human finger in order to determine the muscle forces during free movements and different grasps. Similar models have been established for the thumb: Wu et al. (2009) proposes a five DoF model of the thumb with optimized muscle moment arms and Valero-Cuevas et al. (2003) uses a five DoF model in order to predict the force at the tip of the thumb depending on the muscle forces. Giurintano et al. (1995) proposes a model that neglects the anatomical correspondence and introduces additional rigid bodies in between the bones.

Biomechanical models that incorporate stabilizing tissues and contacting surfaces are developed only for larger joints, such as the knee. They mainly serve the purpose of predicting internal stresses, deformations and wear (Goreham-Voss et al. 2010). The kinematics of these models is determined either by fixed axes (Guo et al. 2009) or the combination of contacting surfaces and stabilizing tissues (Landon et al. 2009).

1.2. Problem Statement

Kinematic or dynamic simulations of the human hand are based on the assumption of fixed rotational axes as links between bones. Since these axes approximate the actual movement of the joint, an error remains. The 24 DoF kinematic model of the whole hand from Stillfried and van der Smagt (2010) results in a maximum rotational and translational error of $5.4\,^\circ$ and $0.7\,\mathrm{mm}$ respectively for all joints except for the thumb saddle joint. At this joint, the translational error amounts to $2.6\,\mathrm{mm}$. These errors in the kinematic description lead to difficulties in further calculations, such as the prediction of the forces at the tip of the thumb due to muscles activation conducted by Valero-Cuevas et al. (2003). In order to improve the results of future experiments and simulations based on kinematic models, it is necessary to investigate alternative ways of describing the joint movements. This holds especially for the thumb and the thumb saddle joint.

1.3. Definition of Objectives

Since the assumption of fixed axes for describing the thumb kinematics might not be able to reproduce actual movements in sufficient accuracy, a new modelling approach is proposed: In contrast to calculating rotational axes to best fit certain measurements, all anatomical components contributing to the joint movement are modelled to provide a physiological movement. Due to its complexity and comparatively large error in the kinematic model of Stillfried and van der Smagt (2010), the thumb saddle joint is chosen to be modelled in this thesis. The biomechanical model should involve:

- Contacting surfaces
- Muscles
- Ligaments

For each component, both anatomical and mechanical aspects have to be investigated. Appropriate methods of conducting simulations based on contacting surfaces have to be determined and compared. Finally, all components are assembled to investigate the joint kinematics. Based on the outcome of the simulations conducted with the biomechanical model of the thumb saddle joint, a verdict about the applicability of the proposed modelling approach to kinematic investigations can be derived.

2. Investigation

The aim of this thesis is to develop a biomechanical model of a human finger joint. It is obvious that extensive literature investigation is necessary in both anatomical and mechanical fields. Furthermore, the developed model should account for the shape of the joint surfaces, thus contact mechanics has to be considered.

In order to account for all of these aspects, the investigation is divided into three sections: Anatomy, biomechanics and contact mechanics. The anatomical section provides general information on human joint and subsequently focuses on the functionality of the joints of the thumb. Finally, all anatomical components contributing to joint stability and movement are determined. In order to incorporate them in a biomechanical model, material properties have to be specified. This is covered by the field of biomechanics. In the last section of this chapter, analytical and computational approaches of contact mechanics are presented.

2.1. Anatomy

In this section, the basic knowledge of the morphology and functionality of the human thumb is provided. The anatomical terminology and main components of human joints are introduced in the section of general anatomy. Following sections gradually focus on the thumb. Special anatomy deals with the morphology, without taking functionality into consideration. This is part of the functional anatomy, where the influence of the muscles and ligaments on the actual movement of the thumb is described.

2.1.1. General Anatomy

In anatomy, it is common to use a special terminology for describing directions, planes, movements and single components of joints. Figure 2.1 shows the human hand in a neutral position, as well as the most important planes and directions. If not denoted differently, text and figures always refer to the right hand. Later chapters are based on this terminology, which is indispensable for giving distinct information on morphology and functionality.

Besides morphology, it is important to consider the principle behind the human movement. It is commonly known that the body consists of bones that are connected by joints and moved by muscles. From the anatomical point of view, not all of these connections are "real" joints, i.e. joints that allow a significant movement. There are generally two types of connections: Diarthrosis and synarthrosis. The diarthrosis can be considered to be a "real" joint, which is able to move freely, whereas the synarthrosis is a joint barely able to move. Synarthrosis are continuous connections of bones, e.g. by cartilage. In contrast to synarthrosis, there is a small separation of the bones in the diarthrosis. The space between the bones is called joint space. It might, however, be that surrounding ligaments are too tight to allow significant movement. These joints are called amphiarthrosis. (Schünke 2005)

Generally, the morphology of the diarthrosis is the same for the whole body. Figure 2.2 shows all the parts of a joint schematically. The geometry of the parts is individual for each joint. This

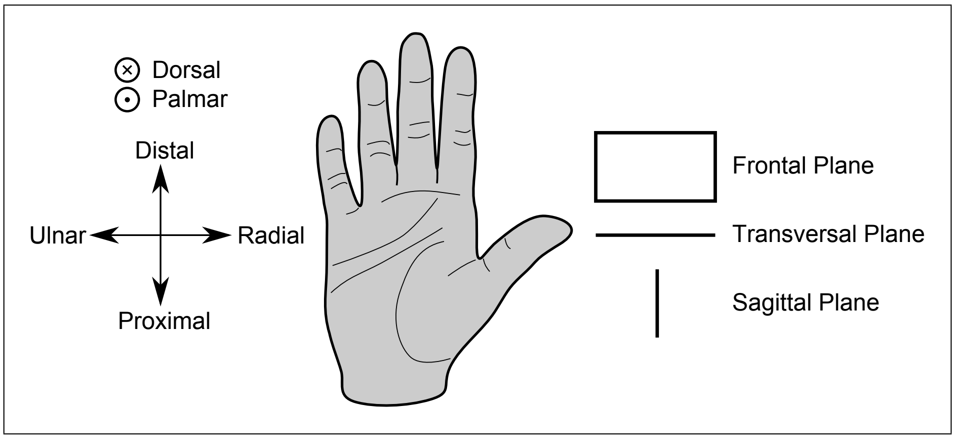

Figure 2.1.: Anatomical terminology for planes and directions. *Adapted from:* Schünke (2005)

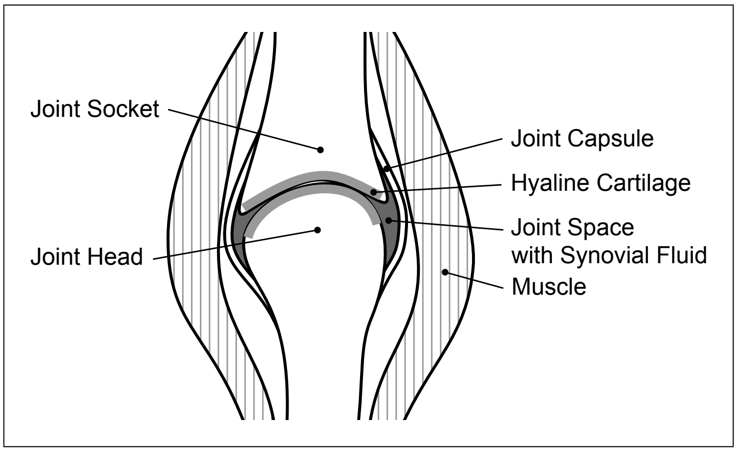

Figure 2.2.: A schematic depiction of the general morphology of a human joint. *Adapted from:* Schünke (2005)

holds especially for the articular surfaces, which are considered to have significant influence on the possible movements. It is important to realize that both the head and the socket of a joint are covered by a thin layer of hyaline cartilage. Hyaline cartilage is rather elastic, thus the mechanical properties of bone and cartilage have to be separated clearly (Uhlmann 1996). The joint space is filled with synovial fluid, which serves as a lubricant. It is produced in an inner membrane of the articular capsule and does not only "grease" the joint, but also nourishes the cartilage. Stability of the joint is provided by the soft articular capsule as well as inner and outer ligaments. Ligaments are rather strong and capable of limiting the movement. Muscles have stabilizing abilities as well, but, in contrast to ligaments, are able to contract and cause a movement. Tendons are the passive link between either a muscle belly and a bone, or a muscle belly and another muscle belly. The muscle as a whole is always attached to two skeletal parts. The proximal point of attachment is called the origin of the muscle and the distal one is called insertion. Between their origin and insertion, it occurs that the tendons get redirected by a so called hypomochlion (e.g. bones or connective tissue). To avoid wear at these points of deflection, tendons are often protected by tendon sheaths, which contain synovial fluid and allow almost frictionless sliding. (Schünke 2005)

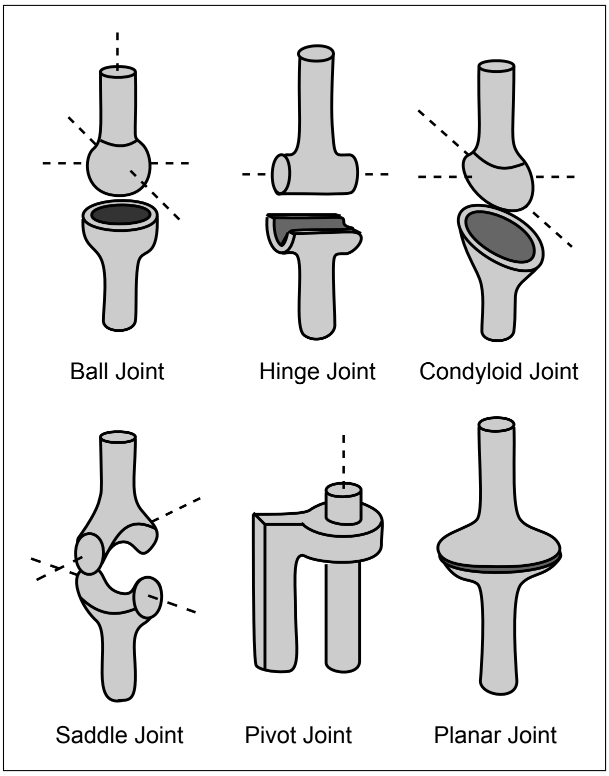

Figure 2.3.: Types of diarthrodial joints of the human body, idealized as technical joints. *Adapted from:* Schünke (2005)

Depending on the articular surface, different kinds of movements are possible in a joint. Figure 2.3 gives an overview of comparable technical joints, which are used to model the actual movement of the diarthroses. Distinguishing between modelled and actual movement is necessary, since technical joints assume the bones to rotate about a fixed axis, whereas the actual movement is much more complex. This is due to the irregularly shaped surfaces, as well as the influence of the ligaments and other surrounding tissues. There is a certain terminology for the movements of the joints, considering a maximum of three axes and therefore six possible directions: Adduction and abduction, extension and flexion, pronation and supination. Unfortunately, this terminology is not commonly agreed on, therefore differences are likely to occur among publications. (Uhlmann 1996)

2.1.2. Special Anatomy of the Hand

As the previous chapter has shown, joints consist mainly of the following parts: Articulating bones, ligaments and muscles. In this chapter, each tissue is explained with respect to its appearance in the joints of the hand, focusing on the thumb.

Bones

Figure 2.4 shows all bones of the human hand, labelled with the respective anatomical expression. There are eight bones that belong to the carpus and are therefore called carpal bones. Distal to the carpus, there are the bones of the five fingers: The metacarpal bone, the proximal phalanx, middle phalanx and the distal phalanx. They are enumerated from 1 to 5, starting at the thumb. The thumb only has two phalanges, the middle phalanx is missing.

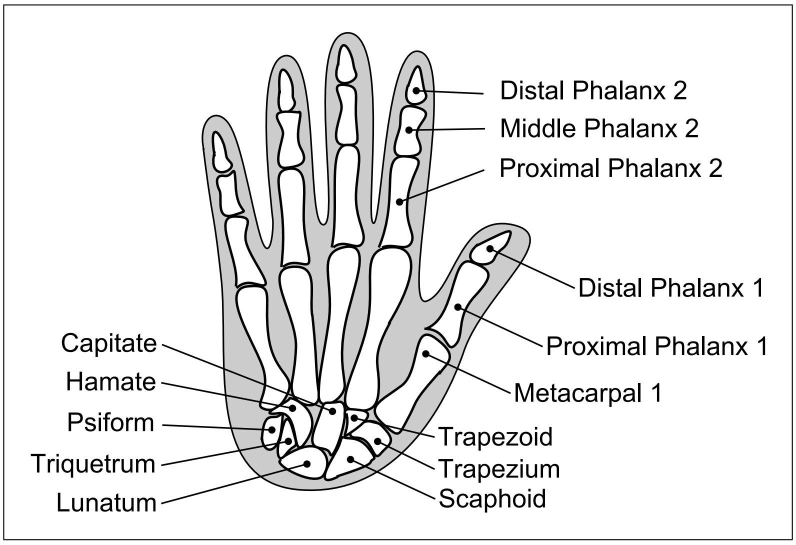

Figure 2.4.: Bones of the hand and the respective anatomical notation. *Adapted from:* Schünke (2005)

The regions at the end of the bone are called epiphyses and the part in between is called the diaphysis (Uhlmann 1996). In the following sections, the proximal epiphysis is referred to as the base and the distal one as the head of the bone.

Ligaments

Generally, the ligaments of the hand can be divided into four groups: Ligaments between forearm and the carpal bones, ligaments between the carpal bones themselves, ligaments between carpal and metacarpal bones and ligaments between the bases of the metacarpal bones (Schünke 2005). As this thesis focuses on the thumb, it is not necessary to name all the ligaments of the hand in detail. Only the main stabilizing ligaments of the thumb are are elucidated and depicted in figure 2.5. Ligaments with another purpose, e.g. keeping the tendon sheath in the right place, are neglected and also not displayed in figure 2.5.

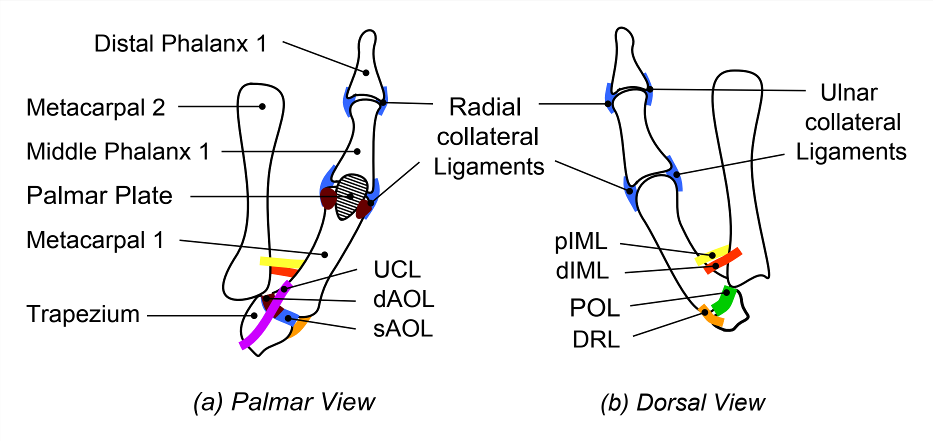

(a) Palmar View (b) Dorsal View

Figure 2.5.: A schematic depiction of the stabilizing ligaments of the thumb in palmar and dorsal view. *Adapted from:* Kapandji (2006) and Nanno et al. (2006)

The number of ligaments stabilizing the first metacarpal bone is still controversial and ranging from four (Kapandji 2006) to seven (Nanno et al. 2006). Nanno et al. (2006) reports the following seven bundles of collagen fibres to be essential: Two dorsal and three palmar, as well as two intermetacarpal ligaments. All of these seven ligaments are shown shown in figure 2.5, corresponding terminology and abbreviations are denoted in table 2.1. In other publications (Imaeda et al. 1993, Tan et al. 2011), only five of the ligaments mentioned are claimed to be influencing the stability of the first metacarpal bone.

	Ligament	**Abbreviation**
Palmar ligaments:	Superficial anterior oblique ligament	sAOL
	Deep anterior oblique ligament	dAOL
	Ulnar collateral ligament	UCL
Intermetacarpal ligaments:	Dorsal first intermetacarpal ligament	dIML
	Palmar first intermetacarpal ligament	pIML
Dorsal ligaments:	Posterior oblique ligament	POL
	Dorsoradial ligament	DRL

Table 2.1.: Notation of the ligaments stabilizing the first metacarpal bone

Between the first metacarpal bone and the proximal phalanx especially the four collateral ligaments are of importance. On each side, originating at the head of the metacarpal phalanx, one is inserting directly at the base of the proximal phalanx, and one is inserting at the palmar plate. The proximal and the distal phalanx are connected by a ulnar and a radial ligament, both of them originating at the head of the proximal and inserting at the base of the distal phalanx. (Kapandji 2006)

Muscles

Muscles are the active part of the musculoskeletal system. In order to understand the movement of the thumb, it is inevitable to be aware of all the muscles contributing to thumb motion, as well as their general functionality. However, detailed morphology of the muscles themselves is not provided in this section.

Figure 2.6 shows all thumb moving muscles schematically, including the areas of origination and insertion. Two groups can be distinguished: The long, extrinsic muscles of the thumb and the short, intrinsic ones. There are four extrinsic muscles that all originate at the forearm and five intrinsic muscles, both originating and inserting at the hand. Terminology and abbreviations are provided in table 2.2. (Kapandji 2006)

2.1.3. Functional Anatomy of the Thumb

In this chapter, functional influences of the bones, ligaments and muscles regarding the movement of the joints of the thumb are be explained. The joints are named after the articulating bones involved:

- The joint between the trapezium, which is a carpal bone, and the first metacarpal bone is called the first carpometacarpal joint (CMC joint)
- The joint between the first metacarpal bone and the first proximal phalanx is called the metacarpophalangeal joint (MCP joint)
- The joint between the first proximal phalanx and the first distal phalanx is called the interphalangeal joint (IP joint)

In order to describe the joint kinematics, it is common to approximate the movement with rotational axes. The DoF of each joint correspond to the number of axes used in the model. Figure 2.7 shows the kinematic description of the thumb established by Brand and Hollister (1999), consisting of a saddle joint and two hinge joints.

For the analysis of thumb movements, both the CMC and MCP joint are mostly considered to have two DoF: one axis for the flexion and extension, the other one for the abduction and adduction. Due to the inclined orientation of the trapezium, flexion means the movement towards the little finger and extension the movement apart from it. Adduction and abduction describe the movement to or apart from the index finger. The IP joint only has one DoF, enabling flexion and extension.

In general, independent movements of the joints are rare since most tendons cross more than one joint. Forces transmitted by tendons inserting at the proximal or distal phalanx thus result in a movement of the CMC joint as well. Additionally, some movements are caused only by the fact that the axes of rotation are neither parallel nor perpendicular to each other. Flexion of the IP joint, for instance, causes a rotation of the distal phalanx. This is related to the tilt of the axis and called conjunct rotation. The extent to which this rotation occurs is always related to another movement, such as the flexion in this case, and cannot be controlled actively. (Brand and Hollister 1999)

In the following sections, the shape of articular surfaces and the functionality of ligaments and muscles is elucidated for each joint of the thumb.

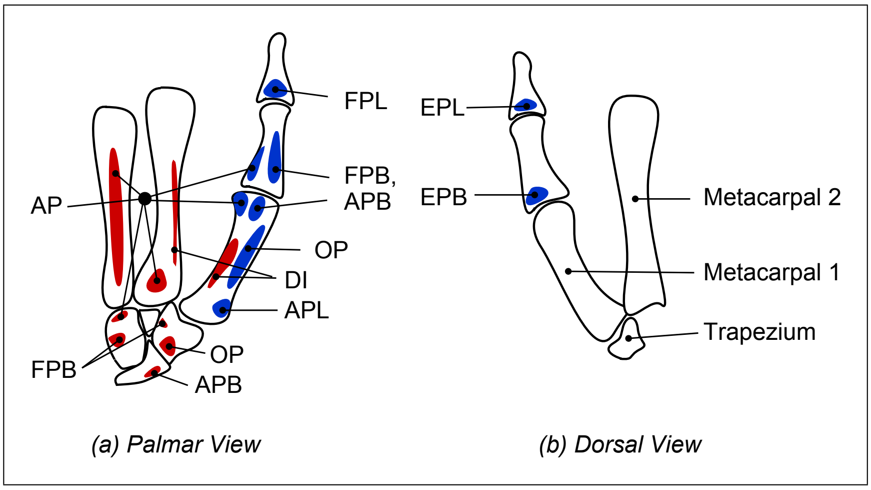

Figure 2.6.: A schematic depiction of the attachment areas of the thumb moving muscles in palmar and dorsal view. Areas of origination and insertion are colored in red and blue, respectively. *Adapted from:* Schünke (2005)

	Muscle	**Abbreviation**
Extrinsic:	Flexor pollicis longus	FPL
	Extensor pollicis longus	EPL
	Extensor pollicis brevis	EPB
	Abductor pollicis longus	APL
Intrinsic:	Adductor pollicis	AP
	Abductor pollicis brevis	APB
	Opponens pollicis	OP
	Flexor pollicis brevis	FPB
	First interosseus dorsalis	DI

Table 2.2.: Notation of extrinsic and intrinsic thumb moving muscles

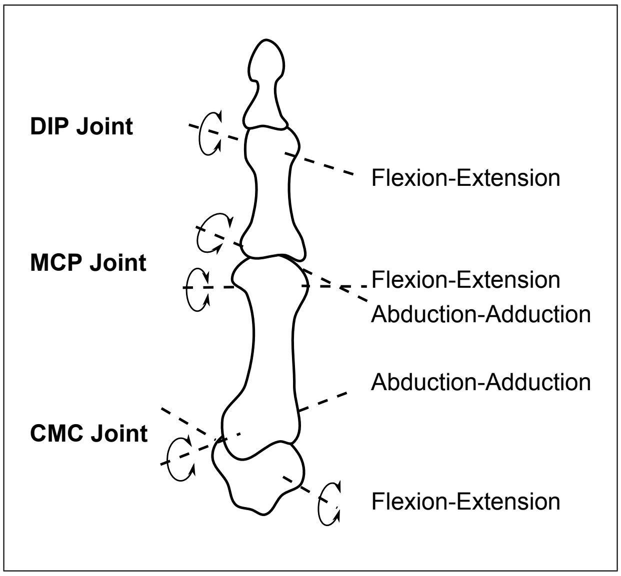

Figure 2.7.: Anatomical terminology of the joints of the thumb and a five DoF kinematic description using fixed rotational axes. *Adapted from:* Brand and Hollister (1999)

The CMC Joint

The CMC joint is one of the most complex joints in the human hand. In combination with the MCP joint it allows the thumb to oppose the other fingers, which is essential for grasping. Exact functionality is still controversial. Kapandji (2006) is convinced that axial rotation in the CMC joint is not possible due to arrangement of ligaments, whereas Koebke (1983) states that limited axial rotation is likely to occur, as indicated by damages of the cartilage. However, it is commonly agreed on that the thumb as a whole performs a rotation during combined movements, such as opposition.

Complexity of the CMC joint arises mainly from the shape of the articular surfaces. Both trapezial and metacarpal surfaces are convex-concave, forming a saddle joint. Kuczynski (1974) provides a very detailed description of the surfaces. As it can be seen in figure 2.8, at the trapezial surface there is a curved ridge C-D, running from the base of the second metacarpal bone. Transverse to the ridge there is a groove A-B. The metacarpal surface approximately matches the shape of the trapezial surface. Differences can be measured in the length of the ridges and grooves, as well as the radius of the metacarpal groove C'-D', which is slightly smaller than the radius of the curvature A-B.

A more practical description of the surface can be derived if the actual shape is compared to different idealized surfaces such as rotational hyperboloids, parabolic hyperboloids or similar. An asymmetric area on the surface of a torus figure 2.9 is assumed to deliver the most appropriate approximation to the real surface, considering the description of Kuczynski (1974). If two of these surfaces are put together, they form a Cardanic joint. According to Kapandji (2006), this enables the CMC joint to perform axial rotation as a combination of two movements, without losing congruity of the surfaces.

The number of ligaments contributing to the stability of the joint differs among publications. Kapandji (2006) describes four ligaments to stabilize the joint, working together to support the movement and to ensure the congruity of the articular surfaces. Functionality of five ligaments

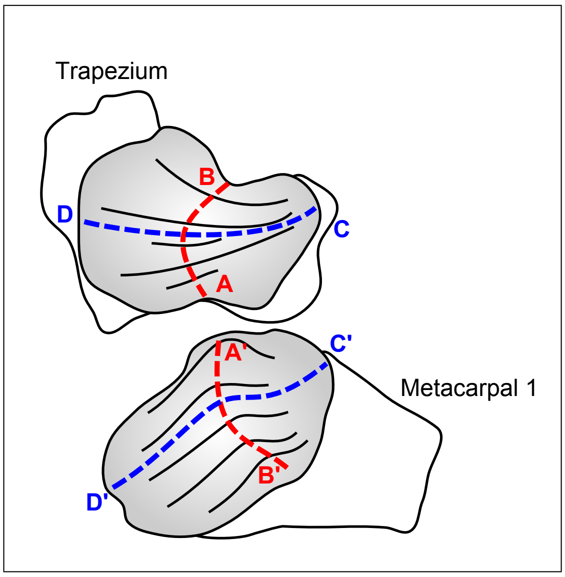

Figure 2.8.: Shape of the trapezial and metacarpal articular surface of the CMC joint. *Adapted from:* Kuczynski (1974)

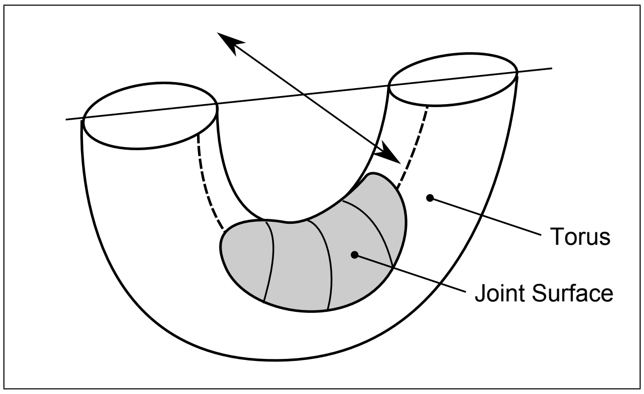

Figure 2.9.: An asymmetric area on the surface of a torus representing an idealization of the articular surfaces of the CMC joint. *Adapted from:* Kapandji (2006)

is reported in great detail by Imaeda et al. (1993): Palmar ligaments are lax in flexion and tense in extension. Dorsal ligaments are tense or unchanged during flexion and lax during extension. Abduction and adduction causes almost all the ligaments to be tense and lax, respectively. Imaeda et al. (1993) identifies the dAOL, supported by the UCL, as the most important ligaments to stabilize the CMC joint. Agreement on this result is found in more recent publications, such as Nanno et al. (2006).

As it was already mentioned, tendons cause a movement in each joint they are crossing. Figure 2.10 shows the cross section at the CMC joint at the level of the flexion-extension axis, displaying all tendons and muscles of the thumb passing by. It is clear that all of them influence the movement of the CMC joint to a certain extent. Their contribution to flexion-extension and adduction-abduction, respectively, can be determined roughly by their position relative to the estimated axes of rotation. (Brand and Hollister 1999)

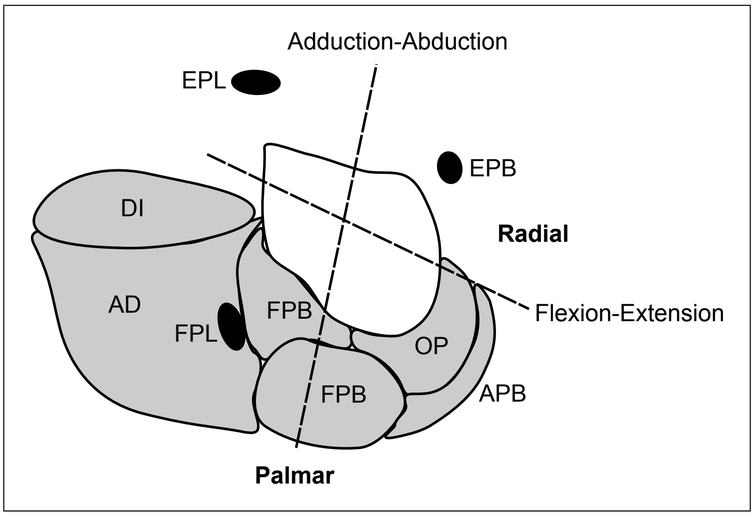

Figure 2.10.: Muscles and tendons passing the CMC joint, displayed in the cross section at the level of the flexion-extension axis. *Adapted from:* Brand and Hollister (1999)

The APB and the OP work together to perform the opposition movement, which is a combination of pronation, abduction and flexion. Strongest flexion is achieved if both FPB and AP are activated. The AP is also the main pinching muscle. The APL is a very strong muscle capable of extension and abduction of the CMC joint and serving as a counterpart for the adductors. Another strong extensor is the EPL. As its tendon is not attached to the phalanx by tendon sheaths, bowstringing occurs during motion, leading to adduction of the whole thumb. The FPL is mainly responsible for the DIP joint flexion and has small effects on the CMC joint. The DI differs from the other muscles, because activation does not result in movement about a defined axis. It rather moves the bases of the first and second metacarpal bone closer to each other, providing stability. (Brand and Hollister 1999)

The MCP Joint

The MCP joint is a condyloid joint with two main axes of rotation. It is therefore possible to perform flexion-extension and adduction-abduction movements. Additional axial rotation is possible only in mid-flexed position. The articular surface of the metacarpal phalanx is biconvex and has two asymmetric palmar prominences. The shape of the proximal phalanx matches the metacarpal surface and is, therefore, biconcave. During the movement, the proximal phalanx is not only rotated but also deviated. The deviation is mainly caused by the collateral ligaments and supported by the asymmetric shape of the articulate surface, which finally leads to pronation. Generally, possible movements depend on the position of the joint and the respective state of the four collateral ligaments. During extension, one pair of ligaments is tense, the other pair is lax. Axial rotation is not possible in this position. When the joint is slightly flexed, the tension ceases and allows for deviation and axial rotation. Flexion is accompanied by pronation of the proximal phalanx, since the ulnar collateral ligament is slightly shorter than the radial one. In total flexion, the pair of ligaments fixed to the palmar plate becomes tense and prohibits both axial rotation and deviation. (Brand and Hollister 1999)

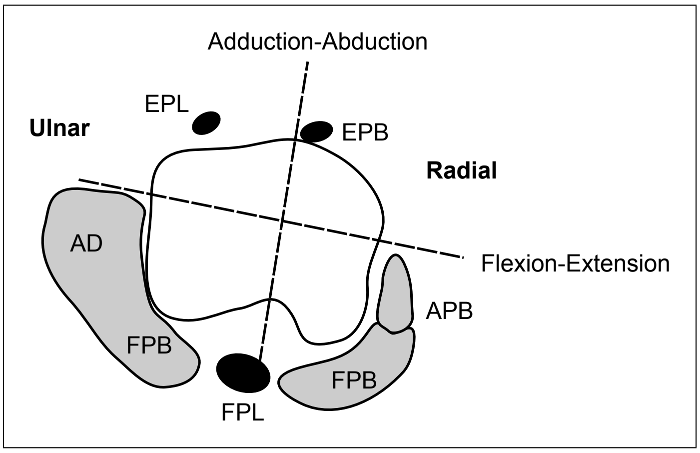

Figure 2.11.: Muscles and tendons passing the MCP joint, displayed in the cross section at the level of the flexion-extension axis. *Adapted from:* Brand and Hollister (1999)

Muscles responsible for movements at the MCP joint are shown in a cross sectional view at the level of the flexion-extension axis in figure 2.11. The APB causes abduction and contributes to opposition movement of the proximal phalanx. Similar to the CMC joint, both FPB and AP are essential for the pinch grip. The FPB allows flexion only, whereas the AP is a flexor and an adductor. Extension is achieved by the EPB and the EPL. The EPL is stronger and able to adduct the proximal phalanx, depending on the bowstringing of the tendon. The FPL only has a small effect on the MCP joint. (Brand and Hollister 1999)

The IP Joint

The movement of the IP joint is similar to a hinge joint with one degree of freedom, allowing flexion and extension. Due to the shape of the articular surfaces and the alignment of the ligaments, conjunct rotation occurs. The articular surface of the proximal phalanx has an ulnar prominence with larger radius of curvature and reaching further distally. The ulnar collateral ligament is slightly shorter than the radial ligament. In combination with the asymmetric shape of the articular surfaces, this leads to a small movement of pronation.

There are only two muscles crossing the IP joint at the level of the flexion-extension axis, as depicted in figure 2.12. The FPL is responsible for the flexion and the EPL for the extension of the joint. (Brand and Hollister 1999)

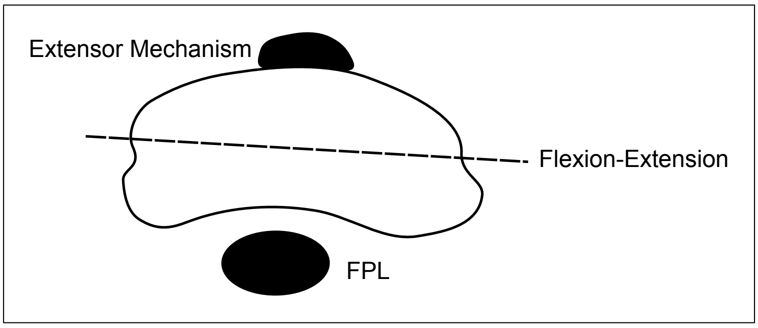

Figure 2.12.: Muscles and tendons passing the IP joint, displayed in the cross section at the level of the flexion-extension axis. *Adapted from:* Brand and Hollister (1999)

2.1.4. Conclusion

The investigation on the anatomy of diarthrodial joints shows that several different tissues contribute to joint stability and movement. Cartilage forms the articular surfaces, which constrain the movement together with the ligaments. In the muscle belly, force is produced and transmitted through tendons, which allow for an active movement of the joint. Hence, both material and geometrical data of cartilage, ligaments, muscles and tendons has to be determined in order to obtain physiologically plausible movements in a computer simulation. The remaining tissue surrounding the bone will, of course, resist any movement (Brand and Hollister 1999), but is not considered to be part of the diarthrodial joint mechanism. Based on the functional anatomy it is concluded that the saddle shape of the articular surfaces, seven ligaments and nine muscles contribute to the stability and movements of the CMC joint. All muscles except for the first DI serve the purpose of conducting rotational movements about the assumed flexion-extension or adduction-abduction axes.

2.2. Biomechanics

The anatomy explains the morphological and physiological aspects of the body in great detail, but is not concerned with the mechanical description of the tissues involved. Biomechanics is a modern field of science that applies mechanics to biology, i.e. living systems (Fung 1993). In this case, the word “mechanics” covers not only force, motion and strength of material, but also thermodynamics, heat and mass transfer and much more. To be able to build a simulation consisting of biomechanical components, it is inevitable to understand differences between the characteristics of organic and inorganic materials. In the following sections, typical material properties of soft tissues such as ligaments, muscles, tendons and cartilage are elucidated. Finally, different possible mechanisms of lubrication in diarthrodial joints are explained.

2.2.1. Mechanical Properties of Living Tissues

In classical mechanics, material is assumed to show linear-elastic behaviour within certain boundaries. Within these boundaries, typically two constants are sufficient for its definition, such as the Young’s modulus and the Poisson ratio. Living tissues behave more complexly, hence, different ways of describing the material are necessary. In order to deal with this complexity, parameterized curves are fitted to experimental data, delivering approximations to the behaviour of the actual

tissue. However, there are some general properties that help to understand overall characteristics of living tissues. The remainder of this section deals with these properties.
Material properties of tissues always depend on their composition of fibres. Especially two types of fibres, elastin and collagen, have great impact on material characteristics. Elastin is linear elastic and extremely compliant, allowing lengthening of $200\,\%$ without permanent deformation. Collagen, in contrast, is very stiff. It allows only $10\,\%$ of strain. Depending on the purpose, tissues contain more elastin or collagen. Tissues that are used for transmitting force or stabilizing joints, such as ligaments, contain mainly collagen. Collagen is a very stiff material that seems to have linear characteristics. Hence, comparing stress-strain curves of steel to those of collagen, they seem to behave similarly within certain strains. However, living tissues, also collagen fibres, generally show nonlinear characteristics. The stress-strain curve (figure 2.13) typically consists of four stages:

- *Unfolding*: Elements of the tissue unfold, little stress is induced
- *Alignment*: Elements gradually align themselves with the stress
- *Stiffening*: Elements are aligned with the stress, steep increase of stress
- *Failure*: Fibres tear apart, finally the tissue is totally separated

This curve looks different for each tissue, depending on its composition of collagen and elastin. Higher amounts of collagen result in a steep curve with a very small region of nonlinearities due to unfolding and alignment. (Brand and Hollister 1999)

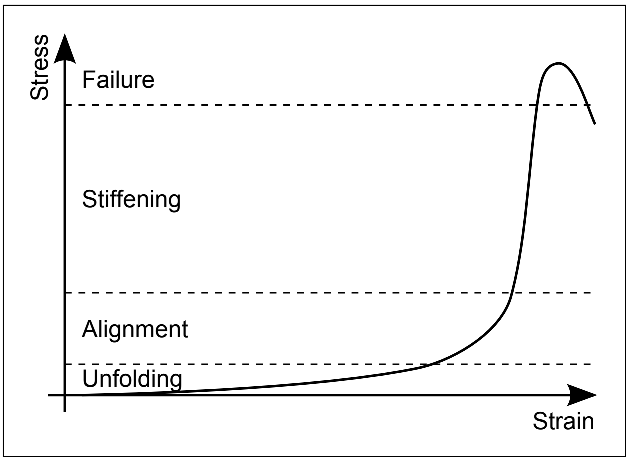

Figure 2.13.: A general stress-strain curve of living tissues, labelled with the typical four stages from unfolding to failure. *Adapted from:* Brand and Hollister (1999)

In biological structures, there is neither pure elasticity nor pure viscosity. Most tissues are viscoelastic, due to fluids and free cells in between an elastic matrix. If stress is imposed on the tissue, those fluids are moved. As soon as it is released, the original shape is gradually restored by the elastic components. Living tissues also show effects of creep and growth. Constant strain results in permanent lengthening of the composite tissue, whereas disuse causes the tissue to shorten. This happens especially with tissues that are very compliant, such as the skin. Noncompliant tissues such as ligaments tend to get thicker and stronger rather than longer. (Brand and Hollister 1999)

As a result of viscoelasticity, the material responds differently depending on its history and the strain-rate. However, it is assumed, that after a certain number of cycles of loading and unloading, the stress-strain curve remains steady and almost strain-rate independent. Hence, before the typical stress-strain curve of any tissue is measured, it is preconditioned by conducting several cycles of loading and unloading. The unloading curve still differs slightly from the loading curve, indicating viscoelastic properties. If loading and unloading is treated separately, the theory of elasticity can be applied to describe mechanical properties. This property is called pseudoelasticity. (Fung 1987)

2.2.2. Mechanical Properties of Ligaments

Ligaments serve the purpose of stabilizing the joints and consist mainly of collagen (Martin 1998). They show the typical behaviour of living tissues, including both a nonlinear stress-strain relationship and viscoelastic effects. As a result, ligaments behave strain-rate and history dependent: Higher strain-rates increase the stiffness, but repeated preconditioning cycles gradually reduces this sensitivity (Wang et al. 1997). Under constant deformation, internal stress reduces over time, which is called relaxation. If a constant load is applied, the tissue creeps, i.e. elongates over time. Both relaxation- and creep-rate are dependent on the current strain of the ligament (Wang et al. 1997).

It is obvious, that is hard to develop a model which accounts for all the effects mentioned above. If time dependence is neglected, the nonlinear stress-strain curve suffices to describe the behaviour of the material. However, these curves still depend on the number of preconditioning cycles and the applied strain-rate. If time dependent behaviour of the ligament should be accounted for, also creep- and relaxation have to be modelled. In this case, the creep is displayed as a function of strain over time under constant loading, whereas relaxation is shown as stress over time, under constant strain.

In literature, there are several approaches of modelling the stress-strain or force-strain curve, neglecting time dependent behaviour (Valero-Cuevas et al. 2003, Blankevoort et al. 1991, Crowninshield and Johnson 1976) but also approaches which try to incorporate time dependence (Hirokawa and Tsuruno 1997, Peña et al. 2007, Wang et al. 1997). This means, that ligaments are either modelled as nonlinear-elastic (time independent) or viscoelastic (time dependent) materials. It has to be mentioned, that the range of material parameters found in literature is large and conditions of the measurements are partly not mentioned. Hence, the applicability of the data to the intended purpose has to be verified carefully.

Nonlinear-elastic Approach

Sancho-Bru et al. (2001) and Blankevoort et al. (1991) show modelling approaches of the nonlinear force-strain curves of collateral ligaments of the MCP joint of the finger and the ligaments of the knee, respectively. Sancho-Bru et al. (2001) proposes a quadratic curve with a stiffness constant $K = 750\,\mathrm{N/cm^2}$ and a ligament-specific resting length l_0. The force F is expressed as a function of the current ligament length l:

$$F = K(l - l_0)^2 \tag{2.1}$$

Blankevoort et al. (1991) provides a formula for predicting the force of knee ligaments and accounts for the transition of a nonlinear to a linear region. The nonlinear region is also quadratic with a ligament-specific stiffness constant K and a reference strain $\epsilon_l = 0.03$. For knee ligaments, K

ranges between $1000\,\mathrm{N}$ and $9000\,\mathrm{N}$. In this approach, F is expressed as a function of the current strain $\epsilon = (l - l_0)/l_0$:

$$F = \begin{cases} \frac{1}{4}K\frac{\epsilon^2}{\epsilon_l} & \text{for } 0 \le \epsilon \le 2\epsilon_l \\ K(\epsilon - \epsilon_l) & \text{for } \epsilon > 2\epsilon_l \\ 0 & \text{for } \epsilon < 0 \end{cases} \tag{2.2}$$

Since these approaches do not account for ligament architecture, the predicted forces show large deviations, as displayed in figure 2.14 (a). For reasons of comparison, values for the cross sectional area (CSA) have to be determined. The CSA of the collateral ligament of the MCP joint was estimated to be $7.27\,\mathrm{mm}^2$ by averaging the data from Nanno et al. (2006), the CSA of the posterior cruciate ligament of the knee was estimated from Harner et al (1995) to be $50\,\mathrm{mm}^2$. Dividing the force by the respective CSA, the stress-strain curves of figure 2.14 (b) can be calculated.

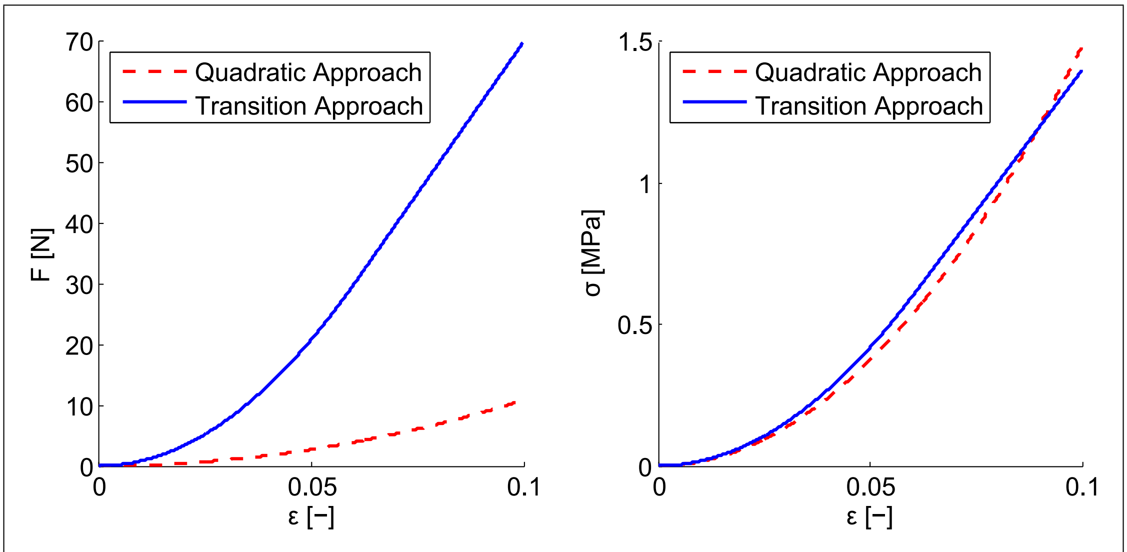

(a) Force-Strain

(b) Stress-Strain

Figure 2.14.: Comparison of different approaches for modelling the force-strain and stress-strain curves of ligaments

The two approaches do not deliver the same, but comparable results. Sancho-Bru et al. (2001) does not account for a linear region, which means, that this approach might only be valid for small strains. Since under physiological conditions the strain will hardly exceed the nonlinear region (Viidik 1987), the formula used by Sancho-Bru et al. (2001) is considered sufficient for modelling joint movements.

Resting lengths and estimations for the CSAs of thumb ligaments are found in the literature, such as Tan et al. (2011) for the unstrained length of CMC ligaments and Nanno et al. (2006) for the unstrained length of CMC ligaments as well as their respective CSAs.

Viscoelastic Approach

The nonlinear-elastic Approach considers the ligament to respond like a nonlinear spring. By adding a dashpot in series or in parallel to the spring, time dependent behaviour is achieved.

The series assembly of a spring and a dashpot is called Maxwell body and shows the effect of relaxation. If the dashpot is put in parallel to the spring, the resulting assembly is called a Kelvin-Voigt body and creeps under a constant load. Since the Maxwell fluid deflects infinitely under constant load, and the Kelvin-Voigt body is not capable of producing the effect of relaxation, they are typically combined to model biological tissues. The combination of two springs and a dashpot is mathematically simple and mostly sufficient for modelling purposes (McMahon 1987). Wang et al. (1997) shows that nearly all viscoelastic effects can be modelled using a nonlinear Zener model. It consists of two nonlinear springs with stiffness $k_1(x)$ and $k_2(x)$ and a dashpot with viscosity η, as displayed in figure 2.15. However, the required parameters for ligaments are not available as of this writing.

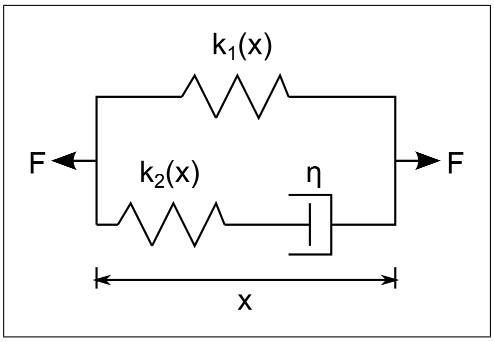

Figure 2.15.: A nonlinear Zener model used for incorporating time dependent material behaviour of ligaments. *Adapted from:* Wang et al. (1997)

In general, the disadvantage of the presented models is that they only describe material behaviour in one axis. More complex models are developed for the application in finite element analysis (FEA), such as the anisotropic visco-hyperelastic model of Peña et al. (2007). Such models focus on the accurate prediction of internal stresses and are not considered sensibly applicable for studying joint stability and movement.

2.2.3. Mechanical Properties of Muscles

Muscles are considered the motors of the body. To model them properly, it is not enough to take only active forces into consideration. Muscles consist of several sarcomere units which are able to contract and exert tension actively, but they show passive elastic behaviour as well. This leads to a tension in the muscle when it is passively stretched. If the muscle is released again, it springs back to its physiologic resting length. In this position, the muscle is able to exert the maximum active force. As it is stretched or contracted, less force can be produced. Figure 2.16 shows both active and passive force in one muscle, as well as their combination. The resulting curve is called Blix-curve. (Brand and Hollister 1999)

The maximum active force is not only dependent on the current length of the muscle, but also on the current velocity. Higher concentric velocities lower the maximum force, whereas higher eccentric velocities increase it, as displayed in figure 2.17.

The Hill muscle model accounts for length and velocity dependence of the maximum active force, as well as the passive force. It typically consists of three parts: A contractile element, a parallel elastic component and a series elastic component. The contractile element develops the active force depending on an activation level α, while the parallel elastic component produces the passive force. The series elastic component is sometimes referred to as the tendon elasticity, but in fact,

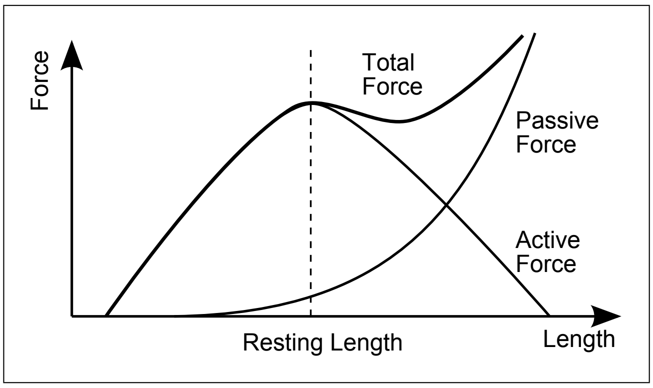

Figure 2.16.: A general force-length curve visualizing the length dependence of both the active and passive force of muscles. *Adapted from:* Brand and Hollister (1999)

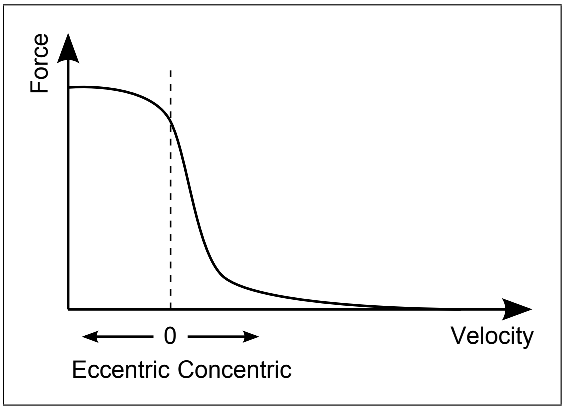

Figure 2.17.: A general force-velocity curve visualizing the velocity dependence of the active muscle force. *Adapted from:* Robertson and Gordon (2004)

is just a part of the model without true anatomical correspondence.(Robertson and Gordon 2004) Since both the active and passive force of a muscle are dependent on the muscle architecture, parameters have to be determined individually for each muscle by experiments. Kaufman et al. (1991) developed an equation for normalized active muscle force which is dependent on muscle architecture index i_a. The architecture index is defined as the muscle fibre length l_f divided by the muscle belly length l_m:

$$i_a = \frac{l_f}{l_m} \tag{2.3}$$

The muscle force is normalized by the maximum muscle force F_{max} and the product of activation level α, length dependent normalized force F_l and velocity dependent normalized force F_v:

$$F = \alpha \cdot F_l \cdot F_v \tag{2.4}$$

F_l and F_v is calculated as follows:

$$F_l = e^{-\left[\frac{(\epsilon+1)^{[0.963+(1-1/i_a)]}-1}{0.353\cdot(1-i_a)}\right]^2} \tag{2.5}$$

$$F_v = \frac{0.1433}{0.1074 + e^{-1.409 sinh(3.2\dot{\eta}+1.6)}} \tag{2.6}$$

The contractile element velocity $\dot{\eta}$ depends on the strain rate $\dot{\epsilon}$ and the maximum strain rate $\dot{\epsilon}_{max}$. $\dot{\epsilon}_{max}$ ranges between $2.0\,\mathrm{s}^{-1}$ and $7.5\,\mathrm{s}^{-1}$ and depends on the composition of the muscle fibres. Sancho-Bru et al. (2001) uses $\dot{\epsilon}_{max} = 2.5\,\mathrm{s}^{-1}$ in a simulation of a human finger.
In order to calculate the absolute force, F_{max} has to be known. Architecture dependence of the maximum force is incorporated by the physiological cross sectional area (PCSA):

$$F_{max} = PCSA \cdot S_{max} \tag{2.7}$$

S_{max} is the maximum stress a muscle can bear and ranges from $10N\,\mathrm{cm}^{-2}$ to $100\,\mathrm{Ncm}^{-2}$ (Kaufman et al. 1991). Valero-Cuevas et al. (2003) uses $S_{max} = 35.4\,\mathrm{Ncm}^{-2}$ for the simulation of thumb moving muscles. However, it is obvious that S_{max} has a significant impact on the absolute muscle force and has to be chosen carefully.
The absolute passive force F_p of the muscle was expressed in dependence of i_a by Woittiez et al. (1983):

$$F_p = F_0 \cdot e^{(0.4911/i_a+0.2933)\cdot\Delta x} \tag{2.8}$$

F_0 is the passive force at the optimum length of the muscle and stated to be 6.5% of F_{max} by (Woittiez et al. 1984). In contrast to the active force, F_p is not normalized. Furthermore, F_p is a function of the deflection Δx, not the strain ϵ. When using this equation, Δx has to be inserted in the approriate unit, which is centimeter. A rough estimation is derived according to Woittiez et al. (1984), when taking into account that the passive force is 6.5% of F_{max} at $\epsilon = 0$ and 87% of F_{max} at $\epsilon = 0.3$. Data for the individual muscles can be found in the literature, such as Jacobson et al. (1992) and Lieber et al. (1992) for all of the thumb moving muscles.
Both active and passive force is transmitted by tendons. Due to morphological similarities, their material properties are comparable to those of ligaments (Viidik 1987). However, tendons are far stiffer than muscles and may be assumed to be infinitely stiff for modelling the muscle-tendon unit (Sancho-Bru et al. 2001).

2.2.4. Mechanical Properties of Articular Cartilage

Articular cartilage is a very complex material. The cartilage itself is considered to be porous, inhomogeneous, anisotropic and viscoelastic. Additionally, the interstitial flow of the synovial fluid influences the compressive behaviour tremendously. To account for both the cartilage and the synovial fluid, biphasic theories are applied to determine material properties. Since the material undergoes large deflections under physiological conditions, geometric nonlinearties have to be incorporated. (Woo et al. 1987)
Many approaches of modelling compressive behaviour of articular cartilage are found in literature: Woo et al. (1987) focuses on the time dependent behaviour due to interstitial fluid flow, Chen et al. (2001) and Chen et al. (2001) divide the cartilage into homogeneous, isotropic layers and Guo et al. (2009) and Blankevoort et al. (1991) assume the whole cartilage to be homogeneous, isotropic and even linear elastic. The latter approach, even though seemingly oversimplified, serves as a good approximation if the cartilage is loaded and unloaded within a short range of time (Hori and Mockros 1976). Only if the load is applied for a very long time, time dependent behaviour has to be incorporated. The creep time constant resulting from the biphasic theory of Woo et al. (1987) is approximately 40 minutes. It is obvious that creep has minor influence on joint movements. It might, however, be interesting to know the equilibrium modulus of elasticity, for instance, to conduct quasi-static analysis. This equilibrium modulus of elasticity is also called aggregate modulus and serves as a measure of the stiffness of the elastic phase, when the whole fluid is ceased (Mansour 2009). Hence, two approaches are considered in the following sections: The fast response and static response.

Fast Response

For the fast response of articular cartilage, it is assumed to be a Hookean material. This means that is simplified to be homogeneous, isotropic and linear elastic for small strains. In order to determine the material behaviour, two constants are required: The Young's modulus E and the Poisson ratio ν. For fast responses, the values of E range between $5\,\mathrm{MPa}$ and $15\,\mathrm{MPa}$ and ν is close to 0.5 according to Blankevoort et al. (1991). Hori and Mockros (1976) gives an overview of existing values in literature (table 2.3).

$E[\mathrm{MPa}]$	$\nu[-]$
11.63	0.424
5.06	0.471
7.87	0.473

Table 2.3.: Hookean material parameters of human articular cartilage. *Adapted from:* Hori and Mockros (1976)

Generally, the stiffness decreases with increasing loading times. Blankevoort et al. (1991) uses $E = 5\,\mathrm{MPa}$ and $\nu = 0.45$ as an approximation for a simulation of joint movement. In order to account for the geometric nonlinearties, Blankevoort et al. (1991) also suggests to implement an effect of stiffness increase:

$$\frac{d\sigma}{d\epsilon} = E(1 - \epsilon) \tag{2.9}$$

Both the linear and nonlinear stress-strain curve of the articular cartilage in fast response are depicted in figure 2.18.

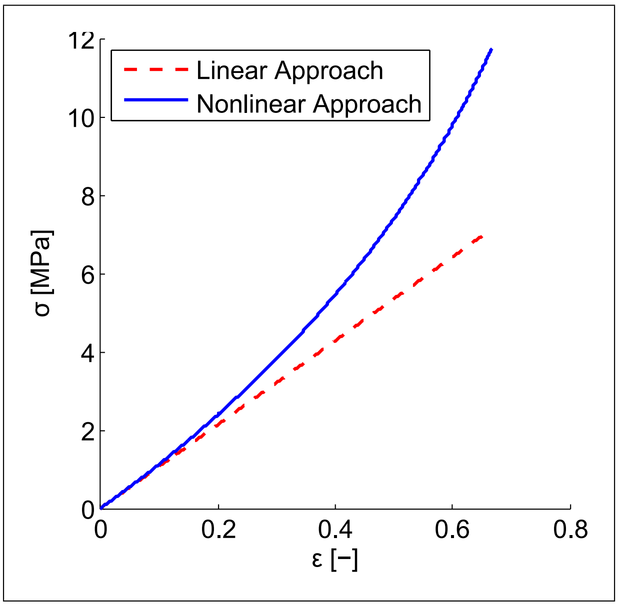

Figure 2.18.: Comparison of the linear and nonlinear fast response stress-strain curves of human articular cartilage

Static Response

Stiffness of articular cartilage in the static case is determined by the aggregate modulus H_A. H_A is measured in a confined indentation test, where a porous indenter compresses the cartilage with a constant load. The cartilage creeps until an equilibrium position is reached. Chen et al. (2001) divided the cartilage into eight layers, which are assumed to be approximately homogeneous. Indentation tests were performed on all layers separately, and also altogether, assuming the whole cartilage to be homogeneous. The experiment showed that H_A increases with depth from the surface, and also with strain. Chen et al. (2001) conducted similar tests for the whole cartilage as a homogeneous unit and expressed the material stress σ as a function of stretch $\lambda = \epsilon + 1$:

$$\sigma = \frac{H_{A0}}{4}\left[1 + 0.9(\lambda - 1)\right]\left[\frac{\lambda^4 - 1}{\lambda^3}\right] \tag{2.10}$$

H_{A0} is the equilibrium modulus for small strains and was determined experimentally to be $H_{A0} = 0.47 \pm 0.11\,\mathrm{MPa}$ for full thickness of the cartilage. The stress-strain curve resulting from formula 2.10 is shown in figure 2.19.

Similar to the ligaments, all the modelling approaches elucidated in this section only account for uniaxial loading. Further analysis of cartilage behaviour are, for instance, conducted using FEA (Bell et al. 2009), by defining several isotropic or transversely isotropic layers.

2.2.5. Friction between Articular Surfaces

For any movement of joints, it is necessary for the surfaces to slide past each other. Similar to any other mechanical system, this sliding is restricted by a frictional force caused by microscopic

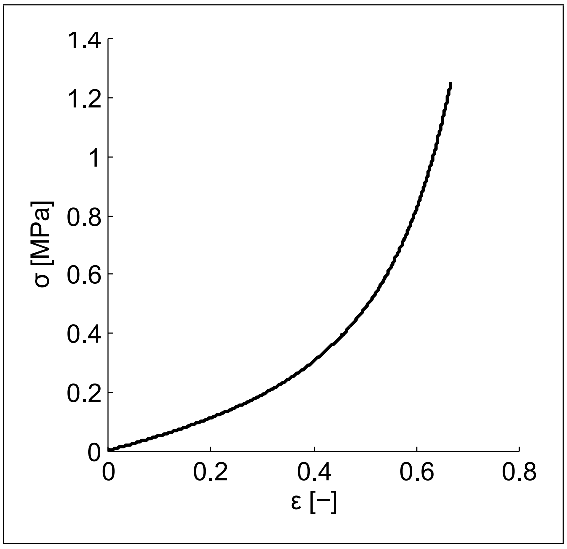

Figure 2.19.: Static response stress-strain curve of human articular cartilage

ridges at the surfaces. In the most general case, the tangential friction force Q depends on the compressive force P, the tangential velocity v_t and a friction coefficient μ (Johnson 1985):

$$Q = -\frac{v_t}{|v_t|} \cdot \mu \cdot P \tag{2.11}$$

Static friction coefficients are higher than sliding friction coefficients. In technical machines, μ ranges between 0.3 for unlubricated and 0.05 for lubricated sliding (Martin 1998). For human joints in motion, μ is typically very low: Charnley (1960) conducted friction measurements on the human knee and found values from 0.005 to 0.023. Clarke et al. (1975) investigated friction in the human hip and states μ to range between 0.001 and 0.03.

It is agreed on in literature, that friction in diarthrodial joints is low (Woo et al. 1987). An et al. (1990) even finds friction to be totally negligible for analysis of joint motion. It is, however, controversially discussed which effects lead to almost frictionless sliding. Several different, partly contradictory, lubrication mechanisms are said to contribute to the reduction of friction forces, such as: Boundary, squeeze film, hydrodynamic, weeping and boosting lubrication (Martin 1998). To overcome the roughness of the surfaces, all these mechanism are based on separating the surfaces. Boundary lubrication diminishes friction by placing a very thin liquid on the surfaces, causing their projections to be held slightly apart. Since the surfaces are not totally separated, this mechanism does not deliver the best lubrication results.

The theory of squeeze film lubrication claims that the viscoelasticity of synovial fluid contributes largely to the separation of the surfaces. During a typical motion, such as walking, the leg is unloaded when swinging forward and loaded when reaching the ground. While swinging forward, the surfaces are separated. When reaching the ground, the viscoelasticity of the synovial fluid resists the movement of the surfaces towards each other, hence, prolongs the time until they are in contact again. In the meantime, the friction is low.

Hydrodynamic lubrication is based on fast relative movements between the surfaces and an interstitial lubricant. During slow movements, lubrication is similar to thin film boundary lubrication, hence, friction is high. When the surfaces move past each other rapidly, friction between adjacent fluid molecules drags intervening fluid in the space between them, causing hydrodynamic pressure which forces them apart. Thus, the friction is determined only by intermolecular friction of the fluid. If the fluid is Newtonian, shear stress increases linearly with strain rate and causes the total friction of the contact to rise again at very high velocities. Synovial fluid diminishes this effect due to its thixotropic behaviour. The slope of the stress-strain rate curve in thixotrophic fluids, unlike Newtonian fluids, decreases with increasing strain rates.

Weeping lubrication could be compared to hydrostatic lubrication. It is based on the porous structure of the cartilage, which is filled with fluid. This fluid is supposed to be a filtrate of synovial fluid, leaving molecules on the surface that are too big to surpass the pores. The theory of weeping lubrication claims that this filtrate is pressed out of the cartilage under compression, contributing to the separation of the surfaces.

Boosted lubrication also assumes the synovial fluid to be filtrated by the porous cartilage. However, contradictory to weeping lubrication, it is claimed that under compression the water is pressed into the pores, leaving behind a highly viscoelastic, gel-like substance which ensures separation of the surfaces.(Martin 1998)

Generally, these theories are all based on the fact that the surfaces are separated in order to reduce friction. Charnley (1960) argues that total separation of the surfaces is unlikely to occur due to physiological conditions in human joints: Loads and pressures are large, relative velocities are low and the cartilage is very compliant. It is obvious that these conditions contradict especially the theory of hydrodynamic lubrication.

2.2.6. Conclusion

The previous sections showed that living tissues behave very complexly. Unlike inorganic materials, it is very hard to describe their material properties including all effects such as history dependence, viscoelasticity and growth. Furthermore, available material data always has to be verified carefully, since the conditions of the measurements influence the result significantly. In order to incorporate the characteristics of living tissues in a biomechanical model, simplifications and assumptions are inevitable. The choice of the material model depends on the purpose of the simulation, but also on the availability of the material data. A complex model which accounts for most effects is not applicable in a simulation as long as the necessary model parameter are not provided. Due to all these uncertainties, it is considered sensible to focus on the well investigated and determined, mostly uniaxial, material models.

2.3. Contact Simulation

It has been mentioned that the shape of the surfaces heavily influences the joint kinematics. In order to account for this shape in a simulation, the surfaces have to be in contact. Naturally, contacting surfaces do not penetrate each other, but are displaced and deformed under the prevailing contact forces. Hence, in the following sections, general terminology and formulation of contact mechanics are elucidated. Subsequently, computational contact methods are introduced.

2.3.1. Contact Mechanics

Whenever two solid bodies contact each other, stresses and deformations arise. The field of contact mechanics deals with methods of computing these stresses assuming certain simplifications. Johnson (1985) delivers a great introduction to different approaches such as the Hertzian contact theory and the elastic foundation model.

Generally, two types of contacts can be distinguished: The conforming and the non-conforming contact. If the contact area is large compared to the dimensions of the bodies, the contact is conforming. This happens if the shape of the contacting surfaces is almost congruent. If both surfaces are convex, the contact area is comparably small and the contact is non-conforming. Most mathematical models are valid only in case the contact is non-conforming. At the moment of the first contact, the surfaces touch at a single point. This point O represents the origin of the contact coordinate system. The z-axis coincides with the common normal of the tangent planes of the surfaces, which is spanned by the x- and y-axes. In this plane, the shape of the surfaces is described by $z_1(x, y)$ and $z_2(x, y)$, respectively. The sum of z_1 and z_2 yields the separation h:

$$h(x, y) = z_1(x, y) + z_2(x, y) \tag{2.12}$$

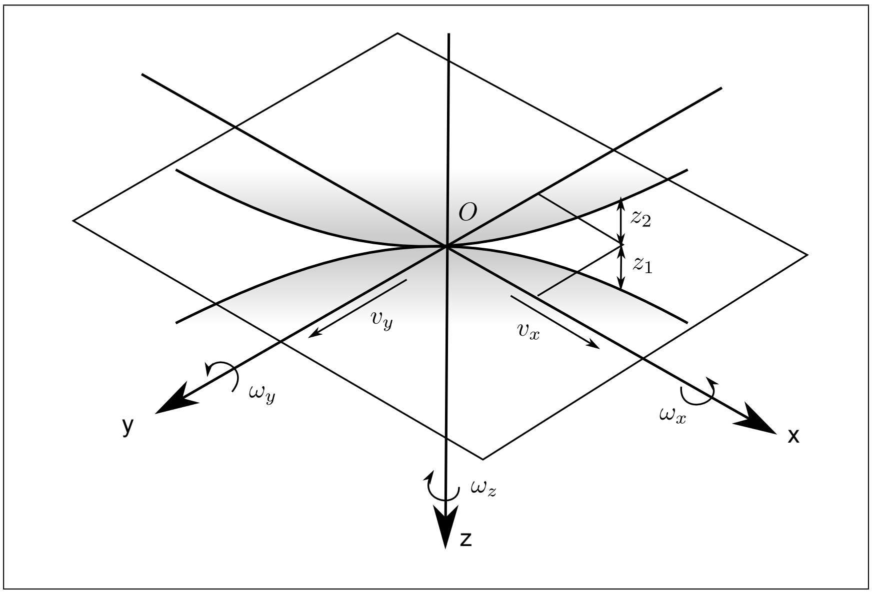

Figure 2.20.: The coordinate system of two bodies in contact at a single point. *Adapted from:* Johnson (1985)

Figure 2.20 shows the contact coordinate system of a non-conforming contact. In this coordinate system, different kinds of relative motions and forces can be described. At a given instant, the first body has velocity $\mathbf{v}_1$ and angular velocity ω_1 at point O and the second body has velocities $\mathbf{v}_2$ and ω_2. If the contact surfaces meet at one point, i.e. they are neither overlapping nor separated, the z-components of $\mathbf{v}_1$ and $\mathbf{v}_2$ have to be equal. This can be expressed as the condition of continuous contact:

$$v_{z1} = v_{z2} = v_{zO} \tag{2.13}$$

Sliding is then defined as the relative linear velocity between the surfaces:

$$\begin{aligned} \Delta v_x &= v_{x1} - v_{x2} \\ \Delta v_y &= v_{y1} - v_{y2} \end{aligned} \tag{2.14}$$

Rolling is the relative angular velocity between the bodies about the x- or y-axis:

$$\begin{aligned}\Delta\omega_x &= \omega_{x1} - \omega_{x2} \\ \Delta\omega_y &= \omega_{y1} - \omega_{y2}\end{aligned} \tag{2.15}$$

If the surfaces rotate about the z-axis, the relative motion is called spinning:

$$\Delta\omega_z = \omega_{z1} - \omega_{z2} \tag{2.16}$$

The motion of contacting surfaces always has to satisfy formula 2.13, and is a combination of sliding, rolling and spinning.

The resulting forces transmitted from one surface to another are the normal force P and the tangential force Q. The normal force P acts along the z-axis and is generally compressive. Q lies in the x-y plane and is sustained by friction. In pure sliding, Q has its maximum value in the direction opposed to the relative velocity:

$$\begin{aligned}Q_x &= -\tfrac{\Delta v_x}{|\Delta v|} \cdot \mu \cdot P \\ Q_y &= -\tfrac{\Delta v_y}{|\Delta v|} \cdot \mu \cdot P\end{aligned} \tag{2.17}$$

Since the bodies are compressed by the Force P, the contact point widens up to a contact area. This allows moments to be transmitted as well. Moments about the x- and y-axis are called rolling moments, the moment about the z-axis is the spinning moment. As a further result, the distribution of the forces at the contact area S can be described as the normal traction p and the tangential traction q. In case warping of the surface is neglected, the conditions for equilibrium over the area S can be described as follows:

$$\begin{aligned}P &= \int p\, dS \\ Q_x &= \int q_x\, dS \\ Q_y &= \int q_y\, dS\end{aligned} \tag{2.18}$$

The distribution functions of the tractions are derived by applying the Hertz theory of elastic contact. It allows for the calculation of the shape of the contact area, and the surface normal tractions. Thus, local stresses and deformation in both bodies can be computed. In order to simplify calculations, Hertz theory makes use of the elastic half-space theory and is only valid in case the surface profiles are parabolic and the surface contact is frictionless. Additionally, the application of the elastic half-space theory implies that the dimensions of the contact area are small compared to the radii of curvature of the undeformed surfaces. If all these conditions are satisfied, it is possible to idealize the contacting bodies as two semi-infinite elastic solids, bounded by a plane surface, and therefore enables the use of elasticity theory.

In case all simplifications are applicable, the pressure distribution due to an external load can be calculated. If the load is applied to both bodies, distant body fixed points T_1 and T_2 are displaced by an amount of δ_1 and δ_2 along the z-axis towards point O. In case no deformation occurred, the bodies would overlap, as displayed with a dashed line in figure 2.21.

Due to contact pressure, the surfaces are displaced parallel to the z-axis by an amount of u_{z1} and u_{z2}, respectively. Inside the contact area, the elastic displacements can be expressed as follows:

$$u_{z1} + u_{z2} = \delta_1 + \delta_2 - h \tag{2.19}$$

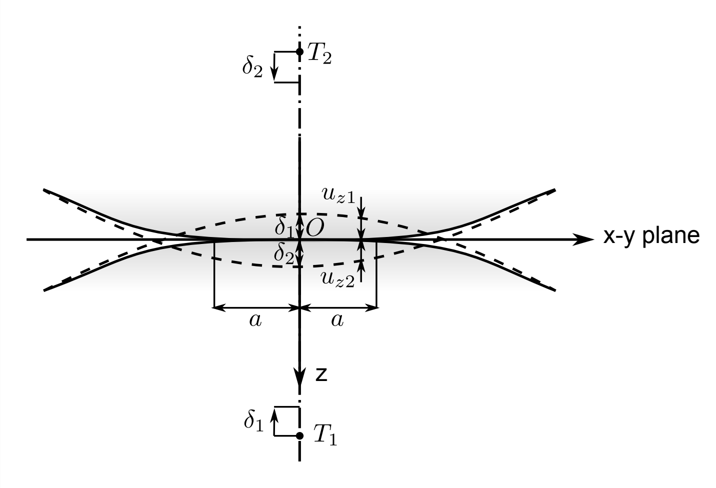

Figure 2.21.: Deformed and undeformed surfaces of two bodies in contact. *Adapted from:* Johnson (1985)

Subsequently, a pressure distribution $p(x, y)$ has to be found, which is acting over the contact area S and produces displacements u_{z1} and u_{z2} satisfying Formula 2.19 within S. The problem was solved by Hertz for a different contact situations. In case of two contacting bodies of revolution, the pressure acts on a circular contact area with radius a and produces a distribution $p(r)$:

$$p(r) = p_0\sqrt{1 - (r/a)^2} \tag{2.20}$$

Based on this formula, radius a of the contact area, mutual approach of distant points δ and the total applied load P can be computed. Even though useful in certain cases, it has to be kept in mind that these formulas are valid only for the given contact situation and only if mentioned simplifications are applicable. Furthermore, calculating the surface displacements u_z is difficult as the displacement at any point depends on the distribution of pressure throughout the whole contact. In order to find the pressure at any point of the solids, it is therefore necessary to solve integral equations. This is avoided if the elastic half-space is replaced by an elastic foundation. The elastic foundation can be imagined as a set of springs with height h and elastic modulus K, fixed on a rigid base, as depicted in figure 2.22.

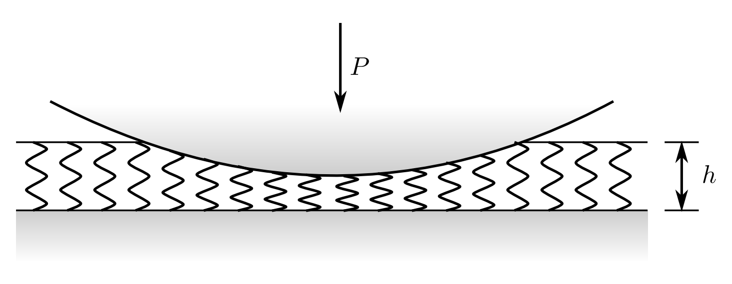

Figure 2.22.: A schematic depiction of the elastic foundation model. *Adapted from:* Johnson (1985)

The springs are compressed by a rigid indenter with a surface equal to the sum of the surfaces of the two contacting bodies:

$$z(x, y) = z_1(x, y) + z_2(x, y) \tag{2.21}$$

Since there is no interaction between the springs, shear is neglected. The elastic displacement can therefore be expressed simply as:

$$u_z(x, y) = \begin{cases} \delta - z(x, y) & \text{for } \delta > z \\ 0 & \text{for } \delta \leq z \end{cases} \tag{2.22}$$

As a result, the pressure at any point depends only on the displacement at this point:

$$p(x, y) = (K/h) \cdot u_z(x, y) \tag{2.23}$$

This simplification may cause inaccuracies compared to Hertz theory of contact. Compensation can be achieved by applying correction values for the ratio K/h. If K is considered to be a material constant, h has to be increased in proportion to contact width a. In case the elastic foundation is used to model a point contact, the calculated pressure might be only half of that calculated based on the equations of Hertz. Despite these drawbacks, the elastic foundation serves as a good approximation whenever elastic half-space theory cannot be applied. Furthermore, it is easily adapted for tangential loading and viscoelastic solids.

2.3.2. Contact in Multi Body Simulations

There are several methods of simulating mechanical systems. Finite element analysis (FEA) is far spread and able to predict stresses and deformations in elastic bodies, due to applied forces and displacements. However, it is often necessary to model systems consisting of many different, fast moving parts, thus inertial effects are not negligible anymore. Even though it is possible to conduct such simulations using FEA, the development of the model is complex and the calculation might be very time-consuming. Multi body simulations (MBS) are based on the theory of multi body dynamics and allow for the prediction of the kinematics and dynamics of simplified mechanical systems. In contrast to FEA, MBS is mainly concerned with the movement of rigid bodies. In classical MBS, these bodies have a certain mass and are connected by massless links, such as springs or bushings. Additionally, kinematic constraints and joints can be defined. (Rill and Schaeffer 2010)

Principles of a Multibody Simulation

In a MBS, the behaviour of each body is determined based on rigid body dynamics. Hence, it is sufficient to define a specific coordinate system and inertial properties for each body. The position, orientation and velocities are defined with respect to a reference coordinate system. Figure 2.23 shows the position of a body with coordinate system K fixed to point S relative to the reference coordinate system 0.

The position of the body is defined by the vector $\mathbf{r}$, and the orientation is determined by the Euler angles α, β and γ. Incorporating the translational velocity $\mathbf{v}$ and the angular velocity ω, the state vector $\mathbf{x}$ of the body is defined as follows:

$$\mathbf{x} = \begin{bmatrix} r_x & r_y & r_z & \alpha & \beta & \gamma & v_x & v_y & v_z & \omega_x & \omega_y & \omega_z \end{bmatrix}^T \tag{2.24}$$

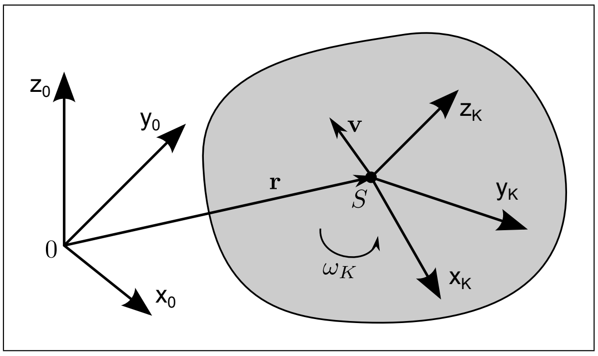

Figure 2.23.: Representation of a rigid body in a MBS. *Adapted from:* Rill and Schaeffer (2010)

Position and translational velocities are defined with respect to the reference coordinate system 0, whereas the angles and angular velocities are expressed in K. In order to describe the motion of the body, the equation of state $\dot{\mathbf{x}} = f(t, \mathbf{x})$ has to be established. For this purpose, both kinematic and dynamic differential equations are used. Kinematic differential equations are:

$$\begin{bmatrix} \dot{r}_x \\ \dot{r}_y \\ \dot{r}_z \end{bmatrix} = \begin{bmatrix} v_x \\ v_y \\ v_z \end{bmatrix} \tag{2.25}$$

$$\begin{bmatrix} \dot{\alpha} \\ \dot{\beta} \\ \dot{\gamma} \end{bmatrix} = \frac{1}{cos(\beta)} \begin{bmatrix} cos(\gamma) & -sin(\gamma) & 0 \\ sin(\gamma)cos(\beta) & cos(\gamma)cos(\beta) & 0 \\ cos(\gamma)sin(\beta) & sin(\gamma)sin(\beta) & cos(\beta) \end{bmatrix} \begin{bmatrix} \omega_x \\ \omega_y \\ \omega_z \end{bmatrix} \tag{2.26}$$

Making use of the principle of linear and angular momentum, dynamic differential equations are derived. The linear momentum is expressed in the reference coordinate system 0 and dependent on the applied force $\mathbf{F}_0$ and the mass m of the body:

$$m \cdot \dot{\mathbf{v}} = \mathbf{F}_0 \tag{2.27}$$

The angular momentum is expressed in the body fixed coordinate system K with the applied moment M_K and the inertia matrix $\mathbf{I}_K$:

$$\mathbf{I}_K \cdot \dot{\omega} = \mathbf{M}_K - \omega \times \mathbf{I}_K \cdot \omega \tag{2.28}$$

Formulas 2.25 to 2.28 result in a system of twelve first order, ordinary differential equations. Since this system of differential equations is nonlinear, it is generally necessary to solve it numerically. (Rill and Schaeffer 2010)

Contact Modelling

As described in the previous section, movement in a MBS only occurs if forces or moments are applied to a body. In order to model contacting bodies, it is necessary to develop equations which allow for the calculation of the contact forces as described in section 2.3.1. Two different approaches are elucidated in this section: The one-dimensional contact element and the polygonal contact model (PCM).

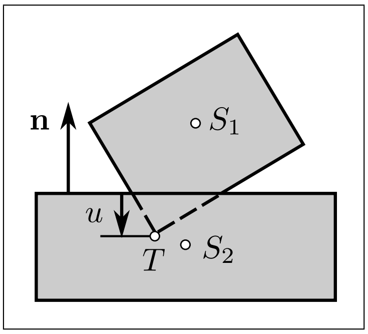

Figure 2.24.: Contact of two bodies in a MBS using a one-dimensional contact element. *Adapted from:* Rill and Schaeffer (2010)

Using the one-dimensional contact element is the simplest way to determine contact forces. It is assumed that the bodies penetrate each other in contact, which means that no deformation occurs. Figure 2.24 shows the bodies S_1 and S_2 in contact. Subsequently, a virtual spring-damper element with stiffness k and damping d is inserted at the surfaces of the two bodies. The normal contact force P is then calculated depending on the penetration depth u of point T:

$$P = \begin{cases} 0 & \text{for } u \geq 0 \\ -k \cdot u - d \cdot \dot{u} & \text{for } u < 0 \end{cases} \tag{2.29}$$

It is assumed that P only acts along the contact surface normal $\mathbf{n}$. Since the relative velocity v_t of the virtual point of contact in the tangential plane can be easily determined by kinematic equations, also a tangential force Q can be calculated using Coulomb's law of friction:

$$Q = -\frac{v_t}{|v_t|} \cdot \mu \cdot P \tag{2.30}$$

It is obvious that there are several simplifications: First, the normal contact force is assumed to be proportional to the penetration depth of a single point. The contact area is neglected completely. Second, contact calculation is only possible with an appropriate collision detection. This is easily done in the special case of modelling contact between a cuboid and a plane, but hard if the surfaces of the bodies are complexly shaped. In order to deal with these problems, Hippmann (2004) developed the polygonal contact model (PCM). PCM is capable of robustly detecting collisions and calculating contact forces, even for irregularly shaped contact surfaces and conforming contacts.

The calculations are based on the elastic foundation theory for the normal force and Coulomb friction for tangential forces. PCM is easily implemented in any MBS environment as a force element. Hence, it takes the kinematic state of each body as input (see formula 2.24) and delivers forces and moments as output. Additionally, polygonal surfaces of the bodies have to be defined. Polygonal surfaces consist of points in space which are connected by triangles or rectangles. Describing complexly shaped surfaces using polygons is simple, robust and wide spread in computer aided design (CAD) as well as in computer graphics. Problems are caused only if the surface contains holes and open edges.

Figure 2.25 gives an overview of how PCM works. There are mainly two kind of problems involved in the computation of the contact forces: Geometrical problems and problems of contact mechanics. The collision detection and the construction of intersection volumes are based on the surface geometry, whereas appropriate theory of contact mechanics has to be applied to find resulting forces and moments.

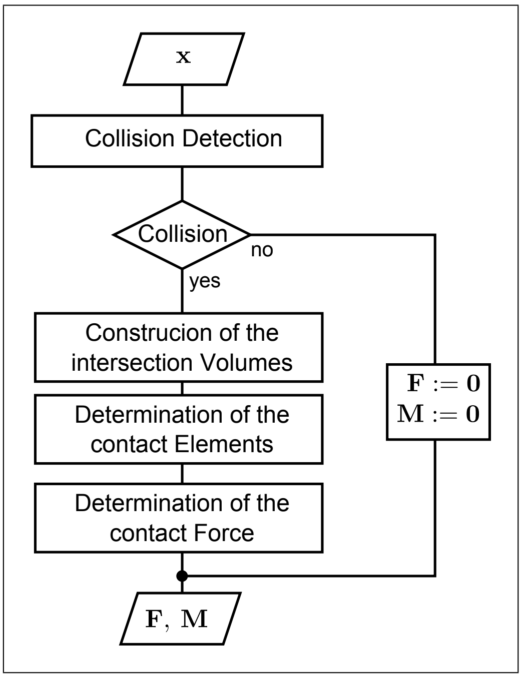

Figure 2.25.: A schematic depiction of the functionality of PCM. *Adapted from:* Hippmann (2004)

In order to detect a collision, intersecting triangles have to be found. For this purpose, computations have to be conducted for each possible pair of triangles. Even though very efficient algorithms are available to perform intersection tests, they might be time consuming in case of a high polygon count. PCM uses bounding volumes to avoid this weakness. Bounding volumes can be considered convex hulls, covering certain areas of the polygonal surface. By subdividing the whole surface into a hierarchy of cuboidal bounding volumes, a bounding volume tree can be determined. Subsequently, collisions between bounding volumes of different surfaces are detected. Collision detections are repeated for volumes of lower hierarchy, until finally intersecting triangles can be determined. Using this method, the computational time for collision detection is reduced drastically. Building the bounding volume tree might be time consuming as well, but has to be performed only once.

If no collision is detected, PCM terminates its calculations. In case intersecting triangles have been found, the volume of the intersecting surfaces has to be determined. The border of the contact area is defined by a polygonal line along the intersection lines of the triangles. Subsequently, polygons within this area are declared as active elements.

In order to compute the contact forces, contact elements are defined using the master-slave method. For this purpose, one surface is defined as master, with all its respective polygons. Each of these polygons subsequently produces a contact element. The depth of penetration u_{nk} is calculated by finding the distance between the centroid C_e of the master-polygon e and the point of intersection I in the plane of a slave-polygon f, as shown in figure 2.26.

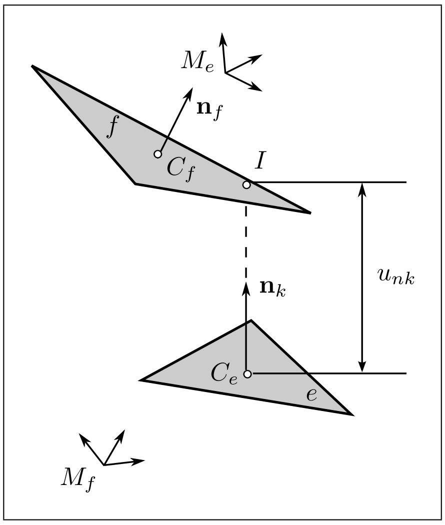

Figure 2.26.: Calculation of the penetration depth of a contact element in PCM. *Adapted from:* Hippmann (2004)

I is determined by intersecting the reversed surface normal $\mathbf{n}_k$ with the plane of f. The position of the contact element is assumed to be placed on an approximated contact surface in between the surfaces of the bodies. Hence, the ratio λ is introduced which is calculated using the stiffness constant c of the elastic foundation of each body:

$$\lambda = \frac{c_F}{c_E + c_F} \tag{2.31}$$

With λ, the position of the contact element C_k can be defined relative to the master-surface reference system M_e:

$$r_{C_k} = r_{C_e} + \lambda \cdot u_{nk} \cdot \mathbf{n}_k \tag{2.32}$$

It is obvious that the discretization of the master-surface influences the quality of the approximation of the contact forces tremendously. The surface with more detailled discretization should therefore be selected as master. To improve the results, 2-pass-mode can be selected in PCM. In 2-pass-mode, master-slave calculations are performed for each surface. The resulting forces and moments are averaged and returned to the MBS.

For each contact element, normal and tangential forces have to be determined. Similar to the one-dimensional force element, a force law is defined in order to calculate the contact normal force. This force law is dependent on the combined layer stiffness c, polygon area A_k and the penetration depth u_{nk}. The combined layer stiffness is calculated as follows:

$$c = \frac{c_E \cdot c_F}{c_E + c_F} \tag{2.33}$$

The body specific contact stiffnesses c_E and c_F are computed using the elastic modulus E and the Poisson ratio ν:

$$c_E = \frac{K_E}{h_E} = \frac{1 - \nu_E}{(1 + \nu_E)(1 - 2\nu_E)} \cdot \frac{E_E}{h_E} \tag{2.34}$$

$$c_F = \frac{K_F}{h_F} = \frac{1-\nu_F}{(1+\nu_F)(1-2\nu_F)} \cdot \frac{E_F}{h_F} \tag{2.35}$$

The contact normal force F_{nk} of each polygon consists of a spring force F_{ck} proportional to spring displacement u_{nk} and a damping force F_{dk} proportional to normal velocity v_{nk}:

$$F_{ck} = c \cdot A_k \cdot u_{nk} \tag{2.36}$$

$$F_{dk} = d \cdot A_k \cdot v_{nk} \tag{2.37}$$

$$F_{nk} = \begin{cases} 0 & \text{for } F_{ck} + F_{dk} \leq 0 \\ F_{ck} + F_{dk} & \text{for } F_{ck} + F_{dk} > 0 \end{cases} \tag{2.38}$$

The calculation of the contact tangential force F_{tk} is based on Coulomb's law of friction and thus a function of F_{nk} and tangential velocity v_{tk}:

$$F_{tk} = \begin{cases} \mu \cdot F_{nk} & \text{for } v_{tk} \geq v_\epsilon \\ \mu \cdot F_{nk} \cdot \frac{v_{tk}}{v_\epsilon}\left(2 - \frac{v_{tk}}{v_\epsilon}\right) & \text{for } v_{tk} < v_\epsilon \end{cases} \tag{2.39}$$

Formula 2.39 shows that PCM uses a quadratic regularization of Coulomb's law of friction with regularization velocity v_ϵ. If the tangential velocity drops below this value, the tangential force is reduced quadratically.

Due to typical conventions of MBS, the force and moment vectors of each contact element of body E are calculated using the coordinate system M_f of body F:

$$\mathbf{F}_k = F_{nk} \cdot \mathbf{n}_k + F_{tk} \cdot \frac{\mathbf{v}_{tk}}{v_{tk}} \tag{2.40}$$

$$\mathbf{M}_k = \mathbf{r}_{M_f C_k} \times \mathbf{F}_k \tag{2.41}$$

The output returned to the MBS is the sum of the individual vectors:

$$\mathbf{F}_E^{M_f} = \sum_k \mathbf{F}_k \tag{2.42}$$

$$\mathbf{M}_E = \sum_k \mathbf{M}_k \tag{2.43}$$

The calculations show that PCM is capable of calculating contact forces and moments based on the polygonal surfaces and the current state vectors. Hence, besides the required definition of the surfaces, it can be treated like any other force element in a MBS. It has to be kept in mind that PCM only approximates the contact forces based on a discrete version of the elastic foundation model. In order to obtain plausible results, the discretization of the surfaces has to be performed carefully.

2.3.3. Contact in Finite Element Analysis

Many engineering problems deal with describing internal states of bodies, such as the deformations of an elastic body undergoing external forces. Analytical solutions are often infeasible for complex materials and geometries. However, an approximation of the solution can be achieved by subdividing the complex system in finite number of simple elements. This procedure is called discretization and the first step of a finite element analysis. The approximated result should subsequently converge the analytical solution as the number of discrete variables increases. (Zienkiewicz et al. 2005)

Principles of FEA

FEA delivers solutions to many engineering problems in different fields, such as fluid mechanics, heat transfer or solid mechanics. The major steps required to conduct a FEA are, however, always the same:

- Discretization
- Selection of interpolation functions
- Development of the element matrix
- Assembly of the element matrices to obtain the global matrix
- Imposition of boundary conditions
- Solution of equations
- Additional, optional computations

In order to give a better understanding of these steps, the direct stiffness approach is introduced in the following. This approach is suitable for simple problems only, but involves each of the steps mentioned above. Additional solving methods are presented at the end of this section.(Madenci and Guven 2006)

In the following, a system of springs is assumed, which is fixed at a certain point and deforms as an external force F is exerted. Discretization of the system requires the definition of elements as well as connective points, which are called nodes. Since the system appears discretely from its nature, it is reasonable to define the springs as elements and connective points as nodes. Putting nodes and their respective connections into a table of connectivity, the step of discretization is finished.

Nodal displacement causes deformations within the elements. This dependence is expressed by the interpolation function. Based on this function, the element matrix $\mathbf{k}$ is derived. $\mathbf{k}$ is also called the stiffness matrix and relates force to nodal displacement. The stiffness matrix of a spring is derived easily by considering the forces f_1 and f_2 as a result of displacement u_1, u_2 and stiffness k:

$$f_1 = k(u_1 - u_2) \tag{2.44}$$

$$f_2 = -f_1 = k(u_2 - u_1) \tag{2.45}$$

Rewriting formula 2.44 and 2.45 in matrix form yields:

$$\begin{bmatrix} k & -k \\ -k & k \end{bmatrix} \begin{bmatrix} u_1 \\ u_2 \end{bmatrix} = \begin{bmatrix} f_1 \\ f_2 \end{bmatrix} \tag{2.46}$$

Denoting the displacement vector as $\mathbf{u}$ and the force vector as $\mathbf{f}$, the following general form is achieved:

$$\mathbf{k} \cdot \mathbf{u} = \mathbf{f} \tag{2.47}$$

The whole assembly is established in the same form, with global stiffness matrix $\mathbf{K}$, unknown nodal displacements $\mathbf{u}$ and the global force vector $\mathbf{F}$:

$$\mathbf{K} \cdot \mathbf{u} = \mathbf{F} \tag{2.48}$$

$\mathbf{K}$ and $\mathbf{F}$ can be computed by simply summarizing element stiffness matrices $\mathbf{k}$ and force vectors $\mathbf{f}$, respectively. In order to solve this system for the unknown displacements, boundary conditions have to be imposed. This can be done by either constraining the movement of certain nodes or by specifying nodal forces. Hence, either nodal displacements or external forces have be known. This leads to a linear system of equations, which can easily be solved for the unknown displacements $\mathbf{u}$. The last step of a typical FEA is to conduct additional calculations. In a system of springs, this could include the computation of element forces.

This direct stiffness approach demonstrates the principles of FEA in a simple way. In order to solve more complex systems, different methods, such as the method of weighted residuals or the variational approach have to be used. The former utilizes differential equations, for instance those of heat transfer or fluid mechanics, and delivers approximate solutions whereas the latter seeks the solution by extremizing a functional. In structural mechanics, this functional corresponds to the potential energy. (Madenci and Guven 2006)

Contact Modelling

In FEA, contact is generally modelled by imposing additional constraints to avoid penetration between the bodies. Since contacting areas are not known a priori, this leads to a nonlinear boundary value problem. There are two well known methods which allow to determine forces caused by these constraints: The Lagrange multiplier method and the penalty method. Both of them are described briefly in this section using a simple, one-dimensional example. In order to elucidate the two methods, they are applied to a one-dimensional mass-spring system, as shown in figure 2.27.

Before the problem is solved, a variational formulation is derived in order to specify the contact problem. The energy Π can be expressed as a function of the spring displacement u, with body mass m, spring stiffness k and gravitation constant g:

$$\Pi(u) = \frac{1}{2}u^2 - m \cdot g \cdot u \tag{2.49}$$

Without considering the restriction of the rigid support, the extremum can be found by variation:

$$\delta\Pi(u) = k \cdot u \cdot \delta u - m \cdot g \cdot \delta u = 0 \tag{2.50}$$

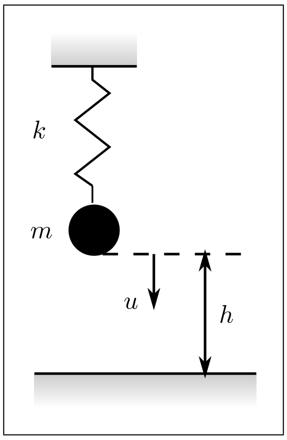

Figure 2.27.: A one dimensional mass-spring system, constrained by a rigid support. *Adapted from:* Wriggers (2002)

The restriction can be described as:

$$c(u) = h - u \geq 0 \tag{2.51}$$

Taking the reactive force f_R into account, either $c(u) > 0$ and $f_R = 0$ or $c(u) = 0$ and $f_R < 0$. Both cases can be expressed together as:

$$c(u) \geq 0, \quad f_R \leq 0 \quad \text{and} \quad f_R c(u) = 0 \tag{2.52}$$

Due to formula 2.51, the virtual displacement can only point in the upward direction, hence $\delta u \leq 0$. This leads to a variational inequality:

$$k \cdot u \cdot \delta u - m \cdot g \cdot \delta u \geq 0 \tag{2.53}$$

Since these variational inequalities do not allow for a direct solution of the contact problems, special methods, such as the Lagrange multiplier or penalty method, are needed. The Lagrange multiplier method assumes that $c(u) = 0$, which means that the constraint is active. Subsequently, the constraint $c(u)$ is multiplied by the Lagrange multiplier λ and added to the total energy:

$$\delta\Pi(u) = k \cdot u \cdot \delta u - m \cdot g \cdot \delta u + \lambda c(u) \tag{2.54}$$

Comparison with formula 2.52 yields that the Lagrange multiplier is equivalent to the reaction force f_R. Independent variation of δu and $\delta\lambda$ shows that formula 2.51 is satisfied and f_R can be calculated in case of contact ($u = h$):

$$f_R = \lambda = k \cdot h - m \cdot g \tag{2.55}$$

The penalty method also adds a term to the energy equation:

$$\delta\Pi(u) = k \cdot u \cdot \delta u - m \cdot g \cdot \delta u + \frac{1}{2}\epsilon[c(u)]^2 \tag{2.56}$$

Where the penalty parameter ϵ can be interpreted as a spring stiffness. Variation, solving for u and substituting in formula 2.51 finally leads to the reaction force:

$$f_R = \frac{\epsilon}{k+\epsilon}(k \cdot h - m \cdot g) \tag{2.57}$$

Hence, for $\epsilon \rightarrow \infty$ formula 2.57 delivers the same solution as the Lagrange multiplier method. $\epsilon \rightarrow 0$ represents the unconstrained solution in inactive contact, and causes high penetration in active contact. A figurative comparison of Lagrange multiplier method and penalty method is depicted in figure 2.28. (Wriggers 2002)

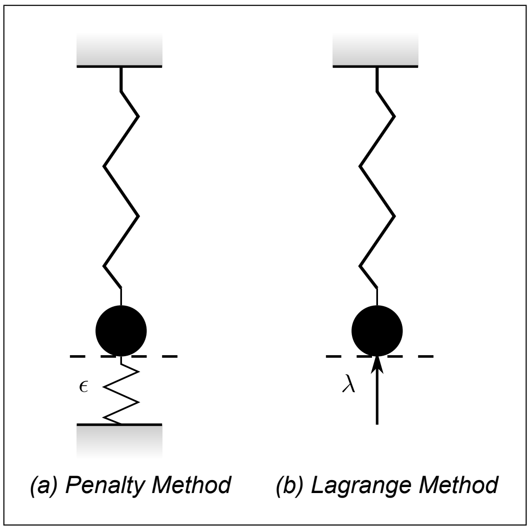

(a) Penalty Method (b) Lagrange Method

Figure 2.28.: Comparison of the penalty and Lagrange multiplier method for modelling contact in FEA. *Adapted from:* Wriggers (2002)

Both Lagrange multiplier and penalty method produce a force at all nodes in contact, in order to avoid them from penetrating. These forces subsequently cause a displacement, similar to any other external force applied on the body.

2.3.4. Application of FEA and MBS to Biomechanical Problems

In this section, the applicability of FEA and MBS to biomechanical problems is investigated based on literature. The biomechanical problem, in this thesis, is the development of a kinematic model of a human joint. In literature, such models are developed in order to investigate free movement (Sancho-Bru et al. 2001), joint stability (Crowninshield and Johnson 1976, Peña et al. 2006) or to predict muscle forces (Brook et al. 1995). Results of these simulations are intended to be used mainly in medical fields, such as hand surgery.

Challenges in developing a plausible biomechanical model are of two different kinds: Challenges concerning the material and those concerning the geometry of the joint. As it has already been mentioned, mechanical properties of living tissues are very hard to determine. Living tissues are mostly inhomogeneous (e.g. cartilage), anisotropic (e.g. collagen fibres of the ligaments), nonlinear (e.g. stress-strain curve), show time dependent behaviour (e.g. viscoelasticity) and some of them also biphasic behaviour (e.g. solid and liquid phase of cartilage). Even if all of these properties could be determined for a certain specimen, they would still only be valid for the tested specimen. This leads to the problem of individual geometry. Not only material properties,

but also joint surfaces, length of bones and areas of tendon or ligament insertions depend on the investigated individual. It is obvious that also the applicability of assumed, general joint axes is limited.
As a result, an appropriate level of detail for a biomechanical simulation has to be considered, according to its aim. In literature, both FEA and MBS are used for the simulations of human joints, serving different purposes. Several of these simulations are explained briefly in the following. In a concluding remark, MBS and FEA are compared to each other in order to determine the most sensible approach for simulating the kinematics of a human finger joint.

FEA

FEA is applied whenever internal stresses or displacements need to be calculated accurately. Articular cartilage is, for instance, analyzed regarding the internal stress distribution (Guo et al. 2009), as well as the wear of implants, replacing the cartilage (Goreham-Voss et al. 2010). Especially the calculation of wear is a well investigated topic. Goreham-Voss et al. (2010) gives an overview of those simulations, some of them also accounting for viscoelastic effects. Other applications of FEA aim solely at modelling single tissues, such as ligaments. A very detailled model accounting for hyperelasticity, anisotropy and viscoelasticity is proposed by Peña et al. (2007).
This clearly shows the strength of FEA: The level of detail. However, the main disadvantage is the high computational cost (Hippmann 2004, Lin et al. 2010). As soon as different tissues are involved in a simulation, simplifications are necessary. Guo et al. (2009) and Peña et al. (2006), for instance, consider both cartilage and ligaments, but assume the cartilage to be isotropic, homogeneous and linearly elastic. Another disadvantage is that all bodies involved in the FEA have to be constrained, either by locking degrees of freedom, or by assuming axes of motion (Guo et al. 2009).

MBS

Compared to FEA, the biggest advantage of MBS is, clearly, computational speed. Many biomechanical models in MBS aim primarily at developing fast contact algorithms (Landon et al. 2009, Bei and Fregly 2004, Lin et al. 2010). Most of the contact models are based on the theory of elastic foundation. In some models, the contact is assumed to be linear, which, according to Blankevoort et al. (1991), serves as an appropriate simplification. However, not all simulations make use of these contact algorithms. Some of them assume the bones to be rigid and linked by rotational axes of, hence, develop classical multi body systems (Wu et al. 2009). Additionally, many analytical models exist (Brook et al. 1995, Valero-Cuevas et al. 2003, Sancho-Bru et al. 2001, Giurintano et al. 1995, Crowninshield and Johnson 1976). In these approaches, simplified multi body systems are established based on fixed rotational axis, which are solved analytically rather than by numerical approximation.
Another advantage resulting from the low computational requirements is that not only one joint, but whole kinematic chains, such as a finger, can be simulated. Despite the advantage of computational speed and simplicity, there are some drawbacks. Muscles, tendons and ligaments are typically modelled as springs or spring-damper combinations and assumed to exert forces from one point to another. This means, neither geometry of the tissue itself nor the area of insertion is considered. Good approximation is achieved according to Wu et al. (2009) if muscles with large insertion areas modelled as two point-to-point elements. The simplification of the contact using the theory of elastic foundation could be mentioned as another disadvantage of MBS. However,

it is shown that these contact models are able to predict contact forces comparable to those of FEA (Li et al. 1997).

Conclusion

The literature investigation showed that FEA is useful whenever the joint kinematics is known beforehand, and internal distribution of stress or displacement has to be calculated. MBS in combination with elastic foundation contact models delivers a computationally fast approximation of contact forces, assuming many simplifications.
It is obvious that FEA is the more powerful and diverse tool for any simulation. However, the aim of the thesis is to determine the joint kinematics rather than the internal stresses or deformations of the tissues involved. Furthermore, there is a lack of material data in the field of biomechanics. Even though there are formulations of ligaments, tendons, muscles and cartilage considering all effects of living tissues, experimentally validated material parameter are missing as of this writing. Taking into account the limited availability of material data and computational restrictions, MBS seems to serve as a sensible means of simulating human joint movement. In such a simulation, articular surfaces, muscles and ligaments can be accounted for using force elements with force laws as described in section 2.3.2.

3. Method

The investigation in the field of anatomy, biomechanics and contact mechanics shows that several tissues have to be involved in any biomechanical model for simulating human joint kinematics. Descriptions of the mechanical behaviour of these tissues are provided by biomechanical studies. Existing contact models in either MBS or FEA allow to account for the actual shape of articulating surfaces. Comparing the methods of computational contact mechanics, it is concluded that MBS in combination with PCM delivers a sensible means for conducting kinematic investigations (see section 2.3.4).

In this chapter, a method is proposed to conduct kinematic simulations of human joints based on contacting surfaces, stabilizing muscles and motion restricting ligaments. For this purpose, the CMC joint of the thumb is modelled in commercial MBS software SIMPACK using PCM. The movement of the joint is simulated in time domain and controlled by muscle activation.

In the following section, the outline of the model of the CMC joint is explained briefly. Subsequent sections elucidate the process of modelling each tissue involved in the model in detail, regarding both their geometry and mechanical properties. The assembly of all modelled components in SIMPACK yields the biomechanical model of the CMC joint. The principles behind the simulations conducted based on this model are elucidated in the final section of this chapter.

3.1. Outline of the Simulation

The simulation of the joint kinematics requires a detailled biomechanical model of the CMC joint. Before a simulation in any MBS software can be conducted, the components involved in this model have to be defined. As it has been mentioned, that the level of detail is essential for any biomechanical model. The following points have to be considered:

- The tissues involved
- Geometrical aspects of the tissues
- Mechanical aspects of the tissues

For the purpose of kinematic investigations, bones, cartilage, muscles and ligaments have to be modelled. In the MBS, the bones are represented by rigid bodies. One of the bones is fixed, while the other one is unconstrained in three dimensional space, hence, possesses six DoF. Cartilage, muscles and ligaments exert forces on these bodies. As a result, they have to be modelled as force elements. In the specific case of the CMC Joint, the bones involved are the trapezium and the first metacarpal bone. Eight muscles are considered to contribute largely to joint movement: EPL, EPB, FPL, FPB, APL, AD, OP and APB. Joint stabilizing ligaments incorporated in the simulation are: dIML, pIML, UCL, DRL, sAOL, dAOL and POL.

All the tissues involved have to be defined regarding their geometry. For the bones and the cartilage, a polygonal surfaces have to be determined. Since the calculation of contact forces is based on these surfaces, their quality is essential. The surfaces are created based on magnetic resonance imaging (MRI) scans, which allow for in-vivo visualization of single tissues. The modelling of the geometry of ligaments and muscles is limited due to the principle of MBS. Each muscle and ligament is represented by one or more point-to-point force elements, depending on the size of the respective attachment area. Point-to-point elements only exert forces along the connection line between two attachment points. The elements are attached to the fixed bone on the one side, and to the unconstrained, moving bone on the other side.

In a MBS, movement is a result of forces and moments. Hence, force laws for each force element have to be formulated. The cartilage is modelled using a modified version PCM, which accounts for geometric nonlinearities. Muscles exert both active and passive forces. The passive force is determined by nonlinear spring characteristics, whereas calculation of the active force is based on the Hill model. Another nonlinear spring force element is defined to represent the ligaments.

A schematical drawing of the modelling approach is depicted in figure 3.1, including the body fixed coordinate systems of the trapezium (TZ) and first metacarpal bone (MC1), the muscle and ligament force elements (FE) and the articular surfaces used for contact force calculation.

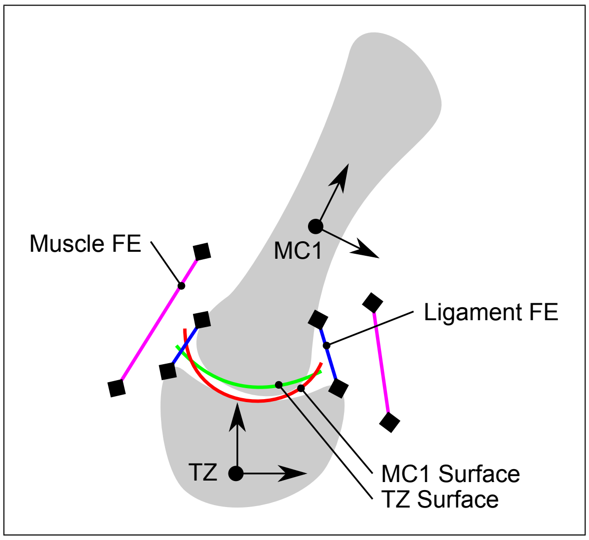

Figure 3.1.: A schematic depiction of the model of the CMC joint of the thumb

It is obvious that the joint is modelled in a simplified way. Hence, it is important to mention tissues and mechanical effects that are not considered. The surrounding tissue is generally neglected, even though it might be seen as a means of limiting joint motion. Muscles and ligaments are modelled as massless links defined by a proximal and distal attachment point, hence, hypomochlions do not cause a deflection of the line of action. Time dependent behaviour of the material is neglected, since necessary parameters are not available in literature as of this writing.

Considering this level of detail, the cartilage, muscles and ligaments are modelled regarding both the geometry and mechanical properties. The assembly of all these components in SIMPACK yields the biomechanical model of the CMC joint and allows for the simulation of the joint kinematics by activating single or multiple muscles.

3.2. Modelling Articular Cartilage

The articular cartilage is a soft tissue that covers the contact area of adjacent bones of a human joint. Modelling the articular cartilage holds two challenges: First, the articular surfaces have to be obtained from MRI images. This involves creating a polygonal surfaces, as well as several processing steps, such as smoothing and dilating. Second, the mechanical properties have to be accounted for. Since PCM is used to model the articular contact, the force law for computing contact forces has to be adapted.

Generally, the following method is proposed: The whole hand is scanned using MRI to obtain a 3D image in neutral position. The segmented bones of this image serve as a reference for the attachment points of ligaments and muscles. Due to limitations of MRI, it is not possible to identify the articular cartilage in this image. Hence, a detailled image of the CMC joint is taken. In this image, the cartilage thickness can be estimated. By dilating the bone surface extracted from the detail image with the measured thickness, the cartilage surface is obtained. In order to match the cartilage surfaces from the detailled image against the bones of the reference image, a transformation is found for each bone using a pose estimation technique. The resulting polygonal cartilage surfaces, transformed into the reference image coordinate system, are imported in SIMPACK and used by PCM to calculate the contact forces during the simulation.

The modelling process is subdivided into two steps: First, the geometry, i.e. the cartilage surface, has to be obtained. Second, a force element has to be established in SIMPACK, which calculates the forces resulting from cartilage contact.

3.2.1. Geometry

In the following sections, the creation of the polygonal surfaces is explained, starting from the segmentation of the MRI images. The principle behind MRI is explained in the first section, which is considered relevant for the process of manual segmentation. Subsequent to a general description of polygonal surfaces, a method for extracting surfaces from MRI image is presented. Since the quality of these surfaces requires improvement, both measures for the surface quality and further processing steps are elucidated. Finally, coordinate system are defined for each bone and the pose estimation algorithm for matching the surfaces of the detail image to those of the reference image is introduced.

Extracting Volumes from MRI Images

In order to work with the image derived by the MRI, it is useful to be aware of the process behind it. MRI is a 3D visualizing technique, mainly used in medical fields of application. The principle of MRI is to measure the reaction of hydrogen protons under exposure to a strong magnetic field. Different tissues are distinguishable due to different densities and reactions of these protons within the tissue. A detailled explanation of the functionality of MRI is provided by Weishaupt et al. (2009).

Each proton has an angular and magnetic momentum due to its spin. The magnetic momentum is influenced by magnetic fields and induces voltage in a coil. If the magnetic field is changed, the spinning axis gradually aligns to its direction, which causes a precession movement. This precession movement has a certain frequency which is proportional to the strength of the magnetic field, called the Larmor frequency. If all spins are aligned to the magnetic field, longitudinal magnetization is high. As soon as the system is stable, it gets excited by applying a radio frequency equal to the Lamor frequency. Subsequently, the spin is tilted 90 degrees. This movement induces alternating

Tissue	in T1 weighted image	in T2 weighted image
Fat	Bright	Bright
Hydrous fluid	Dark	Bright
Muscle	Dark	Dark
Connective Tissue	Dark	Dark
Hyalin cartilage	Bright	Bright
Corticalis	Dark	Dark

Table 3.1.: Appearance of different tissues in MRI-images

voltage in a coil, similar to a dynamo. The frequency of the induced voltage is equal to the Larmor frequency. This signal is called the MR-signal.

Due to different effects, the MR-signal ceases with time. First, the spin realigns to the direction of the magnetic field. The time a proton needs to reach this state again is called the T1 relaxation time. Second, the spins in the tilted plane change their phase. After the so called T2 relaxation time, this dephasing causes the spin vectors to sum up to zero. As a result, the MR-Signal is lost. Different tissues have different T1 and T2 values.

In order to obtain either T1 or T2 weighted images, different sequences of excitation have to be chosen. In T1 weighted images, tissues with small T1 appear bright and those with large T2 dark. This is achieved by repeated excitation with intervals of repetition time TR. If TR is chosen to be large, protons of all tissues will already be realigned when the measurement is conducted. If TR is small, the signal difference between small and large T1 relaxation time of tissue is measurable. T2 is generally smaller than T1. In order to measure tissues with difference in T2, the time between excitation and measurement, the echo time TE, can be adapted. Large TE gives a good contrast of tissues with different T2 relaxation times, whereas small TE gives maximal signal for all tissues. In T2 weighted images, tissues with small T2 appear dark, and those with large T2 appear bright, respectively. Signal intensities of different tissues in T1 and T2 weighted images are displayed in table 3.1.

Additionally, proton density weighted images can be taken. These images display the density of the protons in a tissue and give maximum signal strength. This is achieved by setting TR to a large and TE to a small value. This method is valuable to get signal from tissues which induce only a small signal, such as ligaments.

In order to locate the position of the measured signal, the magnetic field has to be encoded. This is achieved by gradient coils for each direction, which cause an inhomogeneity of the magnetic field. Since the excitation frequency is dependent on the strength of the magnetic field, signals of single slices perpendicular to the respective direction can be measured. This technique is used for longitudinal position encoding. The measurement of the slice is, however, the sum of all signals. Decomposition of the frequencies is conducted by applying a Fourier transform, which delivers all frequencies contained in the signal. Repeating the measurement several times for a single slice and subsequent two dimensional Fourier transform yields an image of signal intensities at their respective spatial positions.

Additional techniques are used, for instance to reduce capturing time, increase of the signal to noise ratio or to suppress the signal of certain tissues. However, the basic knowledge described

above is considered sufficient for working with the images taken with MRI.
The MRI images used for extracting the bone and cartilage surfaces are taken from a male healthy subject by Marcus Settles at Klinikum Rechts der Isar. A Philips Achieva MRI device with a magnetic field strength of $1.5\,\mathrm{T}$ is used with a Philips Sense Cardiac and Micro-47 receiving coil for the reference and the detail image, respectively. Both images are T1-weighted.

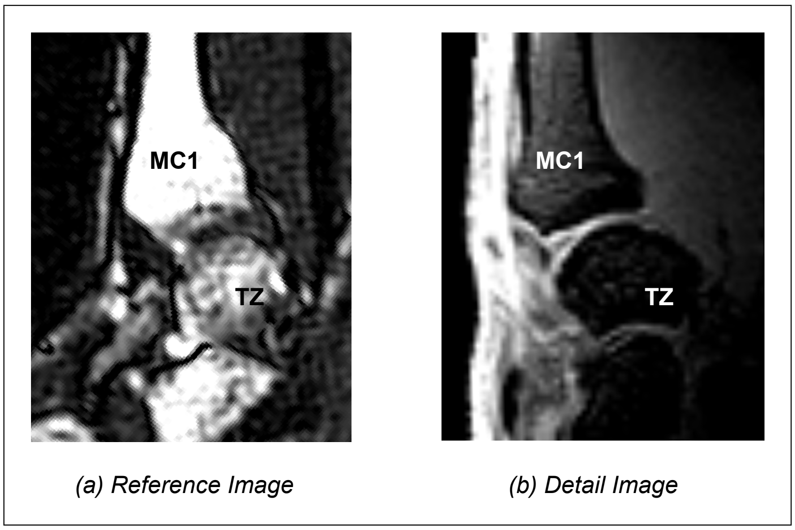

(a) Reference Image

(b) Detail Image

Figure 3.2.: Comparison of an MRI slice of the CMC joint in the reference and the detailled image

In the reference image, the corticalis appears dark, whereas fat and water appear bright. In order to identify cartilage, the fat is suppressed in the detailled image. Resolutions are $0.34 \times 0.38 \times 0.34\,\mathrm{mm}$ for the reference and $0.99 \times 0.52 \times 0.52\,\mathrm{mm}$ for the detailled image. The high resolution of the reference image is achieved only by interpolation. As it can be seen in figure 3.2, the resolution is not necessarily a measure for image quality. The contour of the cartilage can be identified in figure 3.2 (b), whereas it is hardly visible in figure 3.2 (a).

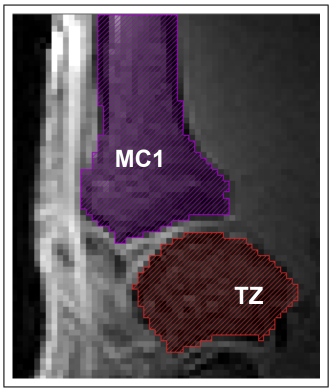

Figure 3.3.: Selected voxels in a single slice of an MRI image during manual segmentation

The MRI image is typically visualized in slices, as depicted in figure 3.2. The whole image, however, consists of volumetric pixels, so called voxels, each of which contain a value representing the signal intensity. In order to display single tissues, such as bone or cartilage, single voxels have to be assigned to this tissue. Selecting these voxels is called segmentation and can be performed either manually or automatically. Since the corticalis is hard to distinguish from other tissues near the bone, such as tendons, segmentation is conducted manually. Figure 3.3 shows the selected area of a single slice. This procedure is repeated for all transversal, sagittal and frontal slices. For the simulation of the CMC joint, the bone volume of the trapezium, the first, the second and the third metacarpal are segmented from the reference image. In the detail image, the visible part of the first metacarpal bone and the trapezium are segmented.

Creating Polygonal Surfaces based on volumetric Data

In this section, the process of creating a polygonal surfaces from MRI images is explained. The notation of polygonal surfaces is adopted from (Zhang and Hamza 2006) and introduced briefly in the following. Polygonal surfaces consist of a set $\mathcal{V}$ of n vertices $\mathbf{v}_i$:

$$\mathcal{V} = \{\mathbf{v}_1, \ldots, \mathbf{v}_i, \ldots, \mathbf{v}_n\} \tag{3.1}$$

and a set $\mathcal{T}$ of m faces $\mathbf{t}_j$:

$$\mathcal{T} = \{\mathbf{t}_1, \ldots, \mathbf{t}_j, \ldots, \mathbf{t}_m\} \tag{3.2}$$

Vertices are points in 3D space defined by their Cartesian coordinates. Each face $\mathbf{t}_j$ is defined by a list of vertex indices. If the face is triangular, the list contains three vertex indices. The order of the list determines the direction of the face normal $\mathbf{n}(\mathbf{t}_j)$, which is calculated as follows:

$$\mathbf{n}(\mathbf{t}_j) = \frac{((\mathbf{v}_2(\mathbf{t}_j) - \mathbf{v}_1(\mathbf{t}_j)) \times (\mathbf{v}_3(\mathbf{t}_j) - \mathbf{v}_1(\mathbf{t}_j))}{||((\mathbf{v}_2(\mathbf{t}_j) - \mathbf{v}_1(\mathbf{t}_j)) \times (\mathbf{v}_3(\mathbf{t}_j) - \mathbf{v}_1(\mathbf{t}_j))||} \tag{3.3}$$

Vertices $\mathbf{v}_j$ adjacent to $\mathbf{v}_i$ form the neighborhood $\mathbf{v}_i^*$. The cardinality of $\mathbf{v}_i^*$ is called the degree d_i of $\mathbf{v}_i$. The set of triangles containing $\mathbf{v}_i$ is denoted as $\mathcal{T}(\mathbf{v}_i^*)$. Averaging the normals of $\mathbf{t}_j \in \mathcal{T}(\mathbf{v}_i^*)$ yields the vertex normal $\mathbf{n}_i$:

$$\mathbf{n}_i = \frac{1}{d_i} \sum_{\mathbf{t}_j \in \mathcal{T}(\mathbf{v}_i^*)} \mathbf{n}(\mathbf{t_j}) \tag{3.4}$$

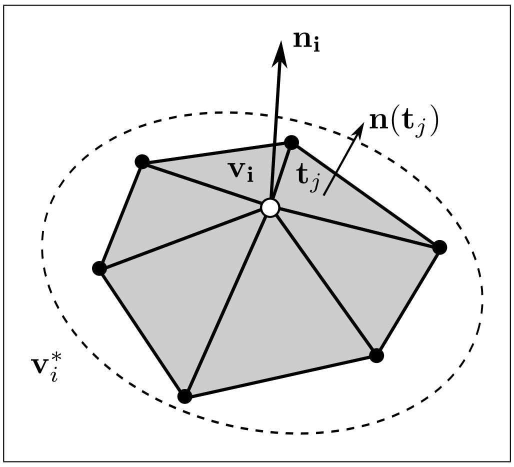

Figure 3.4.: Neighborhood of $\mathbf{v_i}$, faces $\mathbf{t_j}$, face normal $\mathbf{n}(\mathbf{t_j})$ and vertex normal $\mathbf{n_i}$

Figure 3.4 depicts vertices and faces, including the vertex and face normals, respectively. In order to represent the bones and cartilage surfaces in the model, it is necessary to define polygonal surfaces based on the MRI images. The voxels selected in the segmentation process yield a volumetric scalar field of integer numbers. Voxels that are considered to be inside the material are denoted with values greater than zero, those considered to be outside are denoted with zero. In medical imaging, volumetric scalar fields are typically displayed by isosurfaces (Livnat et al. 2000). The isosurface displays a surface of constant values in the volume, separating lower and higher valued regions. For the extraction of the surface, the marching cubes algorithm established as a simple and efficient standard method (Verdonck 2009). It reduces the problem of the surface creation to the analysis of 15 local voxel configurations in a binary dataset. In general, the voxels are represented as points in a 3D grid with a respective gray value $I(x, y, z)$. In order to determine which voxels belong to the material, a threshold value g_t is chosen. The binary grid is thus defined as:

$$\mathcal{B} = \begin{cases} 1 & \text{for } I(x,y,z) > g_t \\ 0 & \text{for } I(x,y,z) \leq g_t \end{cases} \tag{3.5}$$

The creation of the surfaces is conducted locally for a set of eight neighboring voxels of the grid. Four voxels are selected from each of the two adjoining slices forming a cuboid, as depicted in figure 3.5 (a). In this cuboid, there are $2^8 = 256$ possible binary configurations. Using symmetry properties, the number of configurations can be reduced to 15. One of them is shown as an example in figure 3.5 (b).

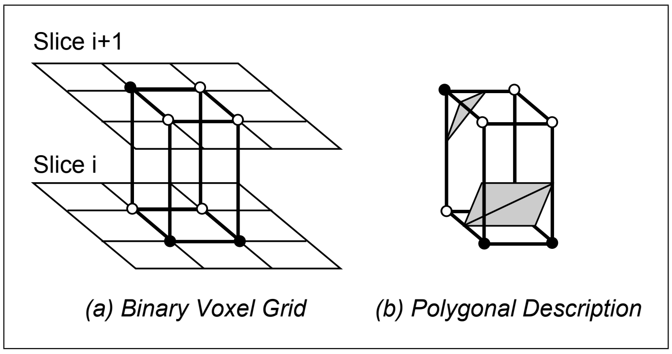

(a) Binary Voxel Grid (b) Polygonal Description

Figure 3.5.: Binary voxel grid and the respective polygonal description of the marching cubes algorithm. *Adapted from:* Handels (2009)

For each configuration, a polygonal description of the surfaces contained in the cuboid is generated. Voxel configurations and respective polygonal descriptions are represented in a lookup table. Using this table, the marching cube algorithm finds suitable descriptions for each cuboid of the whole volumetric dataset. The surfaces intersect the edges of adjacent voxels in the cuboid at a certain point. In order to determine the vertex of the triangular surface, these intersection points are linearly interpolated. (Handels 2009)

In case the isosurface is used for visualizing segmented volumetric data, the value for each voxel of the grid represents the tissue it belongs to. If all voxels within the segmented tissues are assigned the value 1, the threshold value $g_t = 0.5$ generates a surface in between the voxels of the tissue and adjacent, zero valued voxels. Figure 3.6 shows the isosurface of the first metacarpal bone of the detail image.

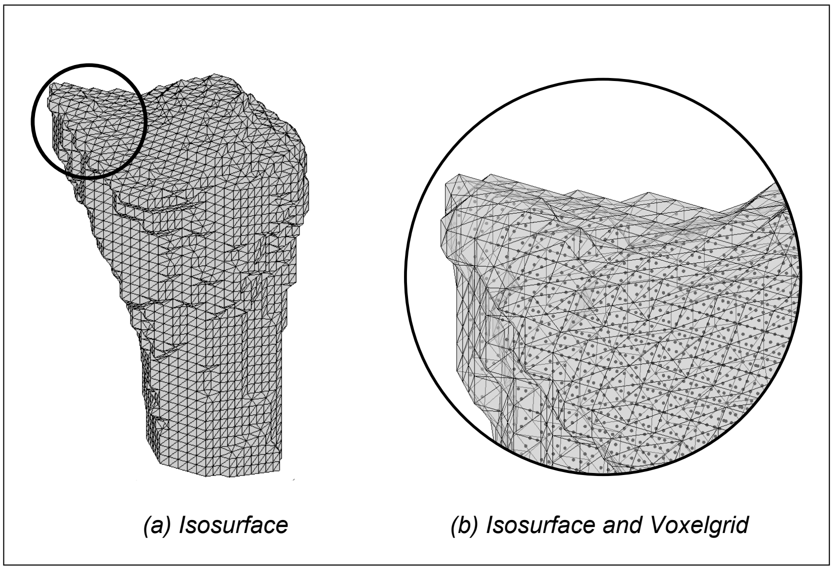
(a) Isosurface (b) Isosurface and Voxelgrid

Figure 3.6.: Isosurface of the first metacarpal bone of the detail image

Since the marching cubes algorithm accounts for any voxel with value above g_t, it is prone to noise. Furthermore, the resulting surface lacks the required smoothness to conduct a contact analysis. Improvement can be achieved by preliminary smoothing of the volumetric dataset. Similar to 2D image processing, linear filters can be applied (Handels 2009). For each voxel of the image $I(x,y,z)$, a new value is calculated depending on the values contained in a mask M of size $(2m+1)\times(2m+1)\times(2m+1)$. The filtered image $\widetilde{I}$ is computed as follows:

$$\widetilde{I}(x,y,z) = \sum_{k=-m}^{m}\sum_{j=-m}^{m}\sum_{i=-m}^{m} I(x+i,y+j,z+k)M(i,j,k) \tag{3.6}$$

Mean filtering, also referred to as box filtering, can be applied by defining M as:

$$M(i,j,k) = \frac{1}{n^3} \tag{3.7}$$

Gaussian filtering is achieved by defining M as:

$$M(i,j,k) = \frac{1}{(2\pi\sigma)^3}e^{-\frac{i^2+j^2+k^2}{2\sigma^2}} \tag{3.8}$$

The standard deviation σ serves as a filtering parameter. The isosurfaces of the first metacarpal of the detail image after the application of the filters with size $3\times3\times3$ are displayed in figure 3.7. For further processing, the volumes segmented from the detail images are filtered with a $3\times3\times3$, those of the reference image with a $7\times7\times7$ box filter. However, smoothness still needs to be improved. Furthermore, accuracy of the isosurface with respect to the originally segmented data might be lost. This is partly caused by the process of smoothing itself, but also by the choice of the threshold value g_t. This value has minor influence in the original volumetric dataset but affects the surface extraction from the filtered dataset, since $I:\mathbb{N}^3\rightarrow\mathbb{N}$, whereas $\widetilde{I}:\mathbb{N}^3\rightarrow\mathbb{R}$. The effect of g_t after volume smoothing is depicted in figure 3.8.

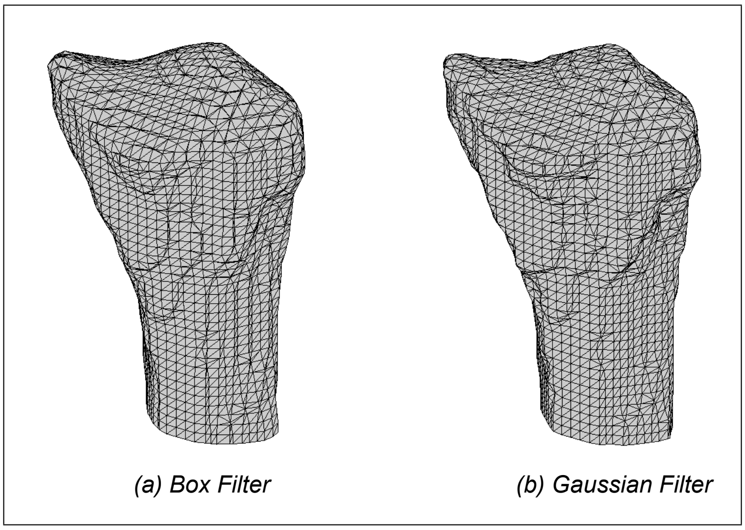

(a) Box Filter *(b) Gaussian Filter*

Figure 3.7.: Isosurfaces after applying filters to the volumetric data

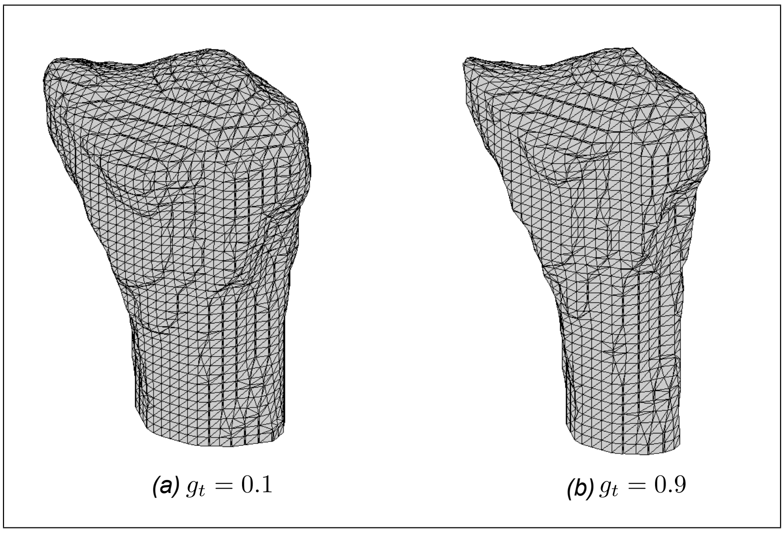

(a) $g_t = 0.1$ *(b)* $g_t = 0.9$

Figure 3.8.: Influence of g_t on the isosurfaces of filtered volumes

In order to deal with these problems, further steps of surface processing are conducted. Quality measures are introduced in the following section and serve as a means of comparison to the original surface.

Measuring the Surface Quality

Several techniques can be applied to improve the quality of a triangular surface. However, it is necessary to define measures to be able to compare their effectiveness. Typical measures for triangular meshes, such as edge ratio and triangle area, are elucidated in the following. Additionally, methods for estimating the accuracy and the smoothness of the surface are introduced.
The calculations of PCM are based on individual triangles, accessing their areas and centroids. In order to achieve consistent results, the shape of the triangles should remain equal over the whole surface. The shape can be measured by computing the area and the edge ratio of each triangle $\mathbf{t}_j$. The edge ratio is defined as the ratio of the shortest edge e_{min} to the longest edge e_{max} of the triangle (Har-Peled 2011):

$$a_j = \frac{e_{min,j}}{e_{max,j}} \tag{3.9}$$

The area A_j of each triangle is calculated using the cross product:

$$A_j = \frac{1}{2}||(\mathbf{v_2}(\mathbf{t_j}) - \mathbf{v_1}(\mathbf{t_j})) \times (\mathbf{v_3}(\mathbf{t_j}) - \mathbf{v_1}(\mathbf{t_j}))|| \tag{3.10}$$

As it has already been mentioned, volume smoothing may cause inaccuracies. In order to calculate the resulting error, the offset of the surface with respect to the the voxels on the boundary of the volume is estimated. Boundary voxels are determined based on their distances from the x-y, x-z and y-z plane of the image coordinate system. For each point of the grid of one of the planes, only the voxels with minimal and maximal distance are kept. In the following, each boundary voxel is denoted as a point $\mathbf{p} \in \mathcal{P}$ in 3D space. The error of the surface is defined as the mean of the distances between each $p \in \mathcal{P}$ and the nearest vertex $\mathbf{v}_p$ along the respective vertex normal $\mathbf{n_p}$. Searching for the minimal euclidean distance between a voxel and all vertices yields $\mathbf{v}_p$. The distance D_i of each voxel $\mathbf{p}_i$ is subsequently calculated as follows:

$$D_i = (\mathbf{v}_p - \mathbf{p}_i) \cdot \mathbf{n_p} \tag{3.11}$$

Summation of $|D_i|$ over $\mathcal{P}$ delivers the measure of the accuracy E with respect to the segmented volume:

$$E = \sum_{\mathcal{P}} |D_i| \tag{3.12}$$

In order to estimate the smoothness of a polygonal surface, the curvature of paraboloids fitted to each vertex neighborhood $\mathbf{v}_i^*$ are calculated and averaged (Magid et al. 2007). The paraboloids are defined as second order surfaces with four parameters p_a,p_b,p_c and p_d:

$$z = p_a \cdot x^2 + p_b \cdot x \cdot y + p_c \cdot y^2 + p_d \tag{3.13}$$

Rewriting in matrix form yields:

$$z = \begin{bmatrix} x^2 & x \cdot y & y^2 & 1 \end{bmatrix} \begin{bmatrix} p_a & p_b & p_c & p_d \end{bmatrix}^T \tag{3.14}$$

If the degree of the respective vertex is greater than four, the system is overdetermined. A solution is found using the least-squares method (Eberly 2008):

$$\begin{bmatrix} p_a \\ p_b \\ p_c \\ p_d \end{bmatrix} = pinv\left(\begin{bmatrix} x_1^2 & x_1 \cdot y_1 & y_1^2 & 1 \\ \vdots & \vdots & \vdots & \vdots \end{bmatrix}\right)\begin{bmatrix} z_1 \\ \vdots \end{bmatrix} \tag{3.15}$$

The expression $pinv(\mathbf{A})$ denotes the pseudo inverse and is defined as $\left(\mathbf{A}^T\mathbf{A}\right)^{-1}\mathbf{A}^T$. Formula 3.15 requires the vertex coordinates x_j, y_j and z_j of $\mathbf{v}_j \in \mathbf{v}_i^*$ to be transformed into a vertex specific coordinate system C_i. The z-axis of this coordinate system coincides with $\mathbf{n}_i$, the x-axis is an arbitrary unit vector perpendicular to z, and y is the result of $z \times x$. In order to transform the vertices from the reference image coordiante system C_I into C_i, the transformation matrix ${}^i\mathbf{T}_I$ needs to be computed. It is obtained using the unit vectors $\mathbf{c}_{x,i}$, $\mathbf{c}_{y,i}$ and $\mathbf{c}_{z,i}$ and the coordinates of $\mathbf{v}_i$ as follows:

$${}^i\mathbf{T}_I = \begin{bmatrix} \mathbf{c}_{x,i} & \mathbf{c}_{y,i} & \mathbf{c}_{y,i} & \mathbf{v}_i \\ 0 & 0 & 0 & 1 \end{bmatrix}^{-1} \tag{3.16}$$

The transformation matrix ${}^i\mathbf{T}_I$ transforms any vertex ${}^I\mathbf{v}_j$ defined in C_I into the vertex local coordinate system C_i:

$${}^i\mathbf{v}_j = {}^i\mathbf{T}_I{}^I\mathbf{v}_j \tag{3.17}$$

The coordinate system of an arbitrarily chosen vertex is shown in figure 3.9 (a). The corresponding paraboloid after least-squares fitting is depicted in figure 3.9 (b).

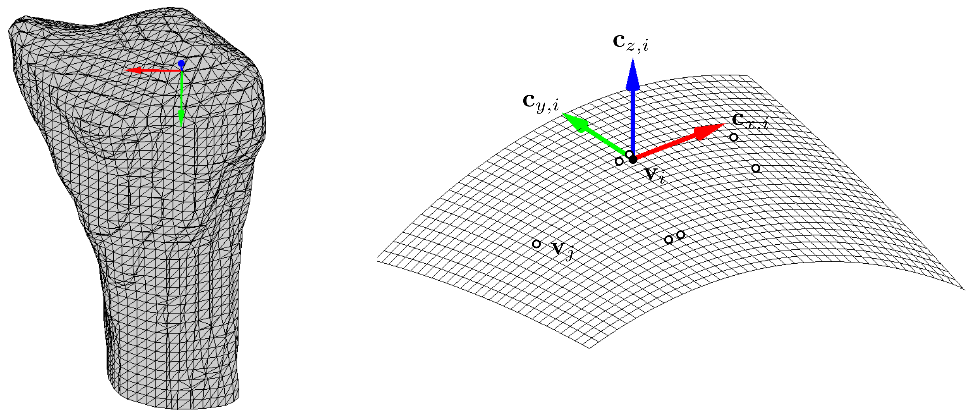

(a) Vertex Coordinate System

(b) Fitted Paraboloid

Figure 3.9.: A vertex coordinate system and the corresponding paraboloid, fitted to the immediate vertex neighborhood

The mean curvature H of the paraboloid is calculated as follows (Magid et al. 2007):

$$H = p_a + p_c \tag{3.18}$$

The mean of $|H_i|$ of all vertices $\mathbf{v}_i$ serves as a measure for the overall smoothness of the surface. Using a color map, accuracy and smoothness can be visualized by interpolating distance and curvature values between the vertices. Since the curvatures may vary at a large scale, a logarithmic scale is applied for the smoothness. The accuracy is displayed by averaging the voxel distances of each vertex.

Processing the Surfaces

In this section, methods for correcting and smoothing the surface are introduced. The quality measures established in the previous section allow for quantitative comparison of the obtained results. Finally, the bone surfaces extracted from the detail image are dilated by the cartilage thickness to represent the articulating surfaces.

Before further processing steps are conducted, the surfaces are scaled in order to account for the different, anisotropic resolutions of the MRI images. The scaling factors s_x, s_y and s_z are assumed to be equivalent to the voxel size. Hence, each vertex is transformed as follows:

$$\mathbf{v}_i \leftarrow \begin{bmatrix} s_x & 0 & 0 \\ 0 & s_y & 0 \\ 0 & 0 & s_z \end{bmatrix} \mathbf{v}_i \tag{3.19}$$

The correction algorithm is based on the voxel-vertex distance D. If one vertex serves as a reference for the distance calculation of several voxels, the distances are averaged for each vertex $\mathbf{v}_i$ and denoted by $\bar{D}_i$. Dilation of each vertex $\mathbf{v}_i$ along the vertex normal $\mathbf{n}_i$ compensates for errors caused by volume smoothing. However, this method produces very rough surfaces, as depicted in figure 3.10 (a). Improvement is achieved by incorporating the distances of all vertices in the neighborhood of $\mathbf{v}_i$. This step is similar to mean filtering of the distances of $\mathbf{v}_i^*$. The resulting distance is denoted as $\widetilde{D}_i$ and calculated as follows:

$$\widetilde{D}_i = \frac{1}{d_i} \sum_{\mathbf{v}_j \in \mathbf{v}_i^*} \bar{D}_j \tag{3.20}$$

Figure 3.10 depicts the original and corrected surfaces of the first metacarpal bone, extracted from the detail image. Dilation along the vertex normals using $\widetilde{D}_i$ delivers a smoother result, as shown in figure 3.10 (c). The original and corrected surface are displayed in figure 3.10 (a) and figure 3.10 (b) respectively. The error is visualized using color maps. The mean values and standard deviations (SD) of the error of the surfaces are provided in table 3.2.

It is shown that the correction algorithm is capable of reducing the error caused by volume smoothing. Using $\widetilde{D}_i$ yields a compromise between accuracy and smoothness. However, the shape of the triangles is still inconsistent over the surface. A smoother and more regular surface is obtained by applying Laplacian smoothing. Laplacian smoothing updates the coordinates of each vertex $\mathbf{v_i}$ as follows (Zhang and Hamza 2006):

$$\mathbf{v}_i \leftarrow \mathbf{v}_i + \sum_{\mathbf{v}_j \in \mathbf{v}_i^*} \frac{\mathbf{v}_j - \mathbf{v}_i}{d_i} \tag{3.21}$$

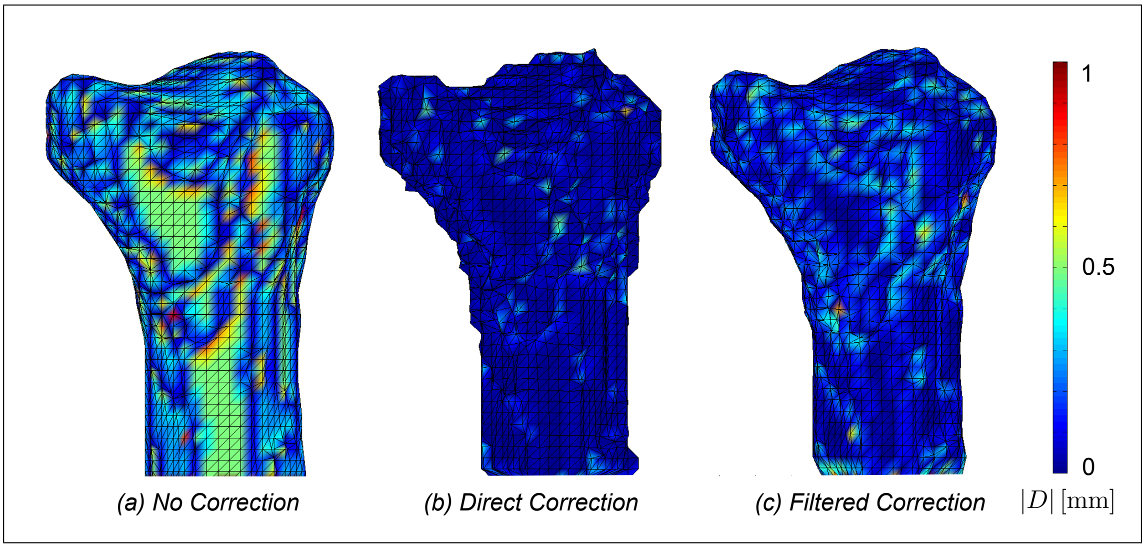

(a) No Correction (b) Direct Correction (c) Filtered Correction

Figure 3.10.: Comparison of the vertex errors of the original surface and the corrected surface using $\bar{D}_i$ and $\widetilde{D_i}$

	Distance Error $[\mathrm{mm}]$	
	Mean	SD
Original Surface	0.26	0.23
Correction with $\bar{D}_i$	0.05	0.072
Correction with $\widetilde{D_i}$	0.13	0.12

Table 3.2.: Mean errors and standard deviations before and after the application of the correction algorithm

Repeated application increases the smoothness, as depicted in figure 3.11, but shrinks the surface. As a result, the accuracy might decrease. Figure 3.11 (a), (b) and (c) show the surface without smoothing, after one iteration and after three iterations of smoothing. For visualization purposes, a logarithmic scale is applied. The results of iterative Laplacian smoothing regarding the triangle area, edge ratio and mean curvature are provided in table 3.3.

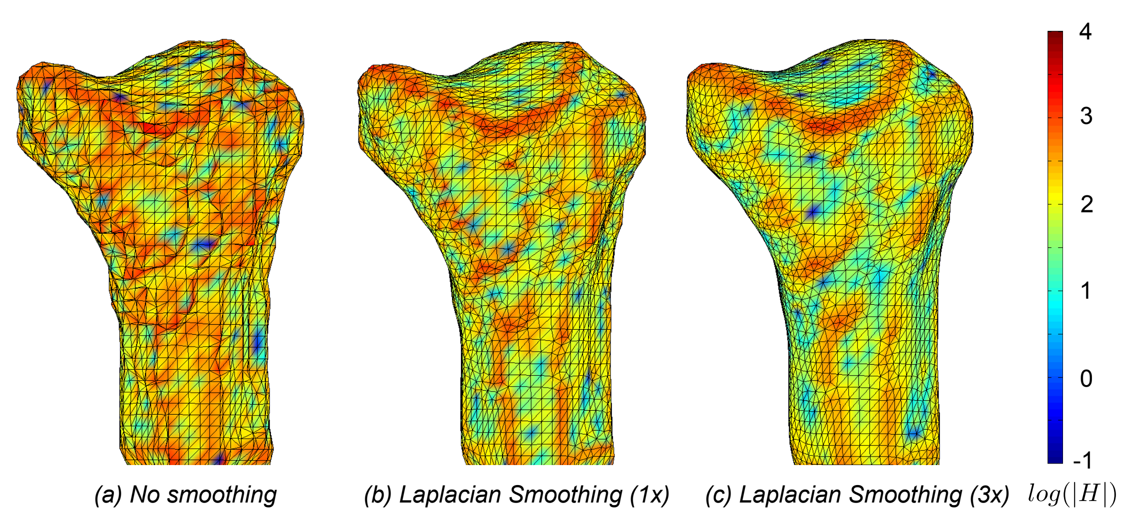

Figure 3.11.: Comparison of the surface smoothness without smoothing and after one and three iterations of Laplacian smoothing

	Triangle Area $[\mathrm{mm}^2]$		Edge Ratio $[-]$		Mean Curvature $[\mathrm{mm}^{-1}]$	
	Mean	SD	Mean	SD	Mean	SD
Corrected Surface	0.18	0.12	2.5	2.4	0.38	0.8
Smoothed (1x)	0.17	0.057	1.6	0.32	0.22	0.24
Smoothed (3x)	0.16	0.052	1.5	0.26	0.18	0.2

Table 3.3.: Surface quality before and after the application of Laplacian smoothing

Table 3.3 shows that even one iteration of Laplacian smoothing increases the quality of the surface significantly. Especially the consistency of the shape of the individual triangles is improved. Both correction and smoothing are applied for all surfaces extracted from the reference and detail image. All surfaces are corrected using $\widetilde{D}$. One iteration of smoothing is applied on surfaces extracted from the detail image, and three iterations on those of the reference image.

In order to obtain the cartilage surface, the surfaces of the first metacarpal and the trapezium of the detail image have to be dilated by the cartilage thickness. The cartilage thickness has to be estimated from the MRI image. Exact measurement is not feasible due to the resolution of the images. Qualitative comparison between the dilated cartilage surface and the original MRI data is achieved by displaying intersection polygons in the MRI slices. The intersection polygons are obtained by intersecting the surfaces by a plane coinciding with the respective MRI slice. They

are computed as follows: First, all intersected triangles are determined, i.e. triangles containing vertices separated by the plane. Second, the intersections of the plane with the connection lines between opposing vertices are calculated. The line between the vector-plane intersections yields a segment of the intersection polygon. The segments of all intersected triangles represent the whole contour of the plane-surface intersection. After scaling, this contour can be displayed in the MRI slice. The amount of dilation is subsequently manually adapted to best fit the cartilage identified in the MRI image. The surfaces are finally cropped by deleting all faces containing vertices within a defined spatial region.
Figure 3.12 (a) shows the first metacarpal and the trapezium bone of the detail image and the dilated surfaces representing the cartilage. The bone surfaces are displayed using Gouraud shading, which interpolates the colors of the surface depending on a light source (Bender and Brill 2006). The red and blue line show the result of the plane-surface intersection with the bone and cartilage surface, respectively.

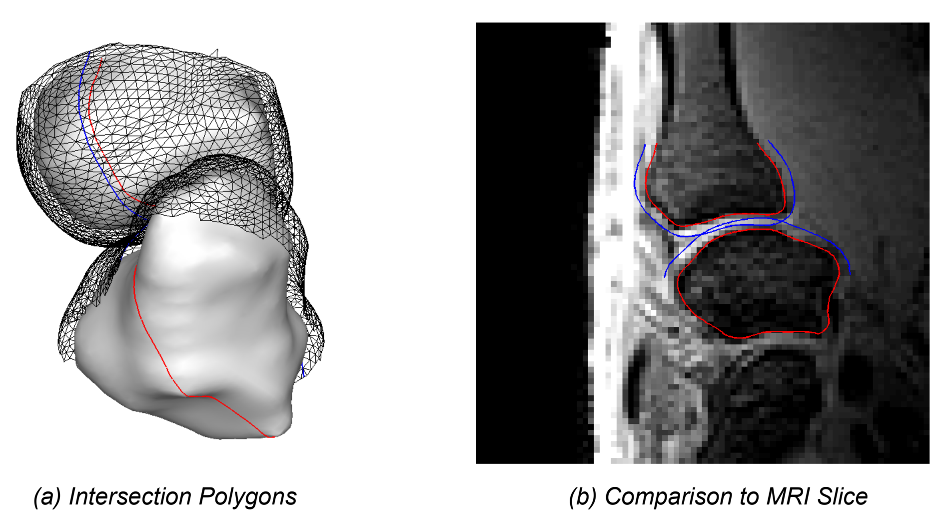
(a) Intersection Polygons

(b) Comparison to MRI Slice

Figure 3.12.: The intersection polygons of the bone (red) and the cartilage (blue) displayed with the surfaces and in the respective MRI slice

The cartilage surface of both the first metacarpal and the trapezium is obtained by dilation of $1.2\,\mathrm{mm}$ along the vertex normals and subsequent Laplacian smoothing.

Defining the Surface Coordinate Systems

In the MBS, each bone is represented as a rigid body with a body fixed coordinate system. Defining this coordinate system yields several problems, since the shape of the bone is irregular. The coordinate systems are either determined arbitrarily, or according to a proposed standard. The Standardization and Terminology Commitee of the International Society of Biomechanics (ISB) provides recommendations for the alignment of the local axes of articulated segments of each joint of the hand (Wu et al. 2005).
For metacarpal bones, the coordinate system is defined as follows: The origin is located midway between a connection line between the head and the base of the bone. The y-axis coincides with this line and points distally. The x-axis is aligned to the sagittal plane, which divides the bone into two symmetric parts. The z-axis is aligned perpendicular to both the x- and y-axis. For the

coordinate system of the trapezium, the following definition is proposed: The origin is placed on the mid-point of the central ridge. The y-axis points towards the junction of trapezium, scaphoid and trapezoid. The x-axis is perpendicular to the central ridge, pointing at the palmar elevation of the trapezium. The z-axis is aligned perpendicular to both the x- and y-axis and runs almost parallel to the central ridge.

Since the proposed definition of the metacarpal coordinate system uses symmetric planes, it may also serve as a good approximation of the center of mass and the principal axes of inertia. Hence, it is adopted for the use in the MBS. Aligning the axes of the coordinate system of the trapzium as recommended is less applicable, due to two reasons: First, in contrast to the metacarpal bone, the origin is defined on the articular surface of the bone, rather than in the center, which is different to the metacarpal coordinate system. Second, the definition of both the x- and y-axes involves the identification of a local feature of the bone and the junction of several bones, which is difficult due to limited resolution of the MRI images. As a result, the trapezium coordinate system is aligned as follows: The z-axis runs parallel to the central ridge. The x-axis runs perpendicular to the z-axis, pointing palmary and running parallel to the trapezial groove. The y-axis is aligned perpendicular to both the x- and z-axis and points distally. The origin is located in the plane dividing the central ridge into two symmetric parts, at the approximate center of rotation of the groove. The resulting coordinate system differs slightly from the ISB-recommendation. However, it allows a more distinct definition with respect to the available data. In the following, methods of determining the coordinate systems of the bones are presented.

The determination of the coordinate system of the metacarpal bone is based on principal component analysis of the vertices of the surface. This is a method often applied in the field of point cloud processing Belton (2008). The eigenvectors $\mathbf{e}_0$, $\mathbf{e}_1$ and $\mathbf{e}_2$ of the covariance matrix $Cov\left(\mathcal{V}\right)$ are calculated and form an orthogonal basis. The eigenvectors $\mathbf{e}_i$ represent the principal components, and their corresponding eigenvalues λ_i yield the variance in the respective direction. The origin $\mathbf{c}_0$ of the coordinate system is calculated as the mean of all vertices:

$$\mathbf{c}_0 = \frac{1}{n} \sum_{\mathbf{v}_i \in \mathcal{V}} \mathbf{v}_i \tag{3.22}$$

The total number of vertices is denoted as n. Using $\mathbf{c}_0$, the covariance matrix can be computed as follows:

$$Cov\left(\mathcal{V}\right) = \sum_{\mathbf{v}_i \in \mathcal{V}} \left(\mathbf{v}_i - \mathbf{c}_0\right) \left(\mathbf{v}_i - \mathbf{c}_0\right)^T \tag{3.23}$$

The eigenvalues λ_i and eigenvectors $\mathbf{e_i}$ are calculated by solving the equations (Bartsch 2007):

$$det\left(Cov\left(\mathcal{V}\right) - \lambda \mathbf{E}\right) = 0 \tag{3.24}$$

$$\left(Cov\left(\mathcal{V}\right) - \lambda_i \mathbf{E}\right) \mathbf{e}_i = \mathbf{0} \tag{3.25}$$

The eigenvalues are sorted descending regarding their eigenvalues, hence, $\lambda_0 > \lambda_1 > \lambda_2$. It is anticipated that the eigenvector with the largest eigenvalue coincides with the y-axis of the ISB-recommended coordinate system of the metacarpal bone. However, $\mathbf{e}_1$ and $\mathbf{e}_2$ do not necessarily correspond to the x- and z-axis. As a result, the axes have to be realigned. For the first and second metacarpal bone, the following definition delivers the desired alignment of the axes $\mathbf{c}_x$, $\mathbf{c}_y$ and $\mathbf{c}_z$:

$$\begin{aligned}\mathbf{c}_x &:= \mathbf{e}_3 \\ \mathbf{c}_y &:= \mathbf{e}_1 \\ \mathbf{c}_z &:= \mathbf{e}_2\end{aligned} \tag{3.26}$$

Figure 3.13 depicts the eigenvectors and the coordinate system of the first metacarpal bone as defined above. The coordinate system is computed using the corrected and smoothened surface extracted from the reference image.

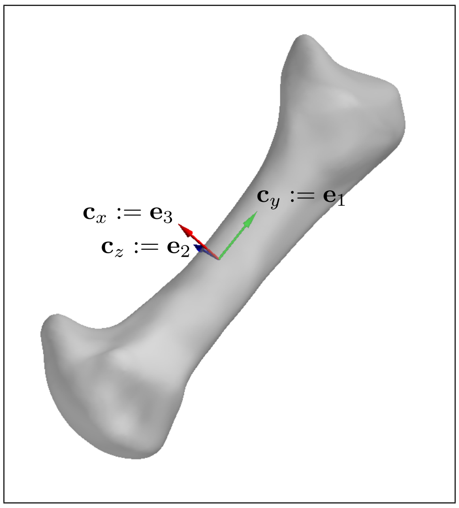

Figure 3.13.: Definition of the surface coordinate system of the first metacarpal bone based on principal component analysis

Applying the principal component analysis delivers good results for bones shaped like the metacarpal bone. However, it fails for bones with dimensions similar to each other, such as the trapezium. The result of the principal component analysis of the trpazium surface is shown in figure 3.14. In order to determine the coordinate system of the trapezium, the following steps are conducted: First, vertices that belong to the articular surface are selected manually. Second, a paraboloid is fitted to the set of selected vertices. Third, the coordinate system of the paraboloid is found by optimally aligning the vertices. Fourth, the coordinate system is shifted to the center of the circle resulting from the convex curvature at the origin of the paraboloid. Each step is elucidated in the following.

The vertices $\mathbf{v}_i$ that belong to the articular surface are selected manually and denoted as the subset $\mathcal{V}_S \subset \mathcal{V}$. The paraboloid is fitted to $\mathcal{V}_S$ using the least-squares method as described in section 3.2.1. In a more general form, the surface is defined as follows:

$$z = p_a \cdot x^2 + p_b \cdot x \cdot y + p_c \cdot y^2 + p_d \cdot x + p_e \cdot y + p_f \tag{3.27}$$

Rewriting in matrix form yields:

$$z = \begin{bmatrix} x^2 & x \cdot y & y^2 & x & y & 1 \end{bmatrix} \begin{bmatrix} p_a & p_b & p_c & p_d & p_e & p_f \end{bmatrix}^T \tag{3.28}$$

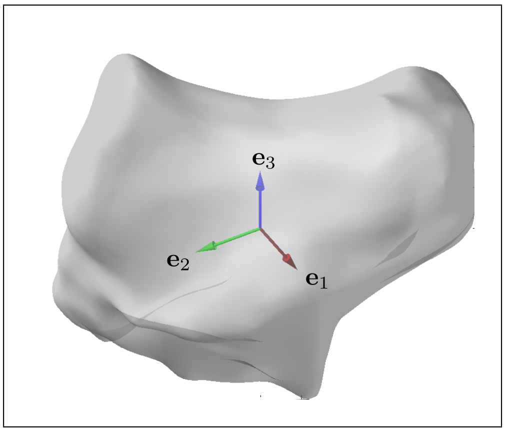

Figure 3.14.: Resulting eigenvectors of the principal component analysis of the trapezium

Solving for the parameters of the surface is conducted as follows:

$$\begin{bmatrix} p_a \\ p_b \\ p_c \\ p_d \\ p_e \\ p_f \end{bmatrix} = pinv\left(\begin{bmatrix} x_1^2 & x_1y_1 & y_1^2 & x_1 & y_1 & 1 \\ \vdots & \vdots & \vdots & \vdots & \vdots & \vdots \end{bmatrix}\right)\begin{bmatrix} z_1 \\ \vdots \end{bmatrix} \tag{3.29}$$

Applying a certain transformation ${}^{P}T_{I}$ to $\mathcal{V}_S$ eliminates all non-quadratic terms of formula 3.27. C_P and C_I denote the paraboloid and image coordinate system, respectively. In order to find this transformation, a nonlinear least-squares optimization in six dimensional pose space is conducted using MATLAB:

$$\mathbf{x}_{min} = \underset{\mathbf{x}}{min}||\mathbf{f}(\mathbf{x})||^2 = \underset{\mathbf{x}}{min}\left(f_1(\mathbf{x})^2 + ... + f_n(\mathbf{x})^2\right) \tag{3.30}$$

Euler angles and translation in x- y- and z-direction are denoted as $\mathbf{x}$. The function $\mathbf{f}(\mathbf{x})$ transforms $\mathcal{V}_S$ according to $\mathbf{x}$, conducts the least-squares fitting of the paraboloid using formula 3.29 and returns the paraboloid parameters:

$$\mathbf{f}(\mathbf{x}) = \begin{bmatrix} p_b(\mathbf{x}) & p_d(\mathbf{x}) & p_e(\mathbf{x}) & p_f(\mathbf{x}) \end{bmatrix}^T \tag{3.31}$$

The obtained equation of the paraboloid after optimization contains only the parameters p_a and p_c. The radius r of the circle approximating the curvature of the convexity of the trapezium at the origin delivers the offset for the coordinate system in z-direction of the paraboloid coordinate system C_P. The result of the optimization shows that the convex parabola lies in the x-z plane of C_P. Since in the x-z plane $y = 0$ and at the origin of the parabola $r = |1/\ddot{z}|$ (Bartsch 2007), the radius is calculated as follows:

$$r = \left|\frac{1}{2 \cdot p_a}\right| \tag{3.32}$$

Figure 3.15 (a) shows the fitted paraboloid with the respective coordinate system C_P. Translation along the z-axis of C_P and rotation of the x-axis about $-90°$ delivers the desired alignment of the trapezium coordinate system C_{TZ}, as depicted in figure 3.15 (b).

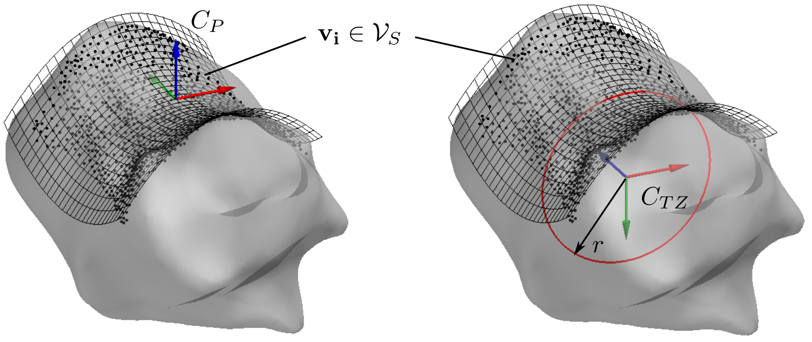

(a) Paraboloid Coordinate System *(b) Trapezium Coordinate System*

Figure 3.15.: Definition of the surface coordinate system of the trapezium based on least-squares fitting of a paraboloid

Formula 3.16 is used to derive the transformation matrices ${}^{I}\mathbf{T}_{MC1}$ and ${}^{I}\mathbf{T}_{TZ}$ for the first metacarpal bone and the trapezium, respectively. The vertices $\mathbf{v}_i$ have been defined in the image coordiante system C_I and are denoted as ${}^{I}v_i$ in the following. The local coordinates of the first metacarpal ${}^{MC1}\mathbf{v}_i$ are subsequently obtained as follows:

$$ {}^{MC1}\mathbf{v}_i = {}^{I}\mathbf{T}_{MC1}^{-1}\;{}^{I}\mathbf{v}_i \tag{3.33}$$

The same holds for the trapezium. All vertices of each surface are transformed into the respective local coordinate system. As a result, each bone can be represented in SIMPACK as a rigid body with a body fixed coordinate system and a locally defined surface. In order to restore the original position of the bone in SIMPACK, six parameters defining the pose have to be determined. The six parameters are derived from the homogeneous transformation matrix, which consists of a translational vector $\mathbf{t}$ and a rotational matrix $\mathbf{R}$:

$$\mathbf{T} = \begin{bmatrix} & \mathbf{R} & & \mathbf{t} \\ 0 & 0 & 0 & 1 \end{bmatrix} \tag{3.34}$$

The translation $\mathbf{t}$ can be adopted directly, whereas further computational steps are required to extract the angles from the rotational matrix $\mathbf{R}$. In SIMPACK, rotations are defined using Euler angles. Slabaugh (1999) proposes a simple technique to find Euler angles α, β and γ from a rotational matrix $\mathbf{R}$. It is defined as the following sequence of rotations:

$$\mathbf{R}(\alpha,\beta,\gamma) = \mathbf{R_z}(\gamma)\cdot\mathbf{R_y}(\beta)\cdot\mathbf{R_x}(\alpha) \tag{3.35}$$

The method is based on equating single numerical elements of $\mathbf{R}$ with the corresponding elements of $\mathbf{R}(\alpha,\beta,\gamma)$. SIMPACK uses a different sequence of rotations for the computation of $\mathbf{R}$:

$$\mathbf{R}(\alpha,\beta,\gamma) = \mathbf{R_x}(\alpha)\cdot\mathbf{R_y}(\beta)\cdot\mathbf{R_z}(\gamma) \tag{3.36}$$

Adapting the result of Slabaugh (1999) yields the angles required in SIMPACK:

$$\begin{aligned}\beta &= \arcsin(\mathbf{R}(1,3))\\ \alpha &= -\arctan\left(\frac{\mathbf{R}(2,3)/cos(\beta)}{\mathbf{R}(3,3)/cos(\beta)}\right)\\ \gamma &= -\arctan\left(\frac{\mathbf{R}(1,2)/cos(\beta)}{\mathbf{R}(1,1)/cos(\beta)}\right)\end{aligned} \tag{3.37}$$

$\mathbf{R}(1,3) = 1$ and $\mathbf{R}(1,3) = -1$ have to be handled as special cases, since $cos(\beta) = 0$ causes a division by zero. If $\mathbf{R}(1,3) = 1$:

$$\begin{aligned}\beta &= \pi/2\\ \alpha &= \arctan\left(\frac{\mathbf{R}(3,2)/cos(\beta)}{\mathbf{R}(2,2)/cos(\beta)}\right)\\ \gamma &= 0\end{aligned} \tag{3.38}$$

If $\mathbf{R}(1,3) = -1$:

$$\begin{aligned}\beta &= -\pi/2\\ \alpha &= \arctan\left(\frac{\mathbf{R}(2,1)/cos(\beta)}{\mathbf{R}(2,2)/cos(\beta)}\right)\\ \gamma &= 0\end{aligned} \tag{3.39}$$

Hence, a local coordinate system and a surface defined in this coordinate system can be computed for each bone, by conducting a principal component analysis of the first, second and third metacarpal and a paraboloid fit of the articulating surface of the trapezium. The original position of the bone can be restored in SIMPACK by applying the rotations and translations resulting from the respective transformation matrix.

Matching the detailled against the reference Surface

The original position of each bone represented in SIMPACK can be restored using the calculated Euler angles α, β and γ and the translation $\mathbf{t}$. This holds for all reference bones with surfaces defined in the reference image coordinate system C_I. However, the surfaces representing the cartilage are defined in the detail image coordinate system C_{ID} and require an additional transformation, which matches each bone of the detail image against the respective bone of the reference image. Hillenbrand (2008) developed a robust and general pose estimation algorithm intended for object detection. It was successfully applied for matching bone volumes segmented from MRI images by Stillfried (2009).

The pose estimation algorithm is based on statistically finding the most probable pose of an object in a scene, i.e. finding a transformation that matches two sets of points. For this purpose, a large number (in the order of 10^6) of parameter samples is computed. Each sample is obtained by calculating the rigid motion between a random point triple of one point set and a random, approximately congruent point triple of the other point set. The motion of the whole point set produces locations in parameter space with many, approximately coinciding parameter samples.

The most probable motion is determined using statistical methods.
Since the result of the pose estimation depends on the order of the points in the point set, it is repeated n times for n different permutations of the point set. Averaging the obtained results yields the mean rotation $\overline{\mathbf{R}}$ and mean translation $\overline{\mathbf{t}}$. $\overline{\mathbf{R}}$ is defined as the rotation minimizing the error to all calculated rotations $\mathbf{R_i}$ with respect to the angular distance (Stillfried et al. in press). The angular distance between two rotations $\mathbf{R}_1$ and $\mathbf{R}_2$ is calculated as follows:

$$angdist(\mathbf{R}_1, \mathbf{R}_2) = \arccos\left(\frac{1}{2}(trace(\mathbf{R}_2\mathbf{R}_1^{-1}) - 1)\right) \tag{3.40}$$

$\overline{\mathbf{R}}$ is subsequently computed as:

$$\overline{\mathbf{R}} = \underset{\mathbf{R}' \in SO(3)}{argmin} \left[\sum_{i=1}^{n} angdist(\mathbf{R}', \mathbf{R_i})\right] \tag{3.41}$$

$\overline{\mathbf{t}}$ minimizes the error of all translations $\mathbf{t}_i$ with respect to the euclidean distance. Hence, $\overline{\mathbf{t}}$ is the mean value of $\mathbf{t}_i$:

$$\overline{\mathbf{t}} = \frac{1}{n}\sum_{i=1}^{n} \mathbf{t}_i \tag{3.42}$$

In the following, the homogeneous transformation $\overline{\mathbf{T}}$ denotes the transformation with rotation $\overline{\mathbf{R}}$ and translation $\overline{\mathbf{t}}$. For both the first metacarpal bone and the trapezium, a transformation ${}^{I}\mathbf{T}_{ID}$ has to be determined. Determining the transformation individually for each bone is necessary since the posture of the CMC joint in the reference image is different to the posture in the detail image. Figure 3.16 depicts the result of the pose estimation for both the first metacarpal bone and the trapezium with $n = 100$. Since the faces $\mathcal{T}$ are not affected by the transformation, the surfaces are labeled with their respective set of vertices $\mathcal{V}$. ${}^{I}\mathcal{V}$ denotes vertices of the reference image, ${}^{ID}\mathcal{V}$ those of the detail image. Transformations applied to $\mathcal{V}$ are defined to transform each vertex $\mathbf{v}_i \in \mathcal{V}$.
The determination of the accuracy is possible only by visual inspection, whereas the precision of the pose estimation can be calculated as the variances of $\mathbf{R}_i$ and $\mathbf{t}_i$:

$$\sigma_r^2 = \frac{1}{n(n-1)}\sum_{i=1}^{n} angdist(\overline{\mathbf{R}}, \mathbf{R}_i)^2 \tag{3.43}$$

$$\sigma_t^2 = \frac{1}{n(n-1)}\sum_{i=1}^{n} ||\overline{\mathbf{t}} - \mathbf{t}_i||^2 \tag{3.44}$$

The standard deviations σ_r and σ_t for the pose estimation of trapezium and the first metacarpal bone are shown in table 3.4. Comparing the deviations yields that similar precision is achieved for both of the surfaces. However, angular deviations are large. The source of this error is most likely found in the segmented volumes, since the tissues are segmented manually from MRI images of different contrasts. An image of the whole hand with the same contrast as the detail image would solve the problem but imply a much longer scanning time. As a result, the angular deviation remains. Noticeable implications of this error evolve, for instance, during the determination of the static equilibrium, and have to be compensated (see section 3.5.2).
The result is visualized in figure 3.17 by displaying the intersection polygons of the matched surfaces of the detail image in the MRI slice of the reference image.

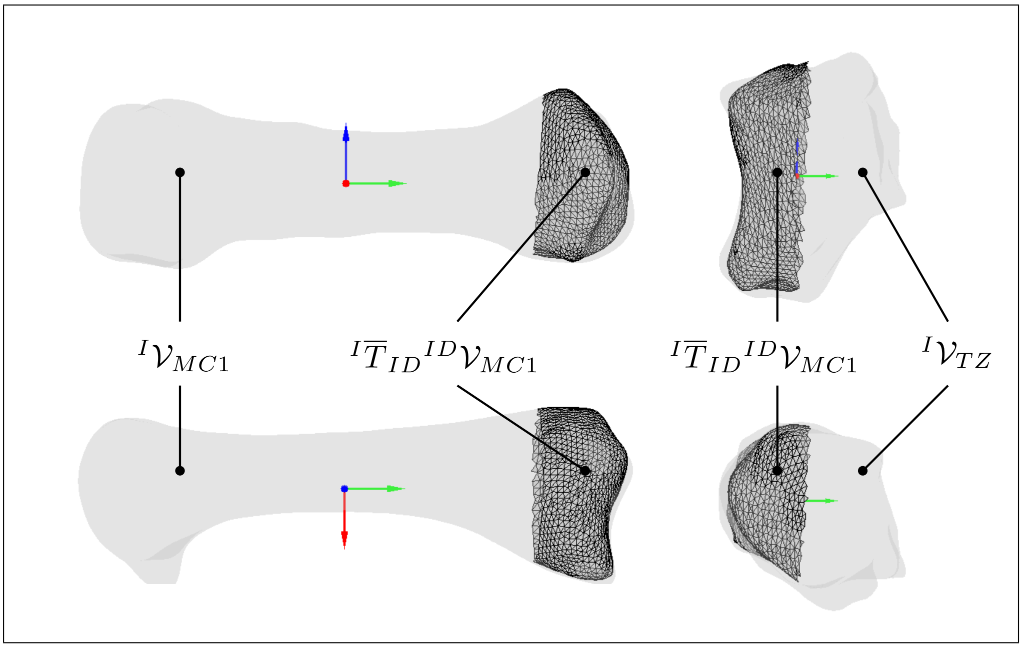

Figure 3.16.: Surfaces of the trapezium and the first metacarpal bone of the detail image matched against the surfaces of the reference image using the pose estimation algorithm

	n	σ_r [°]	σ_t [mm]
First Metacarpal	100	6.64	0.083
Trapezium	100	7.32	0.083

Table 3.4.: Precision of $n = 100$ pose estimations of the trapezium and first metacarpal bone

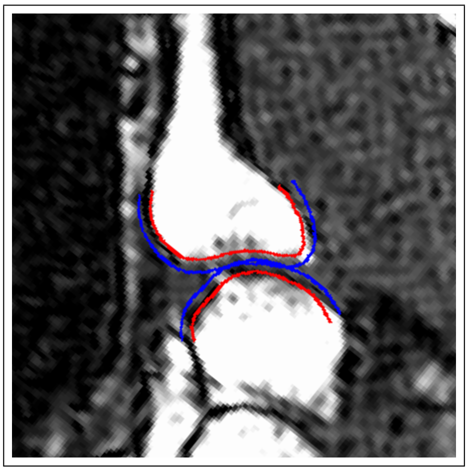

Figure 3.17.: Bone and cartilage surfaces of the detail image, matched against the surface of the reference image, intersected and displayed in a slice of the reference MRI image

For the simulation of the CMC joint, the surfaces of the first, second and third metacarpal and the trapezium are extracted from the reference image. The second and third metacarpal are supposed to serve as a reference for the attachment points of muscles and ligaments. The bone surfaces of first metacarpal and the trapezium of the detail image are matched against the bone surfaces of the reference image. Dilation of the bone surfaces of the detail image yields the cartilage surfaces. All extracted surfaces used in the simulation are displayed in figure 3.18.

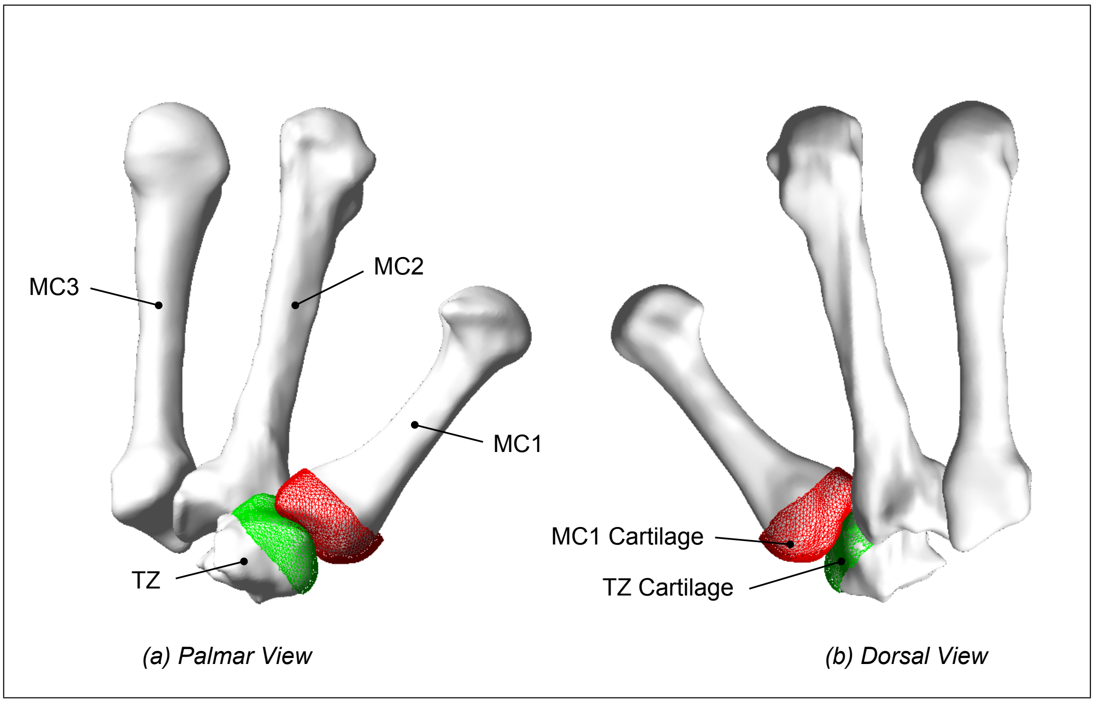

(a) Palmar View

(b) Dorsal View

Figure 3.18.: Overview of all surfaces created based on the MRI images for the use in the simulation of the CMC joint

3.2.2. Force Calculation

The previous sections dealt with obtaining the surface, i.e. the geometry of the contact. In order to compute the force and moment resulting from the intersection volume of the surfaces in contact, PCM is modified to account for the properties of articular cartilage. Based on PCM, a new user defined force element is developed in SIMPACK. Modifications involve a new user interface, as well as changes in the calculations of the contact force.

PCM is available in an open source version, which is incorporated in SIMPACK as a user defined force element. User defined force elements are generally written in the programming language FORTRAN, which also allows for calling C-routines. The PCM force element consists of a FORTRAN interface which calls several C-routines for the calculation of the contact forces and moments. Hence, modifications of the user interface and the contact force calculation have to be conducted in FORTRAN and C, respectively.

The user interface covers all parameter necessary for the calculation of the contact forces and allows for the choice of different operating modes. All inputs necessary for the calculations of the force element are depicted schematically in figure 3.19. Two types of inputs are distinguished: User inputs are defined once and constant over time. Inputs from the simulation are equivalent to the relative kinematics between two points or coordinate systems. Position and velocity data can be accessed directly in the force element.

For incorporating the contact geometry, PCM requires one file per surface, each containing a list of vertices and faces. The operating modes master/slave and 2-pass are elucidated in section 2.3.2. The cartilage thickness, cartilage response type and the range of deflection influence the contact stiffness. Tangential forces include only frictional forces and can be activated or deactivated. PCM requires the relative kinematics between the coordinate systems of the surfaces, i.e. the position and velocity vector, as well as the orientation and the angular velocities.

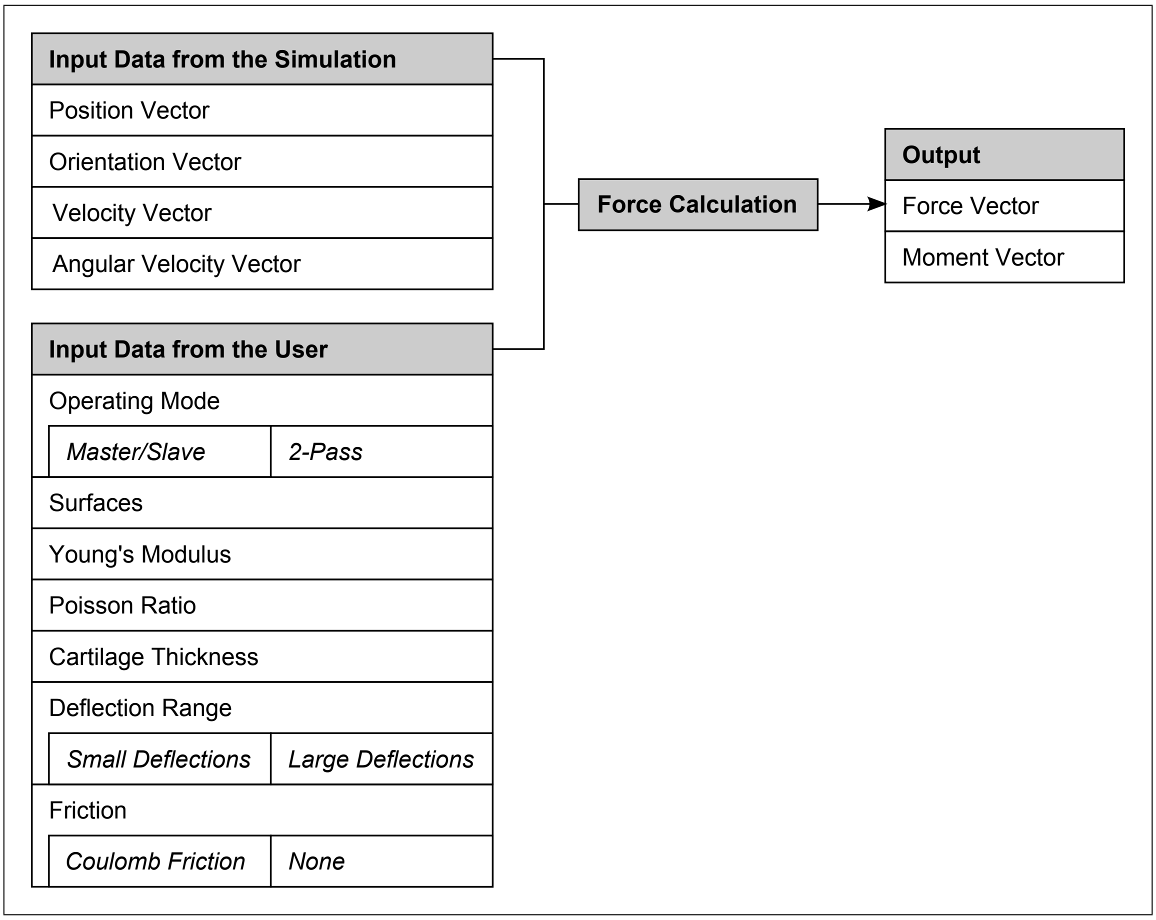

Figure 3.19.: Flow chart of the user defined contact force element based on PCM

The contact force calculations are based on the approaches of modelling the compressive behaviour of cartilage under conditions of fast loading and unloading, as found in literature (see section 2.2.4). The cartilage thickness is assumed to be identical for both surfaces, with identical material properties. This implies an equality of the layer stiffnesses $c_E = c_F$. Hence, the penetration ratio λ is calculated as:

$$\lambda = \frac{c_F}{c_E + c_F} = \frac{c_E}{2c_E} = 0.5 \tag{3.45}$$

and the calculation of the combined layer stiffness c simplifies to:

$$c = \frac{c_E \cdot c_F}{c_E + c_F} = \frac{c_E^2}{2c_E} = \frac{1}{2}c_E = \frac{1-\nu}{(1+\nu)(1-2\nu)} \cdot \frac{E}{2h} \tag{3.46}$$

The calculation of c requires the Young's modulus E, Poisson ratio ν and layer thickness h. The layer thickness is assumed to be $1\,\mathrm{mm}$, as estimated from the MRI images. Agreement on this estimation is found in literature An et al. (1990). Since there is a wide range of values for the Young's modulus and Poisson ratio (Blankevoort et al. 1991), the contact stiffness is adopted directly from An et al. (1990). Assuming $c = 1\,\mathrm{N/mm^{-3}}$ and $h = 1\,\mathrm{mm}$, values of E can be calculated depending on ν:

$$E = c \cdot 2h \cdot \frac{(1+\nu)(1-2\nu)}{1-\nu} \tag{3.47}$$

Choosing $\nu = 0.3$ yields $E = 1.48\,\mathrm{MPa}$. Hence, if only small deflections are considered, PCM can be used for modelling articular cartilage in fast response with E, ν and h as calculated above. For each active element k, the contact normal force F_{ck} is subsequently calculated as follows:

$$F_{ck} = c \cdot A_k \cdot u_{nk} \tag{3.48}$$

Taking large deflections into account, the stiffness is increased with increasing deflection u_{nk} as proposed from Blankevoort et al. (1991):

$$dF_{ck} = c \cdot A_k \cdot \frac{d(u_{nk}/(2h))}{1-(u_{nk}/(2h))} \tag{3.49}$$

Integration over the relative surface displacement $u_{nk}/(2h)$ yields:

$$F_{ck} = \int c \cdot A_k \cdot \frac{d(u_{nk}/(2h))}{1-(u_{nk}/(2h))} = -c \cdot A_k \cdot ln\left(1 - \frac{u_{nk}}{2h}\right) \tag{3.50}$$

Since time dependent effects of the materials are neglected in the simulation, viscoelasticity is not accounted for in this force element. The influence of friction is, however, controversially discussed in literature and incorporated in the cartilage model. In order to investigate changes of the movement due to frictional effects, it is possible to choose whether or not to calculate tangential forces. PCM calculations regarding friction are kept unchanged. Hence, a quadratic regularization of Coulomb's law of friction is used to calculate tangential forces. Values for the coefficient of friction μ for articular cartilage range between 0.001 and 0.03 (see section 2.2.5). The regularization velocity v_ϵ is determined empirically.

3.3. Modelling Muscles

The muscles serve as actuators of the joint, but also contribute to the joint stability. Hence, both active and passive force have to be considered. Similar to the process of modelling articular cartilage, two major steps are necessary: First, the geometry has to be determined. Since the muscles are modelled as point-to-point elements, it is necessary to identify representative attachment coordinates. Second, a force law has to be formulated, which yields the passive and active force in terms of the Hill model.

3.3.1. Geometry

The muscles are modelled as point-to-point elements. Hence, two points have to be defined for each muscle element, which represent the line of action. The following methods are considered for the determination of these points:

- Connecting the centroids of the areas of the attachment sites of each muscle
- Reconstructing the line of action from MRI images
- Using existing data from quantitative studies

The first method requires the results of quantitative studies of the attachment locations of the thumb moving muscles. In case such a study is not available, the attachment centroids have to be estimated from qualitative analysis. Schünke (2005) provides the locations of all the required attachments graphically. However, simply connecting the estimated centroids of these areas does not model the muscle line of action properly, since the muscle is naturally deflected by hypomochlions. As a result, this approach is not be pursued any further.
Using MRI data for the identification of the muscle lines of action yields several advantages: First, rather than the averaged values derived from either qualitative or quantitative studies, the tendons and muscles extracted from the MRI image correspond to the extracted surfaces. Second, the muscle does not have to be assumed to span directly from the origin to the insertion. Despite these advantages, this method can not be applied for all thumb moving muscles. Depending on the contrast of the MRI image, tendons are visible only as the absence of signal, i.e. appear as a dark line embedded in a bright region, as depicted in figure 3.20 (a). The muscle bellies appears bright in general, but cannot be distinguished from each other. Manual segmentation of the MRI images only allows for the reconstruction of the APL, EPL and FPL. For the reconstruction of the tendon line, the centroids of the segmented area of each slice are connected linearly, as depicted in figure 3.20 (b).

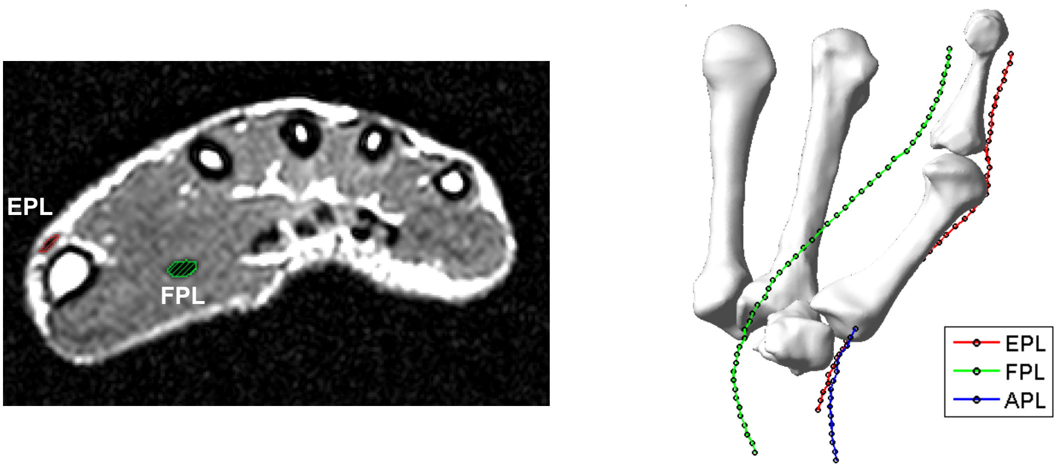

(a) EPL and FPL in MRI slice *(b) EPL, FPL and APL Centroid Line*

Figure 3.20.: Identification of tendons in an MRI slice and the results from reconstructing the respective centroid lines

Since modelling the muscle with only three muscles is hardly sufficient to reproduce the thumb motion in a plausible fashion, data from literature has to be used. An et al. (1979) presents a quantitative study of the tendon locations. For each joint, proximal and distal coordinates of the tendon line of action are determined. Since these points are chosen directly at hypomochlions, such as the end of a tendon sheath, bowstringing is likely to occur directly between the points. Using these points, the point-to-point force elements deliver a good approximation of the actual tendon line of action. In the study of An et al. (1979), tendon locations of all fingers are described except for the thumb. Wu et al. (2009) defines the locations of the tendons and muscles of the thumb in a similar fashion. However, Wu et al. (2009) only presents the results after the optimization of the muscle moment arms based on an experiment conducted by Smutz et al. (1998). Hence, it has to be accepted that the resulting tendon locations might have lost anatomical correspondence. Since no other literature source of the tendon locations of the thumb moving muscles is known to the author, the coordinates for the muscle force elements are adopted from Wu et al. (2009). The coordinates of eight muscles are provided: EPL, EPB, FPL, FPB, APL, AD, OP and APB. The AD is considered to consist of two bundles of muscle fibres. In order to account for the wide insertion area of each of these bundles, they are both modelled with two line elements. Hence, the AD is represented by four point-to-point connections, the remaining muscles by one point-to-point connection each. As a result, eleven couples of points are required for modelling all thumb moving muscles. The coordinates of these points are provided in tables and defined with respect to a proximal and a distal coordinate system of each joint. The coordinate systems are determined in a similar fashion to An et al. (1979): The proximal coordinate system is located in the approximate center of rotation of the head of the proximal bone and the distal coordinate system is located at the base of the distal bone. The x-axis points distally, the y-axis dorsally and the z-axis radially for the right hand. The coordinates of the muscles moving the CMC joint are defined in the proximal and distal CMC joint coordinate system and the proximal MCP joint coordinate system. They are denoted as $C_{CMC,P}$, $C_{CMC,D}$ and $C_{MCP,P}$ in the following. Except for the orientation of the axes, C_{TZ} was defined similar to $C_{CMC,P}$ (see section 3.2.1). Rotating C_{TZ} 90° about the z-axes yields $C_{CMC,P}$. $C_{CMC,D}$ and $C_{MCP,P}$ are derived by a $90\,^\circ$ rotation as applied to C_{TZ} and subsequent translation in the distal and proximal direction, respectively. The coordinate systems are depicted in figure 3.21.

The three sets of points of the muscles attachments are denoted as ${}^{CMC,P}\mathcal{A}_{CMC,P}$, ${}^{CMC,D}\mathcal{A}_{CMC,D}$ and ${}^{MCP,P}\mathcal{A}_{MCP,P}$ and defined in their respective coordinate system. For the use in Simpack, they have to be transformed into the body fixed coordinate systems of either the first metacarpal or the trapezium. The required transformation matrices are derived similar to formula 3.16. Applying the transformations and merging all coordinates defined relative to the first metacarpal bone yields:

$$\begin{aligned} {}^{MC1}\mathcal{A}_{D} &:= \left({}^{MC1}\mathbf{T}_{CMC,D}{}^{CMC,D}\mathcal{A}_{CMC,D}\right) \cup \left({}^{MC1}\mathbf{T}_{MCP,P}{}^{MCP,P}\mathcal{A}_{MCP,P}\right) \\ {}^{TZ}\mathcal{A}_{P} &:= {}^{TZ}\mathbf{T}_{CMC,P}{}^{CMC,P}\mathcal{A}_{CMC,P} \end{aligned} \tag{3.51}$$

The point sets ${}^{MC1}\mathcal{A}_{D}$ and ${}^{TZ}\mathcal{A}_{P}$ contain all attachment points defined in C_{MC1} and C_{TZ}, respectively. As a result, they can be directly incorporated in Simpack. Figure 3.22 shows all point-to-point elements using the defined coordinate systems and transformed coordinates. All coordinates are provided in chapter A of the appendix.

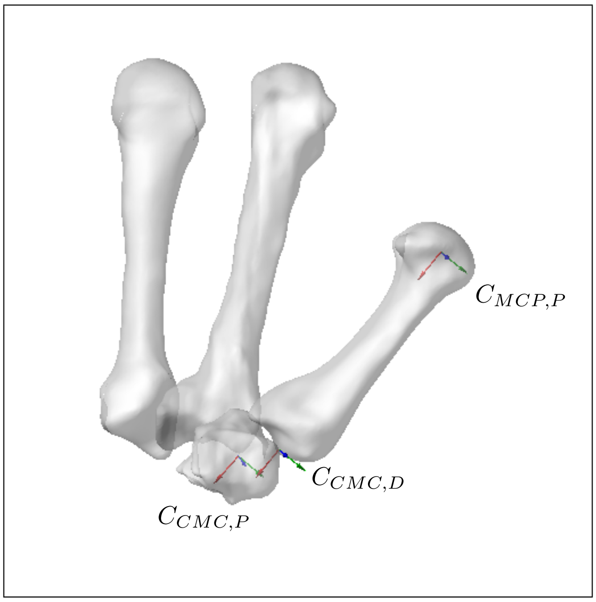

Figure 3.21.: Coordinate systems required for the definition of the muscle point-to-point elements

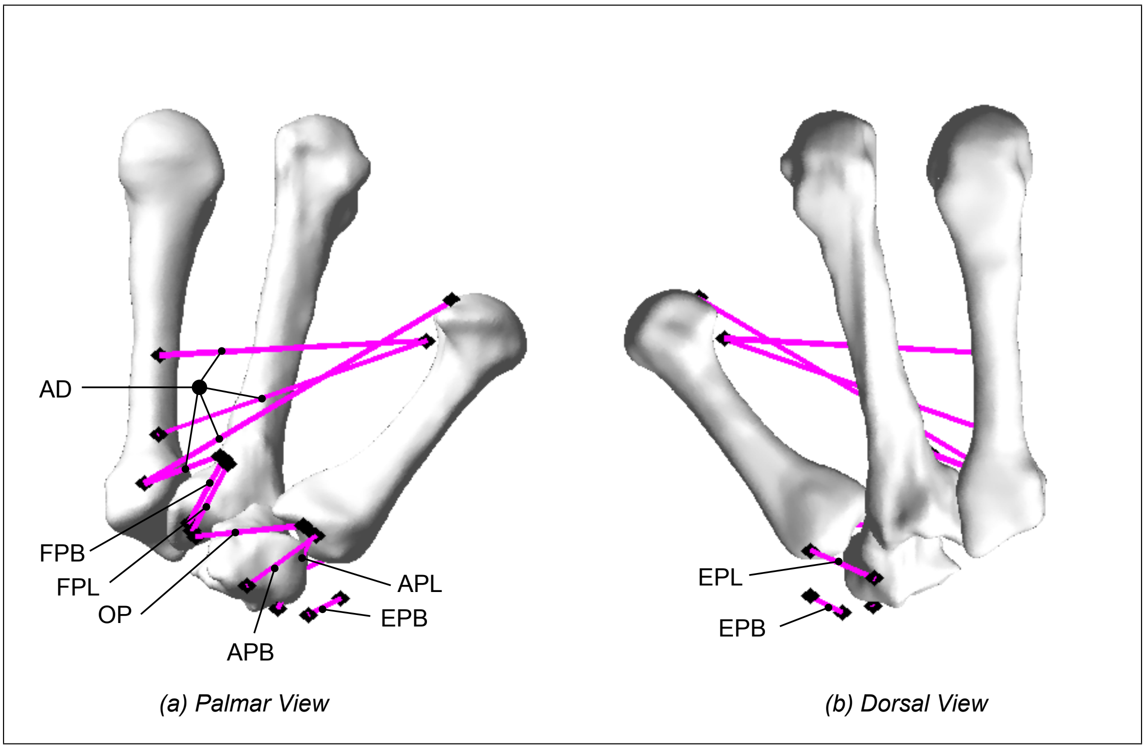

(a) Palmar View

(b) Dorsal View

Figure 3.22.: Overview of all elven muscle point-to-point elements, modelling eight muscles

3.3.2. Force Calculation

Similar to the articular cartilage, a user defined force element for the muscles is developed in Simpack. Both the user interface and the force calculations are written in Fortran. The calculations are based on modelling approaches found in literature (see section 2.2.3). The muscles are modelled either as a single, or multiple point-to-point force elements. The force calculations for muscles modelled with multiple force elements require additional calculations. These calculations are elucidated in the end of this section.

Figure 3.23 gives an overview of the input parameters required for the calculations of the muscle force. In order to account for the architecture of the muscles, the muscle architecture index, the muscle optimum length and the physiological cross sectional area are considered in the calculations. If the muscle is modelled with multiple force elements, the identities of all other force elements involved have to be defined. The initial strain is a means to account for the tension of the muscles in the reference position. The calculation of the initial strain is elucidated in section 3.5.2. The activation level controls the active force of the muscle and can be defined either as constant or as function of time. The required relative kinematics limit to the vector between the proximal and distal attachment point, i.e. the position vector.

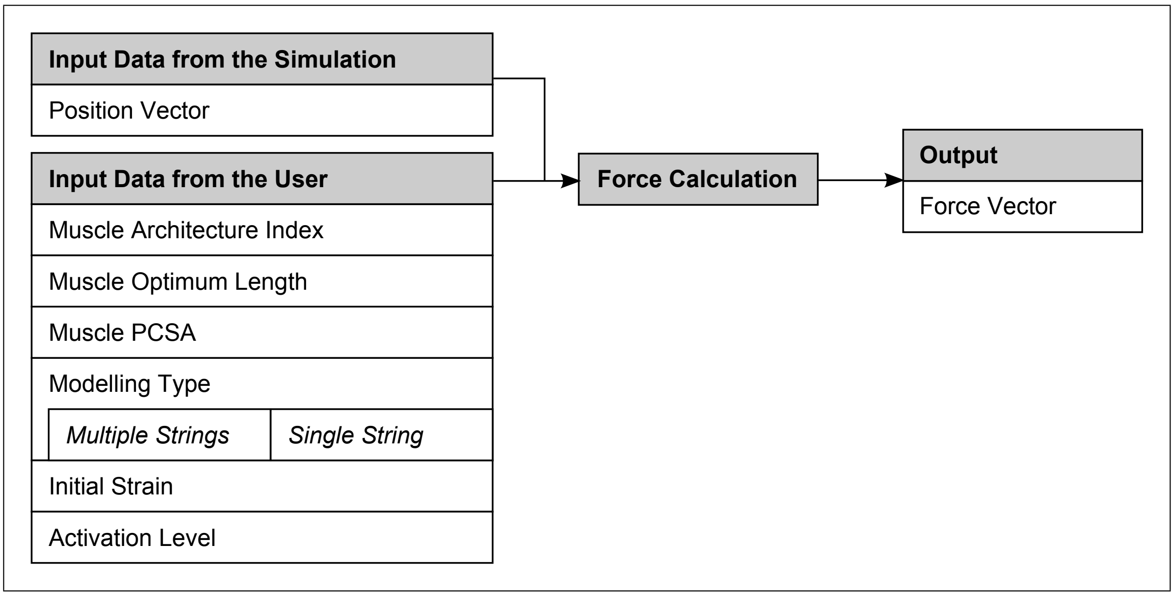

Figure 3.23.: Flow chart of the user defined muscle force element

Based on the input parameters, the active and passive force is calculated. The total force F is the sum of an active force F_A and a passive force F_P:

$$F = F_A + F_P \tag{3.52}$$

The force in a point-to-point element acts along the connection line of the proximal and distal attachment point of the force element. Simpack expects a force vector $\mathbf{F}$ to be returned from the force element. Given the vector $\mathbf{r}$ connecting the attachment points and defined in the reference coordinate system, F is calculated as:

$$\mathbf{F} = (F_A + F_P)\frac{\mathbf{r}}{||\mathbf{r}||} \tag{3.53}$$

The active force is considered to be muscle specific and dependent on the activation level and the current strain of the muscle. Since time dependent effects are neglected in the model, strain rate dependence is not be accounted for. Combining formula 2.4, formula 2.5 and formula 2.7 yields the current active force with the desired specification:

$$F_A = \alpha \cdot PCSA \cdot S_{max} \cdot e^{-\left[\frac{(\epsilon+1)^{[0.963+(1-1/i_a)]}-1}{0.353\cdot(1-i_a)}\right]^2} \tag{3.54}$$

The muscle maximum stress S_{max} is defined to be $35.4\,\mathrm{Ncm}^{-2}$, as used by Valero-Cuevas et al. (2003) for the simulation of thumb moving muscles. The physiological cross sectional area $PCSA$ and the architecture index i_a are muscle specific and taken from Jacobson et al. (1992) and Lieber et al. (1992). The current strain ϵ has to be defined with respect to the muscle optimum length l_0. Hence, it is calculated using the current distance r and the initial distance r_0 between the muscle attachments:

$$\epsilon = \frac{r - r_0}{l_0} + \epsilon_0 \tag{3.55}$$

The initial strain is denoted as ϵ_0 and added to the current strain. In order to calculate the passive force, the muscle is modelled as a nonlinear spring with exponential characteristics:

$$F_P = e^{c_1\epsilon + c_2} \tag{3.56}$$

The parameters c_1 and c_2 are determined based on the findings of Woittiez et al. (1984), that

$$\begin{aligned} F_P(0) &= 0.065 \cdot PCSA \cdot S_{max} \\ F_P(0.3) &= 0.87 \cdot PCSA \cdot S_{max} \end{aligned} \tag{3.57}$$

and calculated individually for each muscle as follows:

$$\begin{aligned} c_2 &= ln(0.065 \cdot PCSA \cdot S_{max}) \\ c_1 &= \tfrac{1}{0.3}\left(ln(0.087 \cdot PCSA \cdot S_{max}) - c_2\right) \end{aligned} \tag{3.58}$$

The calculations above hold for muscles modelled as a single string. For the calculation of muscles modelled with multiple strings, the strain is averaged. In case of the AD, the four strings are subdivided into two pairs of string. The PCSA of each pair was divided in half. Since the PCSA serves as a scale for both the active and passive force, the maximum forces are likewise divided. The averaged strain $\overline{\epsilon}$ is calculated for each pair of strings by accessing the distance between the attachment points of the second string r_2:

$$\overline{\epsilon} = \frac{(r - r_0) + (r_2 - r_{0,2})}{2l_0} + \epsilon_0 \tag{3.59}$$

The averaged active and passive forces are subsequently scaled by 0.5:

$$\begin{aligned} \overline{F_A} &= 0.5 \cdot \alpha \cdot PCSA \cdot S_{max} \cdot e^{-\left[\frac{(\overline{\epsilon}+1)^{[0.963+(1-1/i_a)]}-1}{0.353\cdot(1-i_a)}\right]^2} \\ \overline{F_P} &= 0.5 \cdot e^{c_1\overline{\epsilon}+c_2} \end{aligned} \tag{3.60}$$

This yields the advantage that individual strains are used for the calculation of the forces of each pair of strings representing the AD. Each of the eleven force elements modelling eight muscles subsequently return the force vector $\mathbf{F}$ to SIMPACK. The parameters used for modelling the muscles is provided in chapter B of the appendix.

3.4. Modelling Ligaments

The ligaments constrain the joint movement by exerting forces depending on their current strain. They are modelled as point-to-point force elements, similar to the muscles. Hence, the attachment points and the force law of the force elements have to be determined.

3.4.1. Geometry

Since the ligaments are modelled as point-to-point elements, geometrical aspects limit to the identification of representative points of attachment. The possibilities for the determination of the ligament attachment coordinates are similar to those of the muscles:

- Connecting the centroids of the areas of the attachment sites of each muscle
- Reconstructing the line of action from MRI images
- Using existing data from quantitative studies

Identifying the ligaments in the available MRI images is not feasible due to insufficient resolution and contrast. Hence, the attachment locations presented in the following have to be based on studies found in literature.

In comparison to the muscles, the ligaments are short and span directly between adjacent bones. As a result, the only hypomochlions influencing the line of action are the bones themselves. Connecting the centroids of the attachment areas thus provides a good approximation of the actual line of action. Since no publications of quantitative studies on the determination of the attachment points of ligaments are known to the author, the approach of connecting the centroids of the attachment areas is pursued.

Nanno et al. (2006) provides a detailled description of the attachment areas of the seven ligaments: dIML, pIML, UCL, DRL, sAOL, dAOL and POL. The quantitative data is averaged among the ten investigated specimen. The coordinates of the distal attachment centroids of the dIML, pIML, UCL and DRL are defined roughly with respect to the first metacarpal bone. Averaged values for the length of all ligaments are provided, including a tolerance region. Based on this data, the following approach is proposed to determine the locations of the ligament attachment points: First, the distal coordinates of all ligaments are either adopted from Nanno et al. (2006), or estimated based on qualitative studies. They are assumed to be directly connected to the bone, i.e. the bone surface obtained from the MRI images. Hence, each attachment point coincides with a vertex of the surface of the first metacarpal bone. Second, vertices of the trapezium and the second metacarpal within the tolerance length are calculated. Using qualitative studies, one of these vertices is selected to represent the proximal point of attachment. These two steps are conducted for each ligament. Since the insertion areas of the sAOL and the POL are wide compared to the remaining ligaments, they are modelled with two strings each. In total, the geometry of nine point-to-point elements has to be determined.

Figure 3.24 depicts the locations of the distal attachments at the surface of the first metacarpal bone. The y-axis of the 2D coordinate system defined by Nanno et al. (2006) coincides with the dorsal edge of the bone, the x-axis lies in the plane perpendicular to the dorsal edge passing through the most distal point of the articular surface. The 3D coordinates are calculated by intersecting the surface of the first metacarpal surface with a line perpendicular to both x and y. The set of 3D coordinates of the distal ligament attachments is denoted as $\mathcal{A}_D$. The coordinates of both the distal and proximal are defined in the body fixed coordinate systems C_{MC1} and C_{TZ} and do not require any transformation.

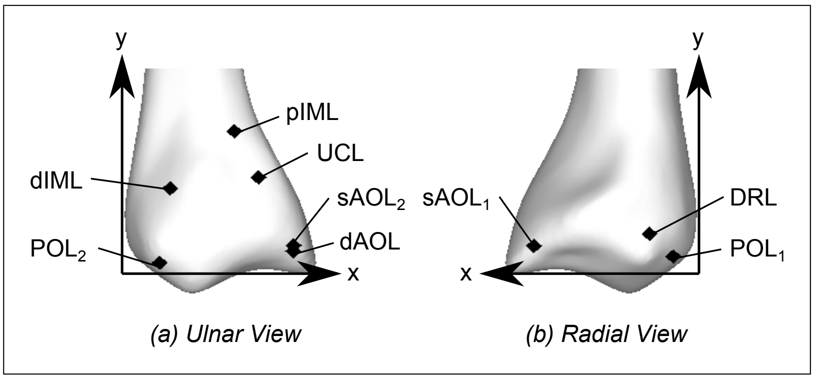

(a) Ulnar View *(b) Radial View*

Figure 3.24.: Distal ligament attachments at the surface of the first metacarpal bone

Using the minimal length l_{min} and maximal length l_{max}, a set of valid vertices $\mathcal{V}_P$ representing the proximal attachment points is found for each ligament. Hence, $\mathcal{V}_P$ is a subset of the vertices $\mathcal{V}$ of either the trapezium or the second metacarpal bone and generally defined as:

$$\mathcal{V}_P := \{l_{min} < ||\mathcal{A}_D - \mathbf{v}_i|| < l_{max} \mid \mathbf{v}_i \in \mathcal{V}\} \tag{3.61}$$

One point $\mathbf{p}_P \in \mathcal{V}_P$ represents the proximal attachment point of a ligament. As an example, the DRL attachment point $\mathbf{p}_{DRL,P}$ and the set of valid proximal attachment points $\mathcal{V}_{DRL,P}$ are displayed in figure 3.25. The selection of the point representing the proximal attachment is conducted based on the qualitative data provided by Nanno et al. (2006). In order to be able to compare the attachment areas, one representative vertex is chosen, and all vertices within a certain tolerance of angular distance from the distal attachment location are highlighted. In figure 3.25 they are denoted as $\mathcal{V}_{DRL,P,A}$.

This method holds for all ligaments except for the UCL. The UCL attaches to the transverse carpal ligament (TCL), which spans from the trapezium to the hamatum. In order to determine valid points for the UCL, a connection line representing the TCL is defined based on qualitative data. Hence, calculating points on this line within l_{min} and l_{max} yields the valid proximal attachment points for the UCL. Figure 3.26 depicts the connection lines of the proximal and distal attachment points of the nine force elements modelling the seven ligaments. All coordinates are provided in chapter A of the appendix.

Except for the UCL, all ligaments are modelled using the lengths provided by Nanno et al. (2006). The length of the UCL in this modelling approach slightly exceeds the tolerance region.

3.4.2. Force Calculation

Ligaments are represented in Simpack as user defined force elements. The calculations are based on the approaches found in literature (see section 2.2.2). Since time dependence is not considered, ligaments are modelled as nonlinear springs, exerting the force point-to-point. Except for the sAOL and the POL, a single string represents each ligament.

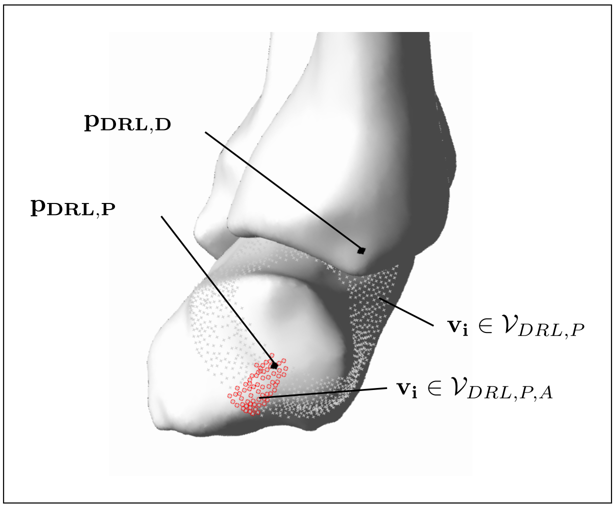

Figure 3.25.: Determination of the proximal attachment point of the DRL, based on qualitative studies found in literature and the ligament minimum and maximum length

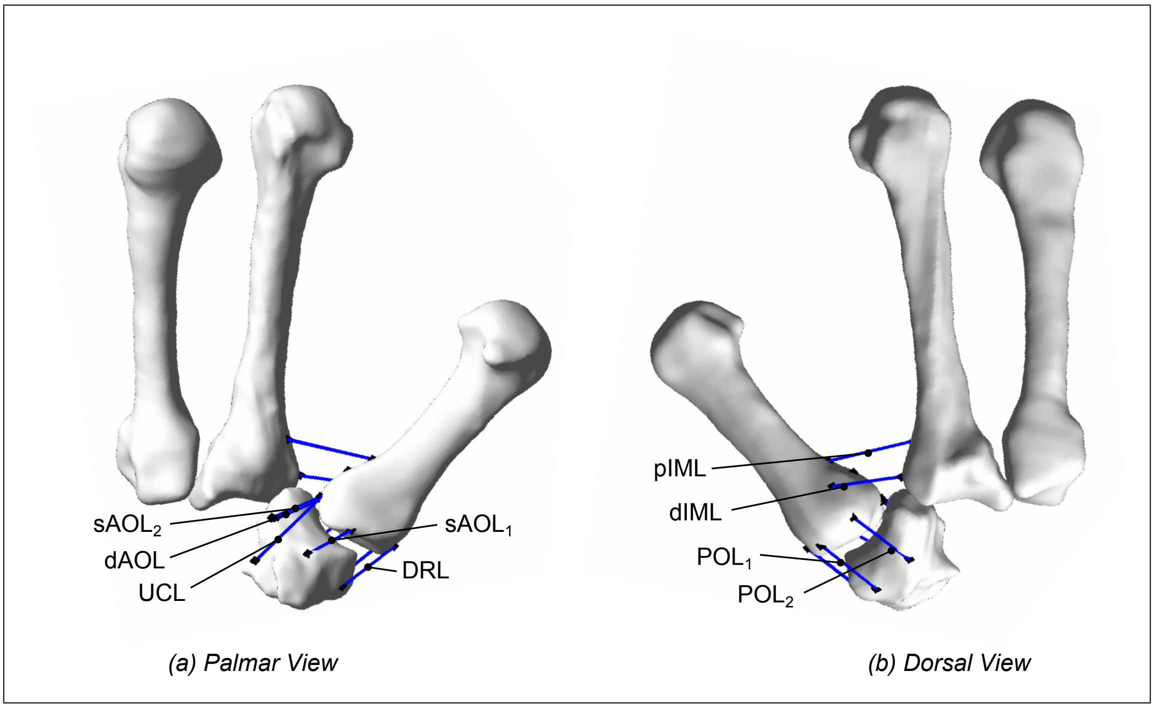

(a) Palmar View

(b) Dorsal View

Figure 3.26.: Overview of all nine ligament point-to-point elements, modelling seven ligaments

Similar to the muscle force element, the force calculation accounts for the architecture of the tissue. The muscle architecture involves the alignment of the fibres, the cross sectional area and the optimum length. Ligaments consist of highly parallel collagen fibres, thus, scaling the ligament force is conducted with respect to the cross sectional area only. The initial ligament length allows to define an initial tension in the reference position. All necessary input parameters are entered in the user interface of the force element and depicted schematically in figure 3.27. Similar to the muscle force element, only the position vector between proximal and distal attachment points has to be accessed for the force calculation.

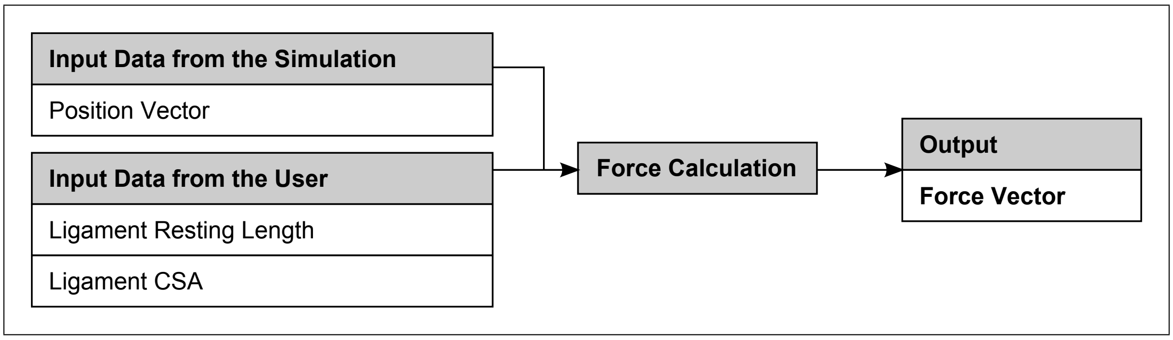

Figure 3.27.: Flow chart of the user defined ligament force element

For the calculation of the force vector $\mathbf{F}$ acting along the connection line between the proximal and distal point of attachment, the vector $\mathbf{r}$ and a scalar force F are required:

$$\mathbf{F} = F \cdot \frac{\mathbf{r}}{||\mathbf{r}||} \tag{3.62}$$

F is calculated depending on the cross sectional area (CSA) of the ligament, the initial length l_0 and the current distance r between the points of attachment. The initial length l_0 allows for initial forces in the ligaments and does not necessarily correspond to the initial distance r_0 between the attachment points. Calculation of l_0 is elucidated in section 3.5.2. In order to scale the ligament forces, the average CSA of all ligaments $\overline{CSA}$ is determined using the data from Nanno et al. (2006):

$$\overline{CSA} = \frac{1}{n}\sum_{i=1}^{n} CSA_i = 7.27\,\mathrm{mm}^2 \tag{3.63}$$

The force F is subsequently determined by modifying formula 2.1:

$$F = \begin{cases} \frac{CSA}{\overline{CSA}} \cdot K \cdot (r - l_0)^2 & \text{for } r > l_0 \\ 0 & \text{for } r \leq l_0 \end{cases} \tag{3.64}$$

The stiffness constant K is adopted from Sancho-Bru et al. (2001) and defined as $750\,\mathrm{N/cm}^2$. Since formula 2.1 yields tensile forces also for $r \leq l_0$, forces for negative displacements are set to zero. For the calculation of the force of ligaments modelled with multiple strings, the CSA is divided by the number of strings. The parameters of all ligaments are provided in chapter B of the appendix.

Angle	Movement
α	Adduction (+) Abduction (-)
β	Pronation (+) Supination (-)
γ	Flexion (+) Extension (-)

Table 3.5.: Interpretation of the kinematics of the first metacarpal in terms of functional anatomy

3.5. Assembling the Model of the CMC Joint

In the previous sections, the process of modelling cartilage, muscles and ligaments was elucidated in detail. The complete biomechanical model of the CMC joint consists of a fixed and an unconstrained body, one cartilage contact force element, eleven muscle force elements and nine ligament force elements. The fixed body represents the trapezium, the unconstrained body the first metacarpal. The surfaces of the bones of the first, second and third metacarpal as well as the trapezium are incorporated for visualization only, since the contact force is calculated depending only on the cartilage surfaces.

3.5.1. The Model of the CMC Joint in SIMPACK

All the components mentioned are assembled in SIMPACK. Since the joint state is defined with respect to the reference coordinate system all bones are transformed into the trapezium coordinate system. This allows for the comparison to functional anatomy. In SIMPACK, the orientation of a joint is represented as the Euler angles computed from the rotational matrix, similar to formula 3.37. Since the orientation of the first metacarpal bone is measured with respect to the coordinate system of the trapezium, it can be interpreted as denoted in table3.5.
The proximal and distal attachment points have already been transformed into the coordinate system of the trapezium and the first metacarpal, respectively. For the moving bone it is necessary to define the moment of inertia and the mass. In the model of the CMC joint, only the inertial effects of the first metacarpal are considered. In fact, the mass and moment of inertia of the whole thumb affect the CMC joint dynamics. However, the model should serve for kinematic investigations only for which rough estimations are considered to be sufficient. The geometry of the thenar is approximated by a cylinder with a diameter of $d = 25\,\mathrm{mm}$ and a height of $h = 50\,\mathrm{mm}$. The density of bone, including tissue is assumed to be $\rho = 1100\,\mathrm{kg/m^3}$ (Sancho-Bru et al. 2001), thus the mass is calculated as follows:

$$m = \rho \frac{d^2 \cdot \pi \cdot h}{4} = 26.99\,\mathrm{g} \tag{3.65}$$

Since the axes of the coordinate system of the first metacarpal bone were derived by principal component analysis of the the surface, they are assumed to coincide with the principal axes of inertia. Hence, only the principal moments of inertia of the cylinder have to be calculated (Hibbeler 2006):

$$\begin{aligned} I_{xx} = I_{zz} &= \tfrac{m}{12}(3r^2 + h^2) = 6.68\,\mathrm{Nmm}^2 \\ I_{yy} &= \tfrac{m \cdot r^2}{2} = 2.11\,\mathrm{Nmm}^2 \end{aligned} \tag{3.66}$$

All bones except for the first metacarpal are fixed, thus it is not necessary to compute the respective masses and moments of inertia. Finally, all modelled components can be assembled in SIMPACK. Figure 3.28 shows the surfaces of all bones extracted from the reference image, the cartilage surfaces of the trapezium and the first metacarpal as well as the force elements representing the ligaments and the muscles.

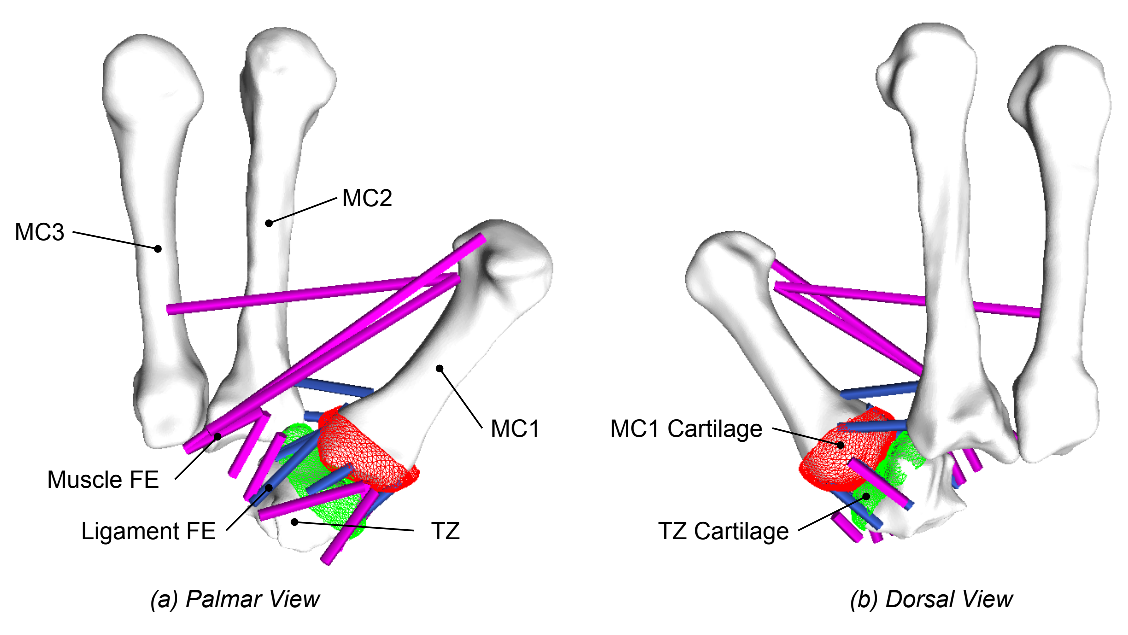

(a) Palmar View

(b) Dorsal View

Figure 3.28.: The model of the CMC joint in SIMPACK, including the bones (white), cartilage surfaces of the first metacarpal (red) and trapezium (green), the ligament force elements (blue) and the muscle force elements (purple)

3.5.2. Determining the Static Equilibrium Position

In the reference position, the cartilage surfaces penetrate each other and cause a contact force. Hence, it is necessary to determine the ligament and passive muscle force that retains the first metacarpal in the initial position. A solution is obtained in three steps: First, the forces of all 20 force elements are determined by solving the linear system of equations resulting from the static equilibrium conditions. Second, the initial strains and lengths are calculated for the muscle and ligament force elements respectively. Third, SIMPACK is used to find a static equilibrium position of the first metacarpal with the given initial strains and lengths.

The static equilibrium conditions deliver six linear equations: Three for the forces and three for the moments. Since the initial forces of 20 force elements are unknown, the system is underdetermined. Moreover, ligaments and muscles can exert only tensile forces, thus only positive forces yield a solution. As a result, the system of equations has to be solved by constrained optimization. The conditions of static equilibrium are:

$$\begin{aligned} \sum \mathbf{F} = \mathbf{0} \\ \sum \mathbf{M} = \mathbf{0} \end{aligned} \tag{3.67}$$

The force and moment vector resulting from the contact in the initial position is denoted as $\mathbf{F}_0$ and $\mathbf{M}_0$ respectively. The unknown forces of the force elements are denoted as $F_1, \ldots, F_i, \ldots, F_{20}$. Denoting $\mathbf{n}_i$ as the unit vector pointing from the distal to the proximal point of attachment defined in C_{MC1}:

$$\mathbf{n}_i = \frac{\mathbf{p}_{P,i} - \mathbf{p}_{D,i}}{||\mathbf{p}_{P,i} - \mathbf{p}_{D,i}||} \tag{3.68}$$

and $\mathbf{r}_i$ as the vector pointing from the origin of C_{MC1} to the distal attachment point $\mathbf{p}_{D,i}$:

$$\mathbf{r_i} = \mathbf{p}_{D,i} \tag{3.69}$$

the static equilibrium conditions are:

$$\begin{aligned} \textstyle\sum_{i=1}^{20} F_i \cdot \mathbf{n_i} = -\mathbf{F_0} \\ \textstyle\sum_{i=1}^{20} F_i \cdot (\mathbf{r_i} \times \mathbf{n_i}) = -\mathbf{M_0} \end{aligned} \tag{3.70}$$

Rewriting in matrix form yields:

$$\begin{bmatrix} \mathbf{n_1} & \cdots & \mathbf{n_{20}} \\ \mathbf{r_1} \times \mathbf{n_1} & \cdots & \mathbf{r_{20}} \times \mathbf{n_{20}} \end{bmatrix} \begin{bmatrix} F_1 \\ \vdots \\ F_{20} \end{bmatrix} = \begin{bmatrix} -\mathbf{F_0} \\ -\mathbf{M_0} \end{bmatrix} \tag{3.71}$$

Formula 3.71 is used to conduct a constrained linear least-squares optimization in MATLAB which minimizes the vector $\mathbf{x}$ containing all ligament forces within the boundaries $\mathbf{x}_{lb}$ and $\mathbf{x}_{ub}$:

$$\mathbf{x}_{min} = \underset{\mathbf{x}}{min} \tfrac{1}{2} ||\mathbf{A}\mathbf{x} - \mathbf{b}||^2 \quad \text{such that} \quad \mathbf{x}_{lb} \leq \mathbf{x} \leq \mathbf{x}_{ub} \tag{3.72}$$

with:

$$\begin{aligned} \mathbf{A} &= \begin{bmatrix} \mathbf{n_1} & \cdots & \mathbf{n_{20}} \\ \mathbf{r_1} \times \mathbf{n_1} & \cdots & \mathbf{r_{20}} \times \mathbf{n_{20}} \end{bmatrix} \\ \mathbf{x} &= \begin{bmatrix} F_1 & \cdots & F_{20} \end{bmatrix}^T \\ \mathbf{b} &= \begin{bmatrix} -\mathbf{F_0} & -\mathbf{M_0} \end{bmatrix}^T \end{aligned} \tag{3.73}$$

The ligament forces are represented by $F_1 \ldots F_9$, the muscles forces by $F_{10} \ldots F20$. Lower and upper bounds have to be determined individually for ligaments and muscles. To ensure that only tensile forces result from the optimization, the lower bound has to be greater or equal to zero for both the ligaments and the muscles. No upper boundary for the ligament forces is necessary, however, a value of $200\,\mathrm{N}$ is estimated to serve as a physiological boundary. The boundaries of the muscles forces have to account for the fact that due to the exponential force law, a force equal to zero would require an infinite deflection of the assumed spring. As a result, no active force could be exerted due to its strain dependence. Defining the lower and upper bounds with respect to the passive muscle force in the unstrained state diminishes this problem. Adapting these boundaries for each muscles also allows to deal with large displacements of certain muscles. The boundaries for the ligaments and muscles are defined as follows:

$$x_{lb,i} = \begin{cases} 0 & \text{for } 1 \leq i \leq 9 \\ 0.02 \cdot F_{max,i} & \text{for } 10 \leq i \leq 20 \end{cases} \tag{3.74}$$

$$x_{ub,i} = \begin{cases} 200 & \text{for } 1 \leq i \leq 9 \\ 0.11 \cdot F_{max,i} & \text{for } 10 \leq i \leq 20 \end{cases} \tag{3.75}$$

F_{max} is calculated for each muscle with formula 2.7. Since the passive force F_{P0} in the unstrained state is defined as 6.5% of F_{max}, the chosen boundaries for the muscle forces represent a region of $\mp 4.5\%$ of F_{max} about F_{P0}. Formula 3.75 holds for all muscles except for the EPL and the EPB, which are the only extensor muscles. The lower boundary is defined as the respective value of F_{P0} to ensure that active force can be developed at a scale similar to the remaining muscles, which are mainly flexors.

The initial strains $\epsilon_{0,i}$ for the muscles and the initial lengths $l_{0,i}$ for the ligaments are calculated using the force laws described in section 3.3.2 and 3.4.2 respectively:

$$\epsilon_{0,i} = \frac{ln(F_i) - c_2}{c_1} \tag{3.76}$$

$$l_{0,i} = r - \sqrt{F_i \cdot \frac{\overline{CSA}}{K \cdot CSA}} \tag{3.77}$$

Formula 3.76 holds for single string muscles only. For muscles modelled with two strings, the force F_i has to be doubled. As the optimization is constrained by the given boundaries, a residual representing forces and moments is likely to remain. Hence, calculating the initial strains and lengths for the obtained forces still causes a movement of the bone in the simulation. In order to account for the residual, SIMPACK is used to determine the static equilibrium position of the bone, i.e. the position in which accelerations become zero:

$$\ddot{\mathbf{z}} = f(\mathbf{z}, \dot{\mathbf{z}}, t) = \mathbf{0} \tag{3.78}$$

The state vector $\mathbf{z}$ contains all translational and rotational state variables of the joint to be determined. Since the resulting system of equations is nonlinear, SIMPACK applies iterative methods to find a solution. The static equilibrium position deviates from the original position of the reference posture, as depicted in figure 3.29.

The euclidean distance amounts to $8.43\,\mathrm{mm}$, the angular distance to $14.14\,°$. The movement resulting from the residual appears similar to flexion. Since the static equilibrium position represents a physiologically feasible position, it is considered a valid starting point for conducting kinematic simulations. The initial parameters for both muscles and ligaments are provided in chapter B of the appendix.

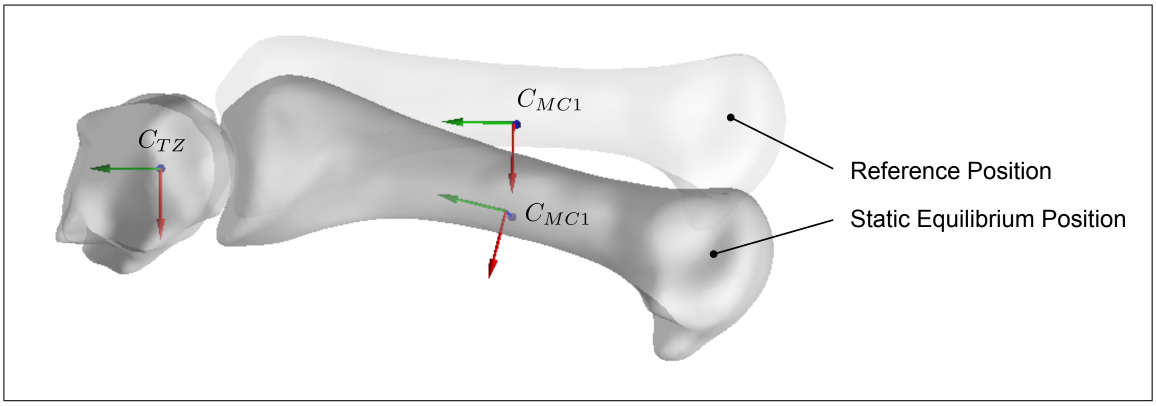

Figure 3.29.: Reference and static equilibrium position of the first metacarpal bone

3.5.3. Conducting Simulations

At the beginning of each simulation, the first metacarpal bone remains at its initial position, since the equilibrium conditions are satisfied. Subsequently, single or multiple muscles are activated by a function defining the activation level $\alpha(t)$ for each muscle. If the activation level remains constant, the bone moves until the equilibrium conditions are satisfied for the force applied by the activated muscles. During the simulation, the joint state history is measured and provided for post processing. Additionally, each force element produces individual output values, such as the contact force, contact area and the penetration depth. Figure 3.30 depicts the inputs and outputs of the simulation of the CMC joint schematically. The state vector $\mathbf{x}$ contains the position, orientation and respective velocities of the joint. Solving the system of ordinary differential equations $\dot{\mathbf{x}} = f(t, \mathbf{x})$ numerically yields the state vector $\mathbf{z}(t)$.

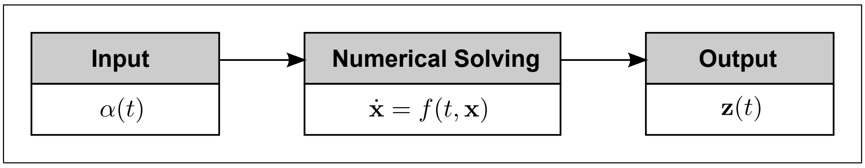

Figure 3.30.: A schematic depiction of the simulation of the CMC joint movement in SIMPACK

Simulations in time domain are conducted in SIMPACK by establishing and solving a nonlinear system of equations by numerical integration. The principle behind the derivation of this system of equations is elucidated in section 2.3.2. Hippmann (2004) compares the efficiency of different numerical solvers for the use with PCM. The differential algebraic system solver (DASSL) has shown best performance with PCM and is chosen also for the simulations of the CMC joint. The functionality of DASSL is explained in detail by Hippmann (2004). The accuracy of the numerical integration is influenced by the absolute and relative tolerance of the solver. Roughly, the absolute tolerance corresponds to the error of the state variables in meters and radiants respectively and the relative tolerance can be defined equal to the absolute tolerance. It is set to $5 \cdot 10^{-5}$ for all simulations conducted. The initial and maximum step size of the integrator is set to $1 \cdot 10^{-13}$ and $1 \cdot 10^{-4}$ respectively. For the remaining parameters, the default values are chosen.

4. Results

The CMC joint of the thumb has been modelled in SIMPACK including articulating surfaces, ligaments and muscles as described in chapter 3. Based on this biomechanical model, several simulations in time domain are conducted in order to determine parametric influences and the plausibility of movements due to muscle activation. The movements are represented by the history of state vectors after time integration, i.e. the position and orientation of the body fixed coordinate system of the first metacarpal bone with respect to the reference coordinate system. The reference coordinate system coincides with the body fixed coordinate system of the trapezium and allows for the interpretation of the movement in terms of functional anatomy. Additional simulation outputs, such as the forces exerted by the individual force elements, are presented in chapter C of the appendix.

4.1. Parametric Influences

In this section, the influences of certain parameters on the joint kinematics are investigated. For this purpose, a strong flexion movement is conducted and the properties of the contact stiffness, the ligament stiffness and the friction are varied. The flexion movement results from fully activating the ADP, FPL, FPB, OPP and the APB. The respective activation levels $\alpha(t)$ are defined as:

$$\alpha(t) = \begin{cases} 0 & \text{for } 0 \leq t < 0.1 \\ 3.3 \cdot t & \text{for } 0.1 \leq t < 0.4 \\ 1 & \text{for } 0.4 \leq t \end{cases} \tag{4.1}$$

indicating a linear increase of the activation level from $t = 0.1\,\mathrm{s}$ to $t = 0.4\,\mathrm{s}$. The time integration is conducted from $t = 0\,\mathrm{s}$ to $t = 0.5\,\mathrm{s}$.

The results from time integration are compared regarding the state of the first metacarpal bone, i.e. position and orientation with respect to the trapezium coordinate system. For each time step delivered by time integration, the angular distance d_a and the euclidean distance d_e of the transformations is calculated. The average of these differences over the whole duration of the simulation serves as a measure for the influence of the parameter on the joint kinematics. Using formula 3.40 for the angular distance, the difference at each time step is calculated as follows:

$$\begin{aligned} d_a(t) &= angdist(\mathbf{R}_1(t), \mathbf{R}_2(t)) \\ d_e(t) &= \mathbf{t}_2(t) - \mathbf{t}_1(t) \end{aligned} \tag{4.2}$$

The average distances $\overline{d_a}$ and $\overline{d_e}$ are subsequently computed as the mean of the distances of all evaluated time steps n:

$$\begin{aligned} \overline{d_a} &= \tfrac{1}{n} \textstyle\sum_{i=1}^{n} angdist(\mathbf{R}_{1,i}, \mathbf{R}_{2,i}) \\ \overline{d_e} &= \tfrac{1}{n} \textstyle\sum_{i=1}^{n} \mathbf{t}_{2,i} - \mathbf{t}_{1,i} \end{aligned} \tag{4.3}$$

Both $\overline{d_a}$ and $\overline{d_e}$ and the final distances $d_a(0.5)$ and $d_e(0.5)$ are computed to determine the influence of the respective parameters.

4.1.1. Contact Stiffness

In general, the contact stiffness is assumed to be nonlinear for the model in order to account for the large displacements of the cartilage. In this section, the differences between linear and nonlinear contact stiffness are investigated regarding the joint kinematics. The Young's modulus and Poisson ratio are are kept unchanged, only the effect of stiffness increase is neglected in the linear approach. The results are displayed in table 4.1.

	$\overline{d_a}$ $[^\circ]$	$d_a(0.5)$ $[^\circ]$	$\overline{d_e}$ $[\mathrm{mm}]$	$d_e(0.5)$ $[\mathrm{mm}]$
Linear vs. Nonlinear Contact Stiffness	0.502	0.601	0.383	0.44

Table 4.1.: Average and final distances of the joint orientation and position due to different contact stiffness modelling approaches

The magnitude of the deviations caused by the change of the contact stiffness modelling is small, especially compared to the precision of the pose estimation (see table 3.4). In order to determine the influence of the variation of the contact modelling approach on the joint kinematics, the angles of adduction/abduction and pronation/supination are plotted against the angle of flexion/extension in figure 4.1. This visualization provides a practical and compact view on the movement and deviations caused by parameter variation. Even though the differences are small, it is obvious that the linear contact modelling slightly enlarges the range of motion. Since the linear approach causes a softer contact at higher strains, it can be concluded that the contact stiffness influences the joint kinematics in a manner that the range of motion gets larger as the contact gets softer.

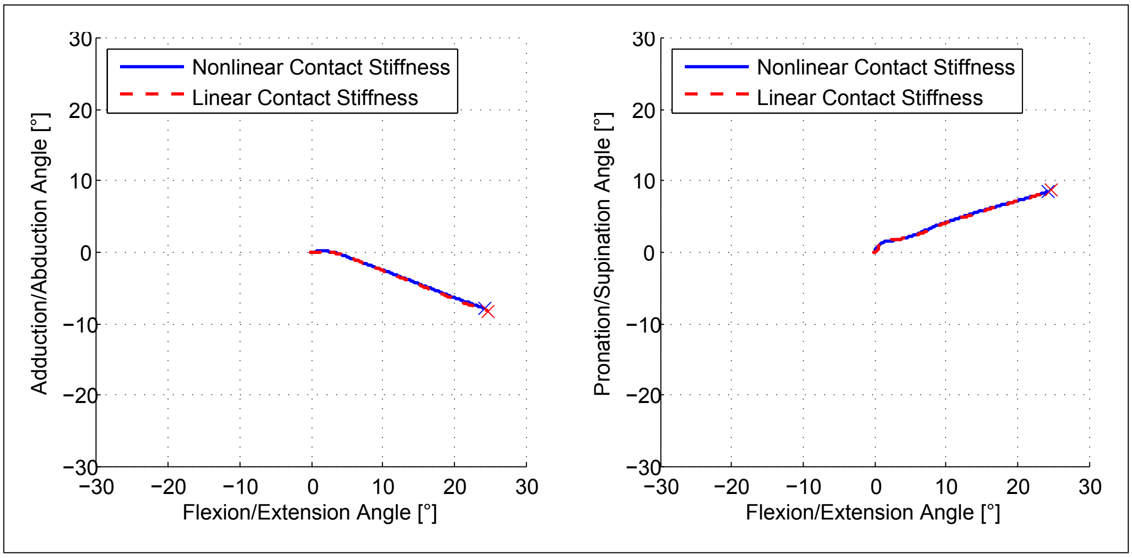

Figure 4.1.: Influence of the contact stiffness modelling approach on the joint kinematics

4.1.2. Ligament Stiffness

For testing the influence of the ligament stiffness, two simulations are conducted, with two and four times the original stiffness coefficient. All other parameters are kept unchanged, the contact stiffness is nonlinear. The resulting deviations of the joint state compared to the original ligament stiffness are displayed in table 4.2.

	$\overline{d_a}$ [°]	$d_a(0.5)$ [°]	$\overline{d_e}$ [mm]	$d_e(0.5)$ [mm]
Stiffness × 2	1.452	2.188	0.723	1.051
Stiffness × 4	3.358	4.613	1.682	2.235

Table 4.2.: Average and final distances of the joint orientation and position due to ligament stiffness variation

The results show that the both angular and euclidean distances are large compared to those caused by the variation of the contact stiffness modelling approach. Figure 4.2 shows the influence of the ligament stiffness on the joint kinematics. The range of motion decreases with increasing ligament stiffness. Besides the magnitude, the movement is not altered significantly, indicating that the ligaments indeed serve as delimiter of the motion.

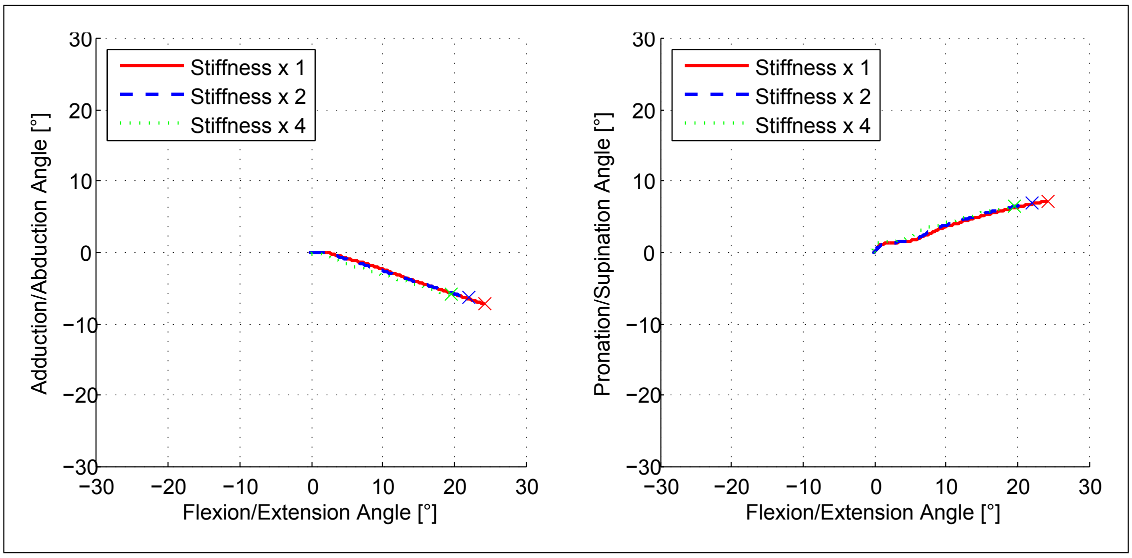

Figure 4.2.: Influence of the ligament stiffness on the joint kinematics

4.1.3. Friction

Friction causes tangential forces proportional to the normal force and the friction coefficient μ. In order to determine the influence of these tangential forces, simulations are conducted with $\mu = 0$, $\mu = 0.001$ and $\mu = 0.03$. These values correspond to those found in literature (see section 2.2.5). The resulting deviations with respect to $\mu = 0$ are displayed in table 4.3.

The differences are small compared to both the variation of the ligament and contact stiffness. Especially the difference between no and low friction is low. Even though the tangential force

	$\overline{d_a}$ [°]	$d_a(0.5)$ [°]	$\overline{d_e}$ [mm]	$d_e(0.5)$ [mm]
$\mu = 0.001$	0.014	0.012	0.011	0.003
$\mu = 0.03$	0.413	0.416	0.364	0.3512

Table 4.3.: Average and final distances of the joint orientation and position due to variation of the friction coefficient

is velocity dependent, slight deviations remain also after reaching the equilibrium position. In figure 4.3, the influence on the joint kinematics is depicted. Deviations are visible only between $\mu = 0$ and $\mu = 0.03$, indicating a very slight decrease of the range of motion if friction is considered.

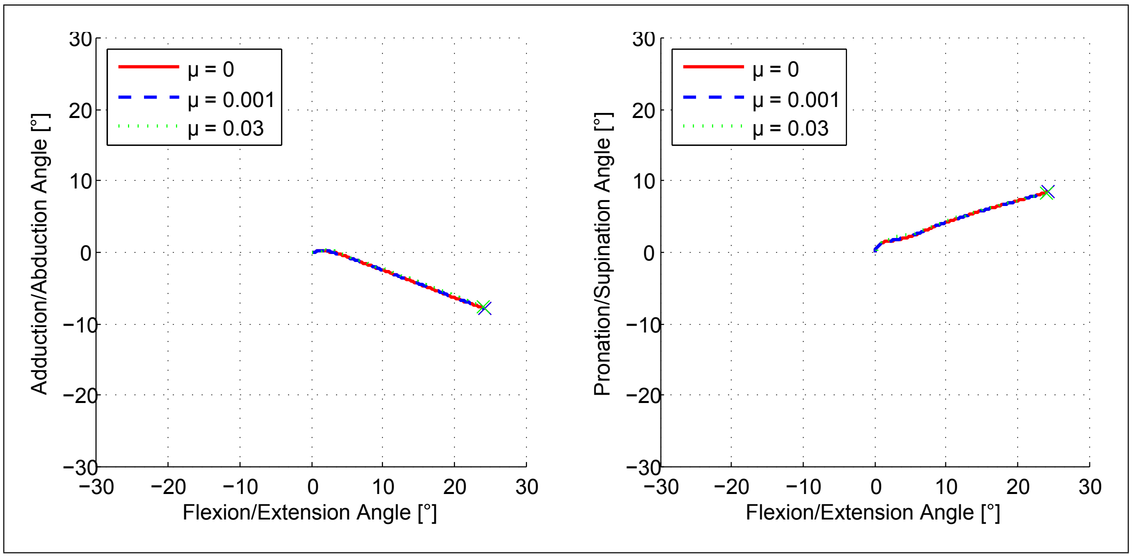

Figure 4.3.: Influence of friction on the joint kinematics

4.2. Single Muscle Activation

In order to determine the contribution of single muscles to CMC joint movement, each of them is activated in a separate simulation. The activation level $\alpha(t)$ is defined similar to formula 4.1 for the respective activated muscle. The simulations are conducted from $t = 0\,\mathrm{s}$ to $t = 0.5\,\mathrm{s}$. The contact is operated in the 2-pass-mode with nonlinear contact stiffness and the friction coefficient is set to zero. The results of the eight time integrations are depicted in figure 4.4.

In the present model, the AD, OP, APB and FPB are flexing muscles, and the EPL, EPB and APL are extending muscles. The EPL, EPB and FPB adduct, the OP, AD, APB and APL abduct the CMC joint. It is observed that the movements caused by the FPL and APL are very small. A probable reason is the initial strain in the muscles, which causes a reduction of the maximal force of the muscles. Both the OP and APB contribute to opposition movement, since the activation results in a combination of flexion and abduction. The rotational joint state at $t = 0.5\,\mathrm{s}$ is displayed in table 4.4 for quantitative comparison.

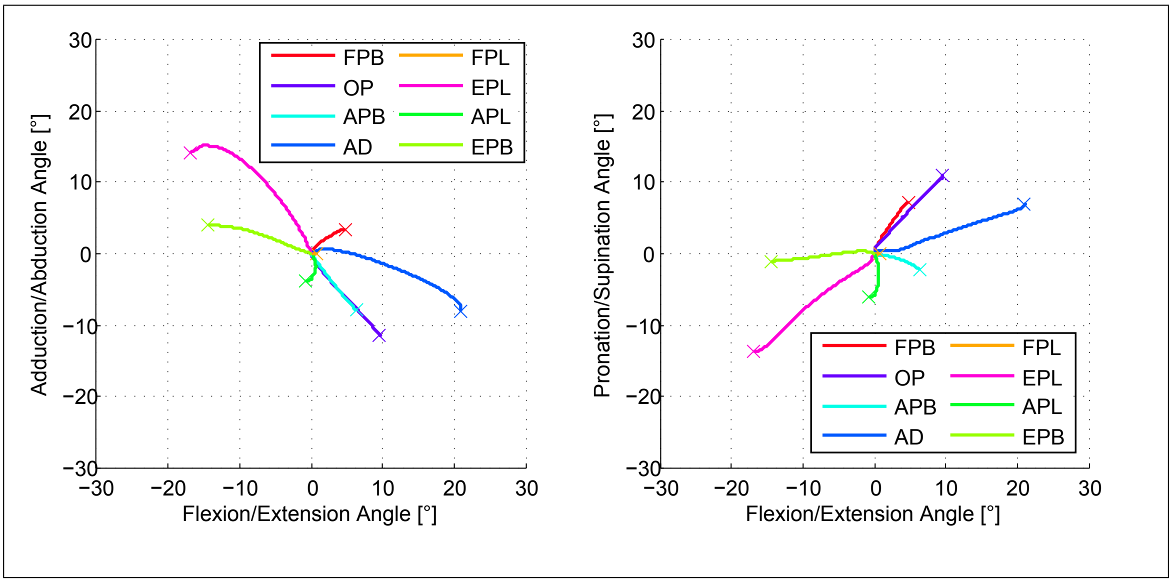

Figure 4.4.: Movements resulting from single muscle activation

	Flexion(+) / Extension(-) [°]	**Adduction(+) / Abduction(-) [°]**	**Pronation(+) / Supination(-) [°]**
FPB	4.75	3.37	7.24
OP	9.62	-11.52	10.98
APB	6.35	-7.92	-2.22
AD	20.85	-7.97	6.71
FPL	0.68	-0.1	-0.09
EPL	-16.83	14.2	-13.73
APL	-0.69	-3.74	-6.15
EPB	-14.54	4.09	-1.06

Table 4.4.: Final orientation of the first metacarpal bone after single muscle activation

It is observed that the AD is the most significant flexor and the EPL the most significant extensor. Largest abduction movement results from activating the OP and largest adduction movement from the EPL.

4.3. Selected Movements

In this section, two movements involving the activation of multiple muscles are simulated: The opposition and the circumduction. One of the most important combined movements is the opposition of the thumb. It is composed of a flexion, abduction and pronation movement and simulated by fully activating the APB and OP muscle (see section 2.1.3). Circumduction is a circular movement of the CMC joint and involves flexing, extending, abducting and adducting muscles. The simulation of circumduction is conducted by subsequently activating the EPB, EPL, AD, OP and APB. For both simulations, 2-pass-mode, nonlinear frictionless contact are selected. The opposition movement is simulated from $t = 0\,\mathrm{s}$ to $t = 0.5\,\mathrm{s}$, with $\alpha(t)$ as defined in formula 4.1 for the APB and OP. The circumduction movement is simulated from $t = 0\,\mathrm{s}$ to $t = 4.6\,\mathrm{s}$ and the activation level $\alpha_i(t)$ for each muscle is defined as follows:

$$\alpha_i(t) = \begin{cases} 0 & \text{for } 0 \leq t < t_i \\ 3.3 \cdot t & \text{for } t_i \leq t < t_i + 0.3 \\ 1 & \text{for } t_i + 0.3 \leq t < t_i + 1.1 \\ -3.3 \cdot t & \text{for } t_i + 1.1 \leq t < t_i + 1.4 \\ 0 & \text{for } t_i + 1.4 \leq t \end{cases} \tag{4.4}$$

For each muscle, a starting time t_i is defined:

$$t_i = 0.1 + i \cdot 0.7 \tag{4.5}$$

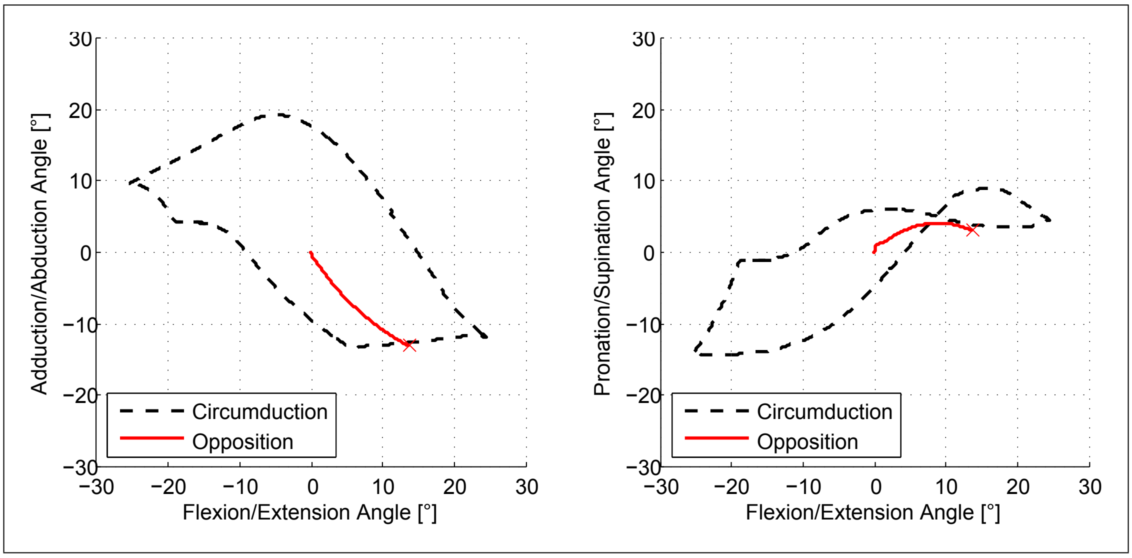

Figure 4.5.: Oppositon and circumduction movement, simulated by activating multiple muscles

The sequence of the muscle activation is EPB, EPL, AD, OP, APB and EPB. Both the sequence and the timings are determined empirically. Figure 4.5 depicts the results of both the opposition and circumduction movement. The opposition movement causes a flexion of $13.55\,°$, an abduction of $-13\,°$ and a pronation of $3.15\,°$ in the final position. The circumduction covers a range of $50.19\,°$ of flexion and extension, $32.75\,°$ of adduction and abduction and $23.31\,°$ of pronation and supination.

4.4. Range of Motion

The range of motion (RoM) is simulated by a combined activation of the strongest flexors, extensors, adductors and abductors. Since pronation and supination are not assumed to be actively controllable, they are excluded from this investigation. For full flexion, the AD, APB, FPL, OP and FPL are activated. Full extension is achieved by activating the activating the EPL, EPB and APL. APB, OP and APL are considered to be the main abductors and the EPL and FPB the main adductors. The respective activation levels $\alpha(t)$ are defined similar to formula 4.1. The results are depicted in a 3D view in figure 4.6. The flexion and extension is shown in ulnar view, the adduction and abduction in a dorsal view. For quantitative comparison, figure 4.7 shows the 2D plots of the results of all four time integrations.

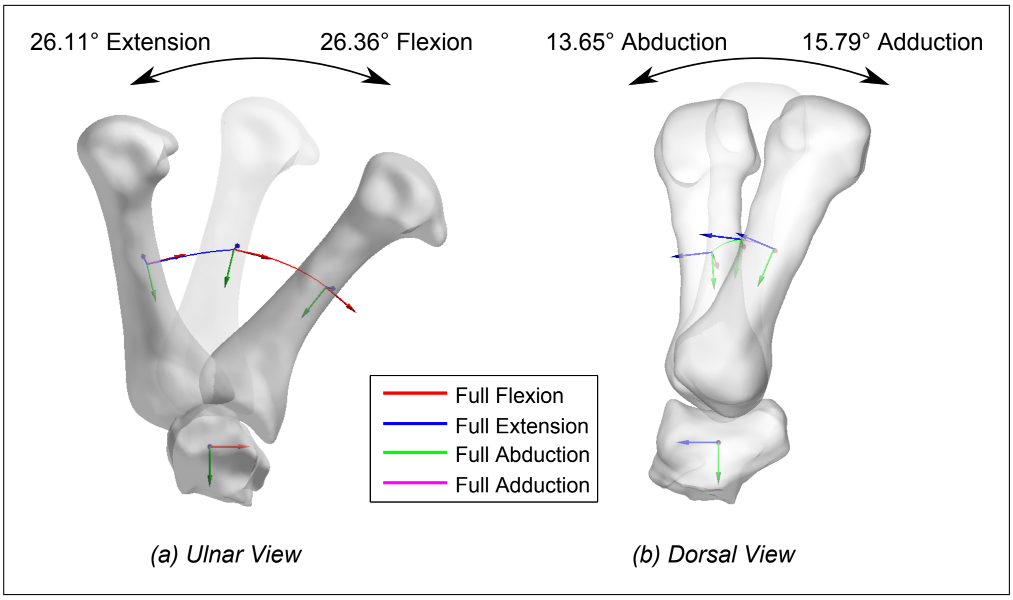

(a) Ulnar View

(b) Dorsal View

Figure 4.6.: Full flexion, extension, adduction and abduction movement, depicted in ulnar and dorsal view

It is observed that the activation of the muscles does not deliver movements solely in one anatomical direction. Full flexion is accompanied by abduction, which is similar to opposition, full extension by adduction, full abduction by flexion and full adduction by extension. Pronation and supination occur especially under full flexion and extension, respectively. The resulting range of motion for flexion and extension is $52.47\,°$, for adduction and abduction it amounts to $29.44\,°$.

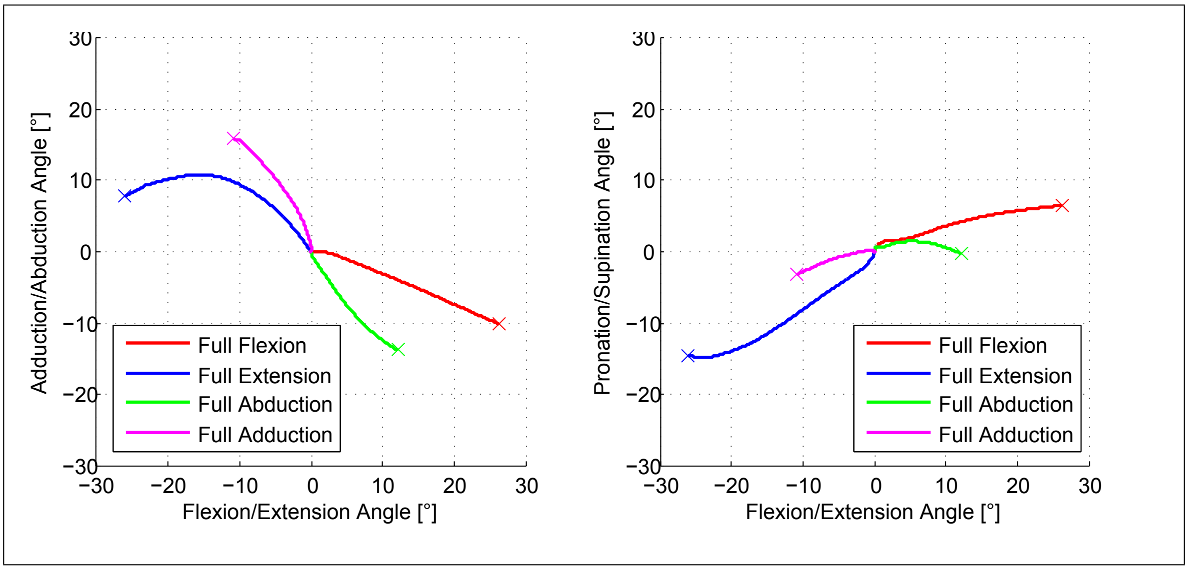

Figure 4.7.: Movements during full flexion, extension, adduction and abduction movement

	Flexion(+) / Extension(-) [°]	Adduction(+) / Abduction(-) [°]	Pronation(+) / Supination(-) [°]	RoM [°]
Full Flexion	26.36	-10.06	6.54	52.47
Full Extension	-26.11	7.77	-14.52	
Full Abduction	12.15	-13.65	-0.16	29.44
Full Adduction	-10.89	15.79	-3.14	

Table 4.5.: Final orientations of the first metacarpal bone after the activation of multiple muscles and the range of motion for flexion/extension and adduction/abduction movements

5. Discussion

A biomechanical model of the CMC joint was established including muscles, ligaments and articular contact. Simulations were conducted in time domain in order to determine the joint movement resulting from the activation of single or multiple muscles. In this chapter, the model of the CMC joint and the results from time integration are discussed. The kinematics of the first metacarpal are compared to studies on functional anatomy for this purpose. In the following, the approach of modelling a human joint based on its morphology for kinematic investigations is discussed, including sources of errors and possible methods of improvement.

5.1. Plausibility of the Joint Kinematics

The biomechanical model of the CMC joint is driven by forces from muscles, ligaments and articular contact. The force calculation of each force element is based on modelling approaches found in literature, hence, comparison of the output values of the force elements with literature is not considered sensible. However, the force laws are functions of deflections which have to stay within a physiological region. Since the deflection is calculated as the distance from a fixed proximal, to a moving distal attachment point, it is assumed that a plausible joint kinematics results in plausible magnitudes of forces exerted by the force elements.

In section 2.1.3, the functional anatomy of the CMC joint is explained briefly. Based on additional literature, the functionality of the muscles in anatomical studies and in the present model are compared.

The APB and OP are radial muscles and combined to conduct opposition movements, consisting of flexion, abduction and pronation. The movement resulting from fully activating the APB and OP shows that the movement is qualitatively well represented by the model. Single muscle activation leads to movements that are consistent with the findings of Brand and Hollister (1999), Kapandji (2006) and Kaufman et al. (1999). Both muscles are flexors and abductors and the OP is generally stronger than the APB. Comparing the moment potential arms from Kaufman et al. (1999), computed by multiplying the muscle moment arms with the respective PCSA, it is observed that the APB is regarded as a weaker flexor than the OP. According to Kaufman et al. (1999), the FPB is a flexor and abductor, similar to the OP and APB. Kapandji (2006) agrees that the FPB has similar functionality to the remaining radial thumb moving muscles. The modelled movement resulting form activating the FPB shows that it serves as a flexor, but causes adduction rather than abduction movement.

The AD is regarded as the strongest adducting and flexing muscle by Kaufman et al. (1999). In the present model, full activation of the AD leads to a strong flexion but abduction instead of adduction. A possible explanation is delivered by Kapandji (2006), who mentions that the AD has different tasks depending on the current joint state, such as an abduction movement in an adducted posture. Hence, if the starting position of the simulation represents an adducted position, the AD might cause an abduction movement.

According to Kaufman et al. (1999), the FPL is a strong flexor, but a weak abductor. Brand and Hollister (1999) states that the FPL influences the DIP joint flexion and has only little influence on the CMC joint. Activating the FPL in the present model leads to a small flexion and abduction movement. Even though small movements would agree with Brand and Hollister (1999), they are more likely a result of the large initial strain that is necessary for satisfying equilibrium conditions of the joint. Except for the magnitude, the movement caused by the FPL is consistent with the findings of Kaufman et al. (1999).

The EPL extends and adducts the first metacarpal bone according to Brand and Hollister (1999) and Kaufman et al. (1999). Kapandji (2006) states a rotational movement of the first metacarpal in ulnar and dorsal direction after activating the EPL, which is similar to extension and adduction. The modelled movement agrees with these findings.

Brand and Hollister (1999) considers the APL to be a very strong muscle capable of extension and abduction. Agreement is found by Kaufman et al. (1999). Kapandji (2006) also mentions the contribution of the APL to opposition movement. In the present model, the activation of the APL causes only a small abduction and extension movement. Moreover, the functionality of the muscle changes from a flexor to an extensor throughout the movement. Similar to the FPL, the low magnitude of the movement is likely to be caused by the initial strain required for satisfying the equilibrium conditions.

According to Kaufman et al. (1999) and Kapandji (2006), the EPB abducts and extends the CMC joint. The modelled movement after activating the EPB results in an extension and slight adduction movement. Hence, the EPB movement is not consistent with the findings of Kaufman et al. (1999) and Kapandji (2006) regarding the abduction and adduction movement.

	Flexion/Extension Range [°]	**Adduction/Abduction Range [°]**
Kapandji (2006)	50-70	40-60
Li and Tang (2007)	63.4 ± 9.4	47.8 ± 6.3
CMC Joint Model	52.47	29.44

Table 5.1.: Comparison of the range of motion of the present model to values found in literature

Besides single muscle activation, the range of motion of the present model resulting from the activation of multiple muscles can be compared with anatomical studies. Kapandji (2006) describes the range of motion for both flexion/extension and abduction/adduction. The maximum flexion and extension is stated to be within the boundaries of $20-25\,^\circ$ and $30-45\,^\circ$ respectively, resulting in a range of $50-70\,^\circ$. Maximum adduction and abduction movements are $15-25\,^\circ$ and $25-35\,^\circ$ respectively, resulting in a range of $40-60\,^\circ$. Li and Tang (2007) measured the range of motion within circumduction movement. The ranges of motion resulting from the measurements are $63.4\pm9.4\,^\circ$ for flexion and extension and $47.8\pm6.3\,^\circ$ for adduction and abduction. The values represent the means and standard deviations and are consistent with the findings of Kapandji (2006). Comparison to the range of motion of the present model shows that the magnitudes of both the flexion and extension and the adduction and abduction movements are low. The range of motion regarding the flexion and extension movement is just within the boundaries defined by Kapandji (2006), the adduction and abduction range is far lower, as shown in table 5.1.

In summary, the present model of the CMC joint allows for kinematic simulations based on contacting surfaces, but is limited regarding the accuracy of the predicted movements. The movements resulting from single activation of the muscles qualitatively agree with the literature for the OP, APB and EPL. The APL and FPL both cause a plausible, but small movement. The functionality of the AD is controversial. In the present model, flexion and abduction result from its activation. The FPB and EPB show good qualitative agreement with the anatomical studies regarding flexion and extension, whereas the addcution and abduction movement is predicted in the respective opposite direction. The range of motion is consistent with literature for flexion/extension movements, but too small for the adduction/abduction movements.

5.2. Error Sources and possible Improvements

The previous section shows that the movements predicted by the present model are only partly consistent with the findings anatomical studies. In order to obtain better results, it is necessary to determine possible sources of errors and potential methods of improvement. The errors are likely to be found in the process of modelling the tissue geometry and its mechanical properties.

Except for the cartilage, all tissues are modelled based on literature. Since the aim of most biomechanical investigations is to obtain a general model of the respective tissues, the values are averaged to a certain extent. As a result, the present model consists of subject specific articular surfaces, but averaged muscle and ligament attachment sites and architectures. Since the present model is based on point-to-point force elements for muscles and ligaments, these attachment sites have a significant impact on joint kinematics. Especially the coordinates used to determine the muscle lines of action are regarded as a major error source. The coordinates are aligned to best fit experimental data, which might imply that the anatomical correspondence is lost. Moreover, the definition of the coordinate system yields several uncertainties due to the irregular shape of the bones. Another error source are the MRI images. Even though they serve as a practical means for in-vivo measurement of the surfaces, low resolutions and artifacts cause difficulties during the process of segmentation and possibly lead to inaccuracies. The comparably low quality of the MRI images is a result of the sequence that is necessary for identifying the cartilage. In this sequence, the MR-signal is very weak, resulting in a low signal to noise ratio. Another error source results from the pose estimation. The accuracy of the pose estimation can be determined only by visual inspection and the precision is low.

Besides the mentioned geometrical aspects, also mechanical aspects are considered to be the source of errors. The parameters of the individual tissues are based on values found in different publications. Since the conditions of measurements are likely to vary, it is probable that these values imply inaccuracies for the model.

In order to improve the present model, the source of the quantitative data has to be changed. Errors regarding the geometry could be eliminated by using additional MRI images to quantitatively detect ligaments, muscle and cartilage. For this purpose, it is probable that several different techniques and sequences have to be tested to obtain the image with the desired contrast. For instance, proton density weighted images could allow for the detection of ligaments. Moreover, contrast agent might be used to identify both the proximal and distal cartilage surface. In order to improve the accuracy and precision resulting from the pose estimation, it is suggested to take MRI images with similar contrasts for both the reference and the detail image.

Since the ranges of parameters for modelling the material properties of the tissues are generally large (e.g. cartilage stiffness), an optimization of the model for the determination of these parameters is considered sensible. The optimization of the model is possible either based on MRI or experimental data. Using MRI images of different postures, the parameters of the tissues could be adapted in a manner that all postures are reached with minimal translational and angular distance. Besides MRI, also EMG in combination with motion tracking techniques could serve as a means of optimization. Based on this data, the parameters of the model could be adapted to minimize the distance between the measured and predicted pose with activation levels as recorded from the EMG.

5.3. Applicability of MBS with PCM to Kinematic Investigations

The aim of this thesis was to develop a biomechanical model of a human joint accounting for the geometry of the articulating surface, muscles and ligaments. This model should serve the purpose of conducting kinematic simulations with increased accuracy compared to models using fixed rotational axes. In this section, the applicability of MBS in combination with PCM for kinematic simulations is discussed. Advantages and disadvantages of the application of this method in the field of biomechanics are elucidated in the following.

5.3.1. Advantages

Joint movements are typically modelled by assuming fixed axes of rotation. This approach assumes idealized joints, similar to those found in technical applications. The axes of rotation is either approximated from the bone geometry or optimized to experimental data. Especially the approach of fitting axes to experimental data allows for a very accurate prediction prediction of the movements. However, the morphology of the joint is not considered. As a result, the movements are valid only for the postures involved in the optimization process. Effects caused by stabilizing tissues, such as the dependence of lateral motion on the flexion angle due to ligament laxity, are not accounted for. The main advantage of modelling the joint based on its actual morphology is that all physiological effects are involved automatically if the level of detail is sufficient. Moreover, the resulting model allows for the prediction of movements after changes in the morphology, such as the number of stabilizing ligaments.

A MBS is a simple means to incorporate all components of a joint in a biomechanical model. Since the MBS is based on rigid bodies with body fixed coordinate systems, the joint kinematics can be accessed directly. Forces resulting from the articular contact, muscles and ligaments are modelled by force elements, which are defined by a simple force law. Assembling these simple force elements yields a model capable of performing complex movements. The computational time of a MBS is moderate, especially compared with FEA.

PCM yields a simple, robust and fast method of incorporating contact in any MBS. The required computational time is minimized due to the use of bounding volumes and the elastic foundation theory. The contact geometry is represented by polygonal surfaces, which are easily handled and processed. Several additional outputs of PCM provide information about the contact geometry, kinematics and prevailing pressures.

The individual design of the force elements allows for comparing the results of experiments to simulations. For instance, electromyography (EMG) could be used to determine the force activation level, serving as an input for the muscle force element.

5.3.2. Disadvantages

In order to determine movements caused by the contact of articulating surfaces, it is necessary to calculate forces that restrict the surfaces from penetrating each other. Additionally, both the stability and movement of the joint are influenced by the forces exerted by ligaments and muscles. As a result, dynamics has to be incorporated in the simulation, even though only the kinematics of the joint are of interest. This implies that inertial properties and force laws have to be defined for each component considered in the model.

Hence, the process of modelling a joint including all morphological components requires profound knowledge about material properties and geometry. Since ligaments, muscles and articular surface are different for each joint, it is necessary to determine the parameters individually. Modelling of both the material properties and the geometry yields a huge effort, including extensive literature investigation. Using data from literature yields several uncertainties, since the circumstances of the respective studies are often unknown.

PCM is a fast and robust means of contact modelling, but simplifies both the contact geometry and the contact force calculation. Polygonal surfaces are easy to handle but always contain spikes and edges depending on the level of discretization. The contact forces calculated from PCM are based on the elastic foundation theory which assumes penetrating surfaces and neglects shear forces within the bodies. Hence, the contact pressure and geometry computed by PCM only serve as approximations.

5.3.3. Conclusion

Modelling a human finger joint based on its actual morphology yields several advantages and novel possibilities. For instance, the influence of single tissues on the joint movement and stability can be investigated. The model is composed of several simple components and driven by forces exerted by the muscles. This allows for observing the joint movement for certain activation levels of the muscles. However, the process of modelling requires profound knowledge about each tissue involved, regarding both its geometry and material properties. In comparison to a model based on fixed rotational axes, a model based on the contact surfaces yields a more complex and highly nonlinear system which can be solved only by numerical integration.

It can be concluded that the approach of modelling a human joint based on contacting surfaces serves as a sensible means for conducting kinematic simulations, but only in case quantitative analysis are available for all tissues contained in the model. This involves geometrical aspects such as ligament and muscle attachment sites, tissue architecture and mechanical aspects such as elastic and time dependent behaviour.

6. Summary and Outlook

The movement of human joints is often approximated by fixed rotational axes. This approximation leads to an error, which was found to be large especially for the CMC joint of the thumb. In this thesis, a new approach of simulating the kinematics of a human finger joint based on contacting surfaces was proposed. The CMC joint was modelled as a multi body system in SIMPACK, consisting of one fixed and one unconstrained bone. The movement of the joint is determined by the forces exerted by the contacting articular surfaces, eight muscles and seven ligaments.

In order to obtain the contact geometry of the articulating bones, polygonal surfaces were created based on MRI images. The surfaces were extracted by applying the marching cubes algorithm to the smoothened volume of the manually segmented metacarpal and trapezium bone. Further surface processing steps involved the correction regarding the accuracy to the segmented data and Laplacian flow smoothing. The contact geometry was subsequently obtained by dilating the bone surfaces with the cartilage thickness estimated from the MRI images. For the implementation in SIMPACK, coordinate systems were calculated based on the surface geometry for both of the articulating bones. The contact forces are computed using a modified version of PCM, which accounts for the mechanical properties of articular cartilage. PCM assumes undeformable surfaces and delivers forces and moments depending on their penetration in contact. Even though articular cartilage is a very complex material, literature investigation showed that it is appropriate to model it as linear elastic, homogeneous and isotropic for fast loading and unloading cycles. Since cartilage is very compliant, PCM was adapted to account for geometric nonlinearities. The friction between the surfaces was modelled using Coulomb's law of friction.

The muscles moving the CMC joint were modelled as point-to-point elements, which exert forces along the connection line between a proximal and distal attachment point. The respective coordinates were adopted from a study which aimed at finding muscle attachment locations to best fit experimental data. In order to account for the large insertion areas of the AD, it was modelled with four point-to-point elements. Each muscle exerts an active force if activated and a passive force if stretched. The active force is computed based on the Hill model, the passive force is exerted similarly to a nonlinear spring with exponential characteristics. Since the architecture of each muscle is different, the architecture index, the muscle optimum length and the PCSA was incorporated in the calculations.

Similar to the muscles, the ligaments were modelled as point-to-point elements. The attachment coordinates were determined based on anatomical studies which provided the attachment areas of seven ligaments. Since the sAOL and POL attachment area is relatively large, they were modelled with two elements each. Each ligament exerts tensile forces similar to a nonlinear spring with quadratic characteristics. The ligament architecture is accounted for by scaling the force with the respective CSA.

The whole model, consisting of two rigid bodies and 21 user defined force elements was assembled in SIMPACK. In order to obtain a static equilibrium position of the joint, the initial forces of the muscles and ligaments compensating the force resulting from the contact in reference position had to be determined. Conducting a constrained linear optimization allowed for the calculation of initial strains and lengths of muscles and ligaments, respectively. Finding a static equilibrium position in SIMPACK eliminated the remaining accelerations due to residual forces and moments. The static equilibrium position deviated from the reference posture but represented a physiological position.

Based on this model, simulations of joint movements were conducted in time domain by numerically solving a system of ordinary differential equations using SIMPACK. The model was controlled by eight time dependent functions representing the activation levels of the muscles. Parametric influences were determined by variation of the contact and ligament stiffness and the friction. It was shown that differences between the linear and nonlinear modelling approach of the contact stiffness is small, resulting in final deviations of $0.60\,^\circ$ and $0.44\,\mathrm{mm}$ of the metacarpal coordinate system. Similar results were obtained for varying the friction from $\mu = 0$ to $\mu = 0.03$, where the final deviations amount to $0.60\,^\circ$ and $0.35\,\mathrm{mm}$. Assuming four times the original ligament stiffness lead to considerably high deviations of $4.61\,^\circ$ and $2.23\,\mathrm{mm}$. Regarding the joint kinematics, it was concluded that a higher contact stiffness, ligament stiffness or friction delimit the joint movement in the present model.

In order to determine the plausibility of the movements of the CMC joint model, it was compared to studies in the field of functional anatomy. Activating single muscles showed good qualitative agreement for the OP, APB and EPL. The APL and FPL lead to movements in a plausible direction, but with a smaller magnitude than expected. The anatomical functionality of the AD is controversial. In the present model, activation of the AD produced an abduction and flexion movement. The FPB and EPB are consistent with literature only regarding flexion and extension movements. The range of motion of the model, resulting from multi muscle activation was $52.477\,^\circ$ for flexion/extension and $29.44\,^\circ$ for adduction/abduction. Comparison to literature showed that the range of motion is consistent only for the flexion/extension movements.

Even though not all movements were consistent with literature, it was shown that the approach of using a multi body simulation software in combination with PCM for conducting kinematic investigations of human finger joints leads to physiological results. Since the model is based on the actual morphology of the joint, it is capable of predicting the influence of single tissues contributing to joint movement and stability, which makes it more versatile than conventional models based on fixed axes. In contrast to FEA, MBS was found to be a simple and fast method for conducting kinematic simulations of human joints. A major drawback of this approach is the extensive anatomical knowledge required to model the individual joint morphology appropriately. This involves mainly the muscle and ligament attachment locations, which were also considered to be the most probable error source of the present model. Hence, improvements of the model should focus on the quality of the data it is built upon. Additional MRI images which allow for the identification of the ligaments and tendons would lead to a more consistent and accurate model of the joint. Alternatively, the geometrical or mechanical parameters of the model could be optimized to best fit a set of given postures.

An improved version of the present model could help to reveal the advantages of the human joints in comparison with idealized technical joints. This knowledge could subsequently be used to enhance anthropomorphic robotic hands, such as the hand of the DLR hand arm system. Due to its anatomical correspondence, a biomechanical model based on the actual joint morphology including contacting surfaces might also be applied in medical fields, such as presurgical investigations or endoprosthetics.

Bibliography

An, K.N., Chao, E.Y., Cooney III, W.P. and Linscheid, R.L., 1979. Normative model of human hand for biomechanical analysis. *Journal of Biomechanics*, 12 (10), pp.775-788.

An, K.-N. et al., 1990. Pressure distribution on articular surfaces: Application to joint stability evaluation. *Journal of Biomechanics*, 23 (10), pp.1013-1020.

Bartsch, H.-J., 2007. *Kleine Formelsammlung Mathematik* . Vierte Auflage. München: Carl Hanser Verlag.

Bei, Y. and Fregly, B. J., 2004. Multibody dynamic simulation of knee contact mechanics. *Medical Engineering & Physics*, 26 (9), pp.777-789.

Bell, J.S., Winlove, C.P., Smith, C.W. and Dehghani, H., 2009. Modeling the steady-state deformation of the solid phase of articular cartilage. *Biomaterials*, 30 (31), pp.6394-6401.

Belton, D., 2008. Improving and Extending the Information on Principal Component Analysis for Local Neighborhoods in 3D Point Clouds. In: *International Society for Photogrammetry and Remote Sensing*. Beijing, China 3-11 july 2008.

Bender, M und Brill, M., 2006. *Computergrafik*. München: Carl Hanser Verlag.

Blankevoort, L., Kuiper, J.H., Huiskes, R. and Grootenboer, H.J., 1991. Articular contact in a three-dimensional model of the knee. *Journal of Biomechanics*, 24 (11), pp.1019-1031.

Brand, P. W. and Hollister, A. M., 1999. *Clinical Mechanics of the Hand* . Third Edition. Missouri: Mosby.

Brook, N., Mizrahi, J., Shoham, M. and Dayan, J., 1995. A biomechanical model of index finger dynamics. *Medical Engineering & Physics*, 17 (1), pp.54-63.

Butterfass, J. et al., 2004. Design and experiences with "DLR" hand "II". *Proceedings of the World Automation Congress*, 15, pp.105-110.

Grebenstein, M. et al. 2011. The DLR Hand Arm System. In: *IEEE International Conference on Robotics and Automation*. Shanghai, China 9-13 May 2011.

Charnley, J.,1960. The lubrication of animal joints in relation to surgical reconstruction by arthroplasty. *Annals of the Rheumatic Diseases*, 19 (12), pp.10-19.

Chen, S. S. et al., 2001. Depth-dependent compressive properties of normal aged human femoral head articular cartilage: relationship to fixed charge density. *Osteoarthritis and Cartilage*, 9 (6), pp.561-569.

Chen, A. C., Bae, W. C., Schinagl, R. M. and Sah, R. L., 2001. Depth- and strain-dependent mechanical and electromechanical properties of full-thickness bovine articular cartilage in confined compression. *Journal of biomechanics*, 32 (1), pp.1-12.

Clarke, I. C., Contini, R. and Kenedi, R. M., 1975. Friction and wear studies of articular cartilage: A scanning electron microscope study. *Journal of Lubrication Technology*, 97, pp.358-368.

Crowninshield, R. and Johnson, R. J., 1976. An analytical model of the knee. *Journal of Biomechanics*, 9 (6), pp.397-405.

Eberly, D., 2008. *Least Squares Fitting of Data* [online] Available at: <http://www.geometrictools.com/Documentation/LeastSquaresFitting.pdf> [Accessed 13 July 2011].

Fung, Y.-C. B., 1987. Mechanics of Soft Tissues. In: R. Skalak and S. Chien, eds. 1987. *Handbook of Bioengineering*. USA: McGraw-Hill, pp.1.1-2.1.

Fung, Y.-C. B., 1993. *Biomechanics*. New York: Springer.

Giurintano, D. J. et al., 1995. A virtual five-link model of the thumb. *Medical Engineering & Physics*, 17 (4), pp.297-303.

Goreham-Voss, C. M. et al., 2010. Cross-shear implementation in sliding-distance-coupled finite element analysis of wear in metal-on-polyethylene total joint arthroplasty: Intervertebral total disc replacement as an illustrative application. *Journal of Biomechanics*, 43 (9), pp.1674-1681.

Guo, Y., Zhang, X. and Chen, W., 2009. Three-Dimensional Finite Element Simulation of Total Knee Joint in Gait Cycle. *Acta Mechanica Solida Sinica*, 22 (4), pp.347-351.

Handels, H., 2009. *Medizinische Bildverarbeitung*. Zweite Edition. Wiesbaden: Vieweg+Teubner.

Harner, C. D. et al., 1995. Comparative study of the size and shape of human anterior and posterior cruciate ligaments. *Journal of Orthopaedic Research*, 13 (3), pp.429-434.

Har-Peled, S., 2011. *Geometric Approximation Algorithms*. Rhode Island: American Mathematical Society.

Hibbeler, R. C., 2006. *Technische Mechanik 3*. Zehnte Auflage. München: Pearson Education Deutschland.

Hillenbrand, U., 2008. Pose Clustering From Stereo Data. In: L. Iocchi and G. Sorrenti, eds. 2008. *VISAPP (Workshop on Robot Perception)*. INSTICC, pp.23-32.

Hippmann, G., 2004. *Modellierung von Kontakten komplex geformter Körper in der Mehrkörperdynamik*. Ph. D. Technische Universität Wien.

Hirokawa, S. and Tsuruno, R., 1997. Hyper-elastic model analysis of anterior cruciate ligament. *Medical Engineering & Physics*, 19 (7), pp.637-651.

Hori, R. Y. and Mockros, L. F., 1976. Indentation tests of human articular cartilage. *Journal of Biomechanics* , 9 (4), pp.259-268.

Imaeda, T., An, K.-N., Cooney, W. P. and Linscheid, R., 1993. Anatomy of trapeziometacarpal ligaments. *The Journal of Hand Surgery*, 18 (2), pp.226-231.

Jacobson, M. D. et al., 1992. Architectural design of the human intrinsic hand muscles. *The Journal of Hand Surgery*, 17 (5), pp.804-809.

Johnson, K. L., 1985. *Contact Mechanics*. Cambridge: Cambridge University Press.

Kapandji, I. A., 2006. *Funktionelle Anatomie der Gelenke*. Stuttgart: Thieme.

Kaufman, K. R., An, K.-N., Litchy, W.J. and Chao E. Y. S., 1991. Physiological prediction of muscle forces - I. Theoretical formulation. *Neuroscience*, 40 (3), pp.781-792.

Kaufman, K. R. et al., 1999. In-vivo function of the thumb muscles. *Clinical Biomechanics*, 14 (2), pp.141-150.

Koebke, J., 1983. A biomechanical and morphological analysis of human hand joints. *Advances in anatomy, embryology, and cell biology*, 80, pp.1-85.

Kuczynski, K., 1974. Carpometacarpal joint of the human thumb. *Journal of Anatomy*, 118 (1), pp.119-126.

Landon, R. L., Hast, M. W. and Piazza, S. J., 2009. Robust contact modeling using trimmed NURBS surfaces for dynamic simulations of articular contact. *Computer Methods in Applied Mechanics and Engineering*, 198 (30-32), pp. 2339-2346.

Li, Z.-M. and Tang, J., 2007. Coordination of thumb joints during opposition. *Journal of Biomechanics*, 40 (3), pp.502-510.

Li, G., Sakamoto, M. and Chao, E. Y. S., 1997. A comparison of different methods in predicting static pressure distribution in articulating joints. *Journal of Biomechanics*, 30 (6), pp.635-638.

Lieber, R. L. et al., 1992. Architecture of selected muscles of the arm and forearm: Anatomy and implications for tendon transfer. *The Journal of Hand Surgery*, 17 (5), pp.787-798.

Lin, Y.-C., Haftka, R. T., Queipo, N. V. and Fregly, B. J., 2010. Surrogate articular contact models for computationally efficient multibody dynamic simulations. *Medical Engineering & Physics*, 32 (6), pp.584-594.

Livnat, Y., Parker, S. G. and Johnson, C. R., 2000. Fast Isosurface Extraction Methods for Large Image Data Sets. In: I. N. Bankman ed. 2000. *Handbook of medical imaging*. San Diago: Academic Press, pp.731-745.

Madenci, E. and Guven, I., 2006. *The Finite Element Method and Applications in Engineerig using ANSYS* . New York: Springer Science+Business Media.

Magid, E., Soldea, O. and Rivlin, E., 2007. A Comparison of Gaussian and mean curvature estimation methods on triangular meshes of range image data. *Computer Vision and Image Understanding*, 107(3), pp.139-159.

Mansour, J. M., 2009. Biomechanics of Cartilage. In: C. A. Oatis, ed. 2009. *Kinesiology*. Philadelphia: Lippincott Williams & Wilkins, pp.69-84.

Martin, R. B., 1998. *Skeletal Tissue Mechanics*. New York: Springer.

McMahon, T. A., 1987. Muscle Mechanics. In: R. Skalak and S. Chien, eds. 1987. *Handbook of Bioengineering*. USA: McGraw-Hill, pp.7.1-8.1.

Mow, V. C. and Mak, A. F., 1987. Lubrication of Diarthrodial Joints. In: R. Skalak and S. Chien, eds. 1987. *Handbook of Bioengineering*. USA: McGraw-Hill, pp.5.1-6.1.

Nanno, M. et al., 2006. Three-Dimensional Analysis of the Ligamentous Attachments of the First Carpometacarpal Joint. *The Journal of Hand Surgery*, 31 (7), pp.1160-1170.

Peña, E., Calvo, B., Martínez, M. A. and Doblaré, M., 2007. An anisotropic visco-hyperelastic model for ligaments at finite strains: Formulation and computational aspects. *International Journal of Solids and Structures*, 44 (3-4), pp.760-778.

Peña, E., Calvo, B., Martínez, M. A. and Doblaré, M., 2006. A three-dimensional finite element analysis of the combined behavior of ligaments and menisci in the healthy human knee joint. *Journal of Biomechanics*, 39 (9), pp.1686-1701.

Rill, G. and Schaeffer, T., 2010. *Grundlagen und Methodik der Mehrkörpersimulation*. Wiesbaden: Vieweg+Teubner.

Robertson, D. and Gordon E., 2004. *Research methods in biomechanics*. Campaign: Human Kinetics.

Sancho-Bru, J. L., Pérez-González, A., Vergara-Monedero, M. and Giurintano, D., 2001. A 3-D dynamic model of human finger for studying free movements. *Journal of Biomechanics*, 34 (11), pp.1491-1500.

Schünke, M., 2005. *Prometheus - LernAtlas der Anatomie*. Stuttgart: Thieme.

Slabaugh, G. G., 1999. *Computing Euler angles from a rotation matrix* [online] Available at: <http://www.gregslabaugh.name/publications/euler.pdf> [Accessed 20 July 2011].

Smutz, P. et al., 1998. Mechanical advantage of the thumb muscles. *Journal of Biomechanics*, 31 (6), pp. 565-570.

Stillfried, G. and van der Smagt, P., 2010. Movement model of a human hand based on magnetic resonance imaging (MRI). In: *International Conference on Applied Bionics and Biomechanics (ICABB)*. Venice, Italy 14-16 October 2010.

Stillfried, G., Hillenbrand, U., Settles, M and van der Smagt, P., (in press). MRI-based skeletal hand movement model. To be published in: R. Balasubramanian and V. Santos, eds (in press). *The Human Hand - a Source of Inspiration for Robotic Hands (tentative title)*. Springer Tracts on Advanced Robotics.

Stillfried, G., 2009. *Kinematische Simulation einer menschlichen Hand*. Master Thesis. Technische Universität München.

Tan, J. et al., 2011. In Vivo Length and Changes of Ligaments Stabilizing the Thumb Carpometacarpal Joint. *The Journal of Hand Surgery*, 36 (3), pp.420-427.

Uhlmann, K., 1996. *Lehrbuch der Anatomie des Bewegungsapparates*. Wiesbaden: Quelle & Meyer.

Valero-Cuevas, F. J., Johanson, M. E. and Towles, J. D., 2003. Towards a realistic biomechanical model of the thumb: the choice of kinematic description may be more critical than the solution method or the variability/uncertainty of musculoskeletal parameters. *Journal of Biomechanics*, 36 (7), pp.1019-1030.

Verdonck, P., 2009. *Advances in Biomedical Engineering*. Amsterdam: Elsevier.

Viidik, A, 1987. Properties of Tendons and Ligaments. In: R. Skalak and S. Chien, eds. 1987. *Handbook of Bioengineering*. USA: McGraw-Hill, pp.6.1-7.1.

Wang, J. L., Parnianpour, M., Shirazi-Adl, A. and Engin, A. E., 1997. Failure criterion of collagen fiber: Viscoelastic behavior simulated by using load control data. *Theoretical and Applied Fracture Mechanics*, 27 (1), pp.1-12.

Weishaupt, D., Köchli, V. D. und Marincek, B., 2009. *Wie funktioniert MRI?*. Sechste Edition. Heidelberg: Springer Verlag.

Woittiez, R. D., Huijing, P. A. and Rozendal, R. H., 1983. Influence of muscle architecture on the length-force diagram. *Pflügers Archiv European Journal of Physiology*, 397 (73-74), pp.73-74.

Woittiez, R. D., Huijing, P. A., Boom, H. B. K. and Rozendal, R. H., 1984. A three-dimensional muscle model: A quantified relation between form and function of skeletal muscles. *Journal of Morphology*, 182 (1), pp.95-113.

Woo, S. L. Y., Mow, V. C. and Lai, W. M., 1987. Biomechanical Properties of Articular Cartilage. In: R. Skalak and S. Chien, eds. 1987. *Handbook of Bioengineering*. USA: McGraw-Hill, pp.4.1-5.1.

Wriggers, P., 2002. *Computational Contact Mechanics*. West Sussex: John Wiley Sons.

Wu, G. et al., 2005. ISB recommendation on definitions of joint coordinate systems of various joints for the reporting of human joint motion - Part II: shoulder, elbow, wrist and hand. *Journal of Biomechanics*, 38(5), pp.981-992.

Wu, Z. et al., 2009. Modeling of the muscle/tendon excursions and moment arms in the thumb using the commercial software anybody. *Journal of Biomechanics*, 42 (3), pp.383-388.

Zhang, Y. and Hamza, A. B., 2006. Vertex-Based Anisotropic Smoothing of 3D Mesh Data. In: *Canadian Conference on Electrical and Computer Engineering*. Ottawa, Canada 7-10 May 2006.

Zienkiewicz, O. C., Taylor, R. L. and Zhu, J. Z., 2005. *The Finite Element Method: It's basis and Fundamentals*. Sixth Edition. Great Britain: Elsevier.

List of Figures

List of Tables

List of Abbreviations

1D	One-dimensional
2D	Two-dimensional
3D	Three-dimensional
AP	Adductor pollicis
APB	Abductor pollicis brevis
APL	Abductor pollicis longus
CMC	Carpometacarpal (joint)
CSA	Cross sectional area
dAOL	Deep anterior oblique ligament
DI	First interosseus dorsalis
dIML	Dorsal first intermetacarpal ligament
DLR	Deutsches Zentrum für Luft- und Raumfahrt
DoF	Degrees of freedom
DRL	Dorsoradial ligament
EMG	Electromyography
EPB	Extensor pollicis brevis
EPL	Extensor pollicis longus
FE	Force element
FEA	Finite element analysis
FPB	Flexor pollicis brevis
FPL	Flexor pollicis longus
IP	interphalangeal (joint)
ISB	International Society of Biomechanics
MBS	Multi body simulation
MC1	First metacarpal bone
MCP	Metacarpophalangeal (joint)

MRI	Magnetic resonance imaging
OP	Opponens pollicis
PCM	Polygonal contact model
PCSA	Physiological cross sectional area
pIML	Palmar first intermetacarpal ligament
POL	Posterior oblique ligament
RoM	Range of motion
sAOL	Superficial anterior oblique ligament
SD	Standard deviation
TZ	Trapezium
UCL	Ulnar collateral ligament

A. Attachment Coordinates

In table A.1 and table A.2, the proximal and distal attachment coordinates of the ligaments and muscles are provided. Proximal and distal attachment points are defined in the trapezium and metacarpal coordinate system, respectively. For the definition of the coordinate systems see section 3.2.1.

	Proximal [mm]			**Distal [mm]**		
	x	y	z	x	y	z
dIML	-3.6295	17.6043	-5.5630	-3.0301	-6.5478	-12.8294
pIML	1.9086	12.6760	-4.7457	1.7564	-10.0164	-16.7585
UCL	3.9873	16.6614	-5.6538	11.8596	4.8287	1.6145
DRL	-3.4871	21.5372	6.6001	-1.7527	-0.7728	9.4222
sAOL$_1$	6.4893	22.5773	4.2930	6.3341	-1.7712	4.8158
sAOL$_2$	7.0055	22.5417	-4.5297	6.4318	-0.7112	-5.2709
dAOL	-5.5420	23.4800	2.8335	-6.1333	2.8250	4.5425
POL$_1$	-4.5469	24.0364	-5.2463	-5.1799	3.9675	-3.6734
POL$_2$	6.9945	23.0199	-4.2090	6.5470	-0.7711	-4.5631

Table A.1.: Ligament attachment coordinates

	Proximal [mm]			**Distal [mm]**		
	x	y	z	x	y	z
EPL	-7.1600	23.3200	-7.4000	-7.2000	2.0000	-7.0400
FPL	19.0400	23.3200	-1.2000	11.2800	4.0000	-1.2000
EPB	-9.2800	28.6800	1.1600	-11.3600	2.0000	3.2800
FPB	18.0400	23.3200	-7.3600	10.1600	4.0000	-7.9200
APL	2.8000	23.3200	5.9200	-5.3200	4.0000	7.2000
OP	5.4400	23.3200	7.6000	11.7200	4.0000	2.9600
APB	3.0400	23.3200	8.4800	3.0400	4.0000	12.3600
AD$_1$	18.7600	23.3200	-7.8000	18.7600	4.0000	-12.0000
AD$_2$	7.0000	-19.6000	-1.8400	18.7600	4.0000	-12.0000
AD$_3$	6.0000	-12.0000	-2.0000	25.4400	-12.0000	-28.0000
AD$_4$	6.0000	-12.0000	-2.0000	25.4400	-4.0000	-4.0000

Table A.2.: Muscle attachment coordinates

B. Muscle and Ligament Parameters

Table B.1 shows the initial lengths l_0 and the CSAs of the ligaments used in the model of the CMC joint. For the muscles, the initial strain ϵ_0, the PCSA, the architecture index i_a and the muscle optimum length l_0 are provided in table B.2. The calculation of the initial lengths and strains is explained in section 3.5.2.

	$l_0\,[\mathrm{mm}]$	CSA $[\,\mathrm{mm}^2\,]$
dIML	11.9750	3.45
pIML	15.5966	3.7
UCL	24.0000	3.37
DRL	11.7231	5.31
sAOL$_1$	8.6252	7.65
sAOL$_2$	9.0945	7.65
POL$_1$	11.9830	6.3
POL$_2$	12.0460	6.3
dAOL	8.6489	7.19

Table B.1.: Ligament parameters used in the simulation

	$\epsilon_0\,[-]$	PCSA $[\mathrm{mm}^2]$	$i_a\,[-]$	$l_0\,[\mathrm{mm}]$
EPL	0.0000	98	138	0.31
FPL	-0.1363	208	168	0.24
EPB	0.0000	47	105.6	0.54
FPB	-0.1363	66	57.2	0.73
APL	-0.1363	193	160.4	0.36
OP	-0.1363	102	55.5	0.64
APB	-0.1363	68	60.4	0.69
AD$_1$	-0.0561	97	54.6	0.63
AD$_2$	-0.0561	97	54.6	0.63
AD$_3$	-0.0561	97	54.6	0.63
AD$_4$	-0.0561	97	54.6	0.63

Table B.2.: Muscle parameters used in the simulation

C. Additional Simulation Outputs

The outputs presented in chapter 4 focus on the kinematics of the first metacarpal. As it was mentioned, a MBS delivers several additional output values, describing the state of each force element. In the following, the force element outputs resulting from a full flexion (see section 4.4) are presented and discussed briefly.

C.1. Contact Force Element Outputs

PCM provides several additional outputs, including the contact geometry, as well as the resulting force and torque with respect to the first metacarpal coordinate system. The contact area, as depicted in figure C.1, is the sum of the areas of the triangles of the surface in contact. It widens up from $69.29\,\mathrm{mm}^2$ in equilibrium position to $93.5\,\mathrm{mm}^2$ in full flexion.

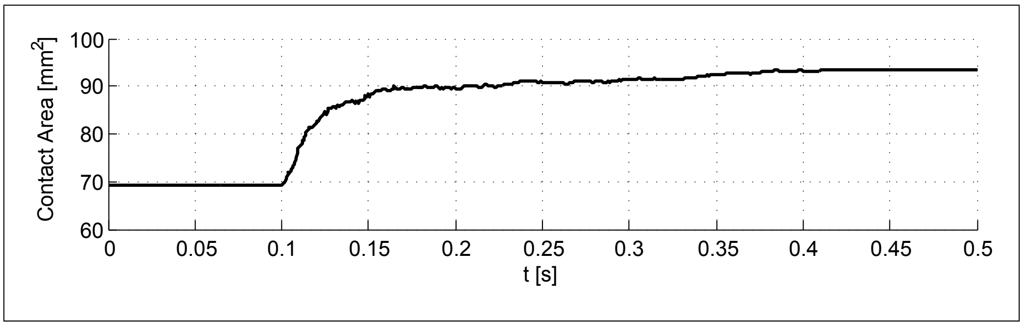

Figure C.1.: Contact area during flexion movement

The enlargement of the contact area is partly caused by the increased penetration of the surfaces, as shown in figure C.2. Both the maximum and the weighted penetration are plotted. The weighted penetration averages the penetrations calculated for each contact element with the respective triangle areas. The penetration is used for the calculation of the contact force using the elastic foundation model and does not represent the actual deformation of the surfaces. Since the material properties are similar, the deformation can be approximated by assuming the contact surface to be located in the middle of the penetrating surfaces, thus represented by half of the penetration depth.

Force and moments exerted on the first metacarpal are depicted in figure C.3. As anticipated, force is exerted mainly in the distal direction, pushing the first metacarpal away from the trapezium with a maximum force of $85.66\,\mathrm{N}$. During the movement, the contact force and moment increase due to the activation of the muscles and the restraining force of the ligaments. The moment resulting from the contact counteracts mainly flexion and adduction moments.

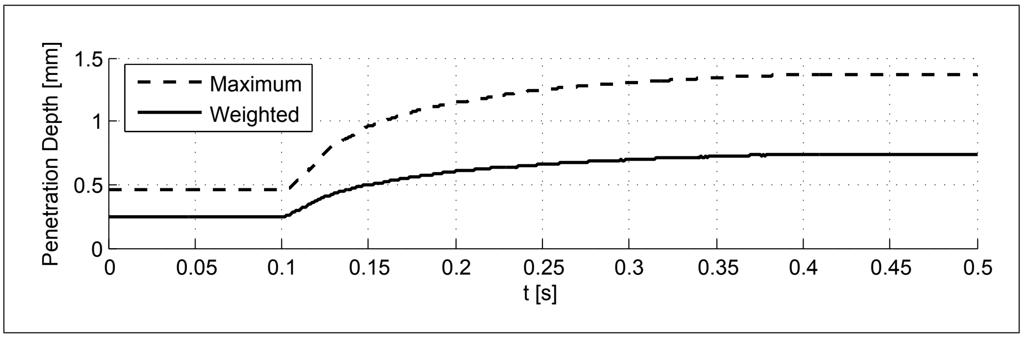

Figure C.2.: Weigthed and maximum penetration depth during flexion movement

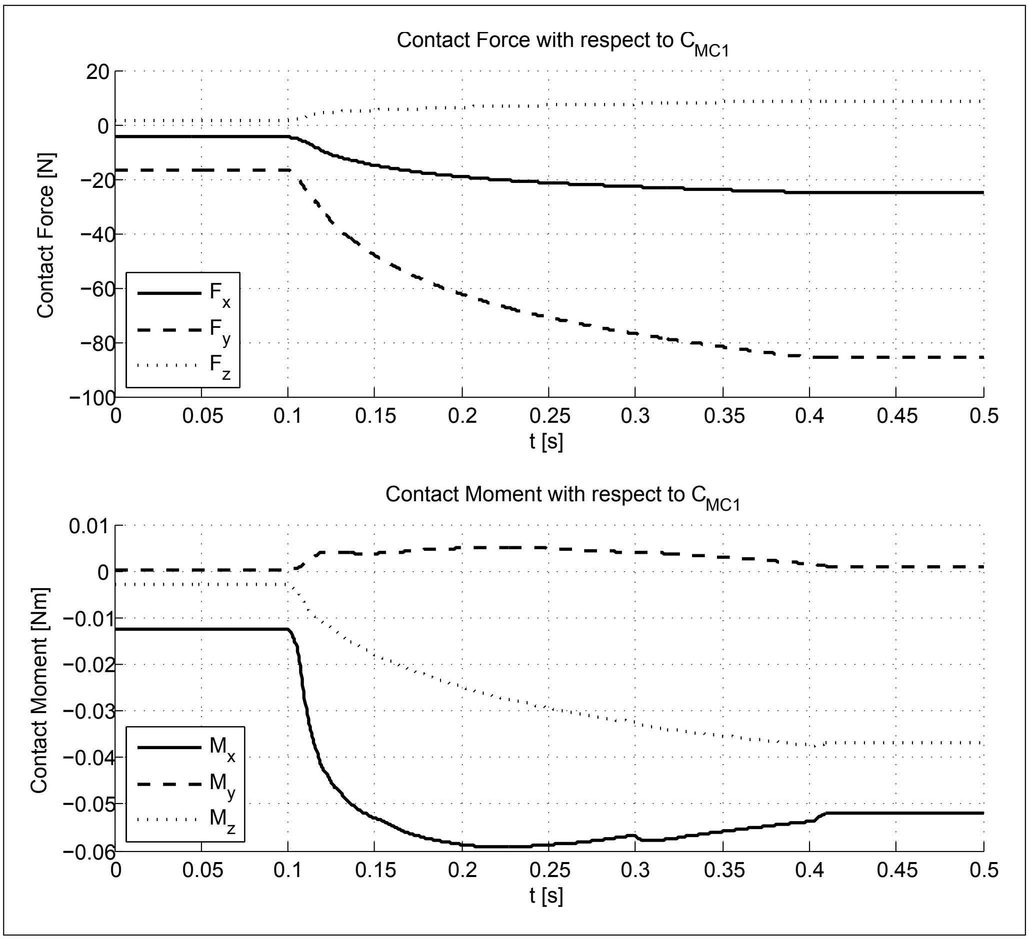

Figure C.3.: Contact force and moment exerted on the first metacarpal during flexion movement

C.2. Muscle Force Element Outputs

The muscles exert both active and passive forces, depending on the current strain in the muscle. Figure C.4 shows the forces of all muscle force elements. The AD is subdivided into two muscles with half of the PCSA of the AD. Each of these muscles is subdivided into two strings, exerting a force based on the averaged excursion. Hence, the forces resulting from AD_1 are equal to those of AD_2. The same holds for AD_3 and AD_4. The APL, EPL and EPB do not exert any active force since they are not activated. However, as they are stretched, a passive force restrains the flexion movement. Except for the FPL, all activated muscles develop a force of up to $12.78\,\mathrm{N}$ per force element. The comparably low active force of the FPL is caused by a large initial strain, which diminishes the maximum active force according to the Hill model.

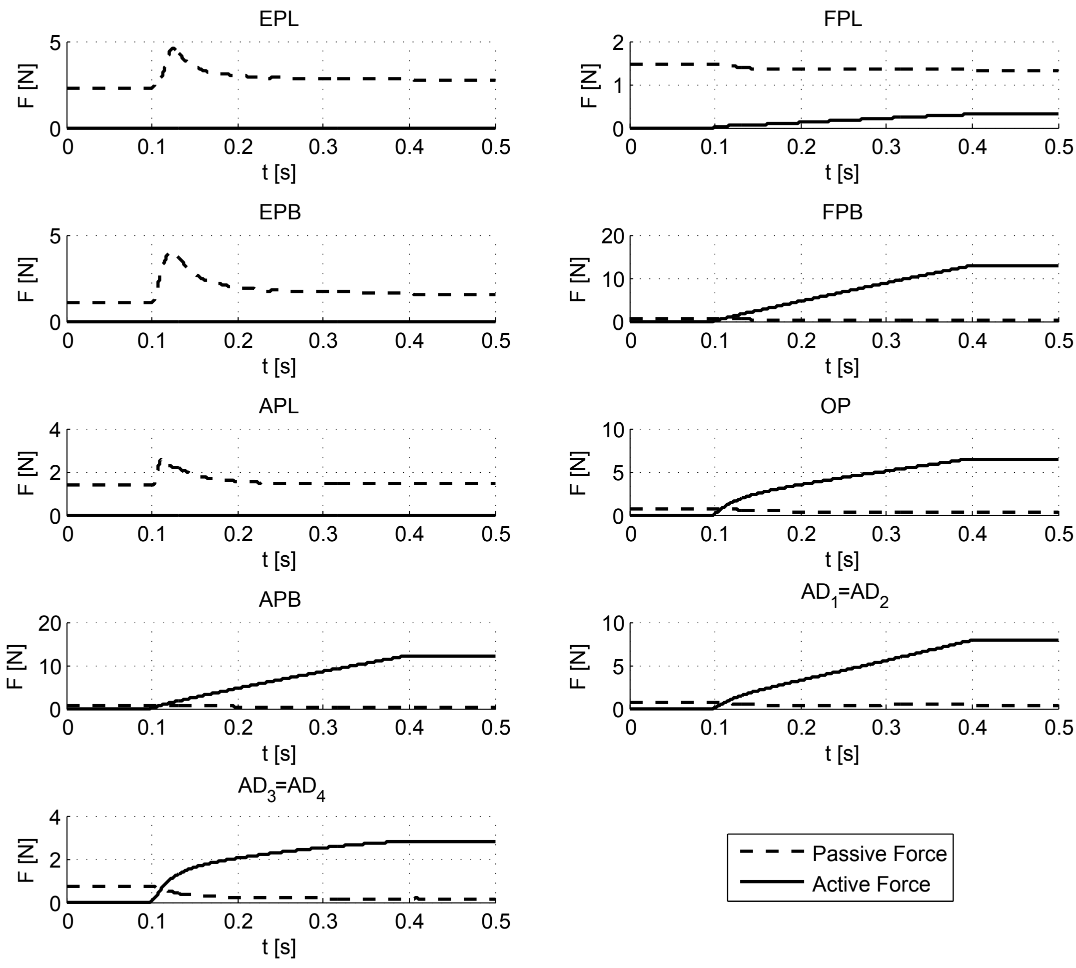

Figure C.4.: Active and passive muscles forces during flexion movement

C.3. Ligament Force Element Outputs

The ligaments restrain the movement of the joint by exerting tensile forces depending on their current strain. Hence, it is anticipated that especially dorsal ligaments are strained during flexion. In figure C.5, both ligament deflecion and forces are displayed. The only ligaments exerting forces are the dIML, POL$_1$ and POL$_2$, which are all located dorsally. The DRL is also a dorsal ligament but not strained during the movement. A possible reason is the abduction movement which accompanies the flexion and moves the proximal and distal point of attachment of the DRL closer together.

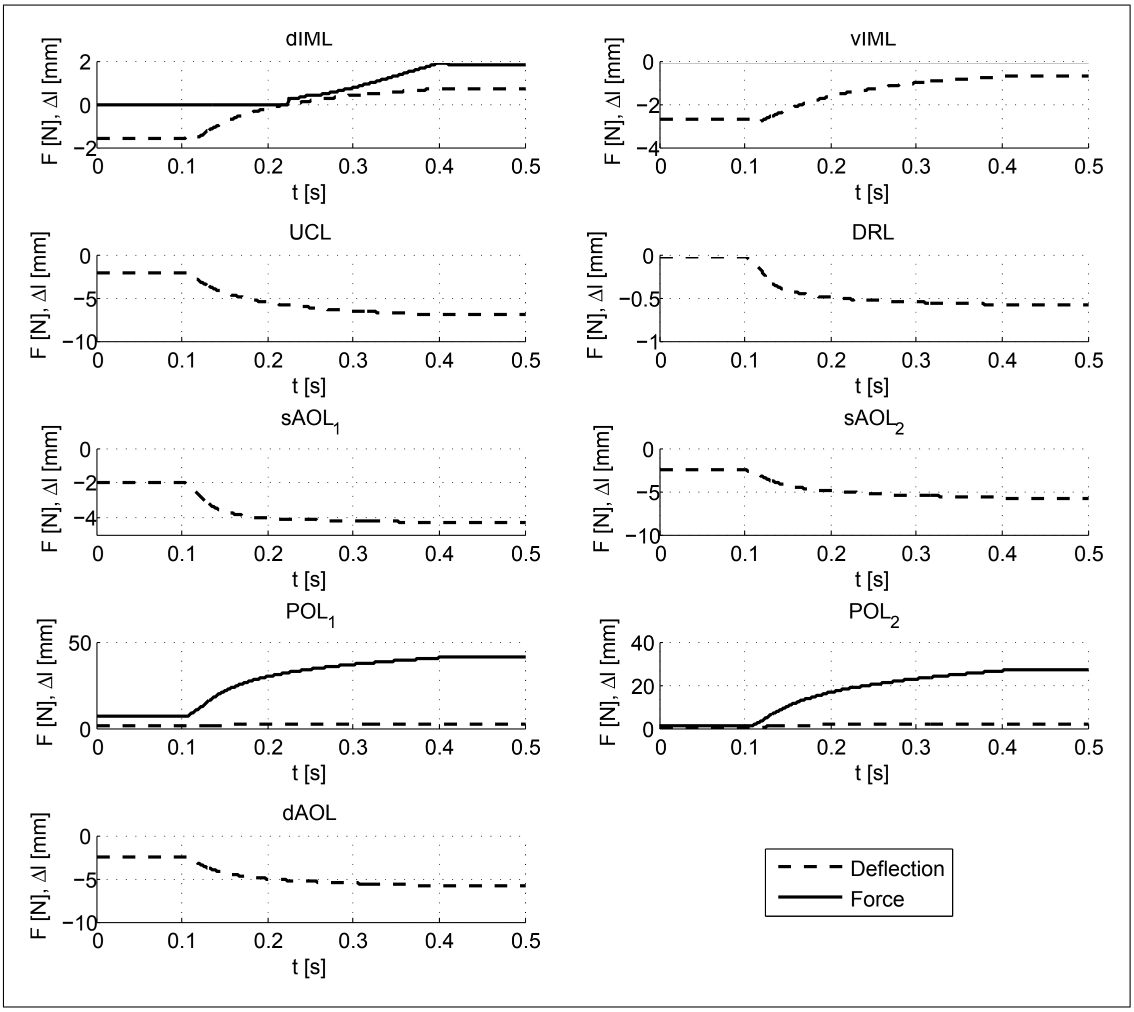

Figure C.5.: Ligament deflections and resulting forces during flexion movement